
# Measurement of three-dimensional deformation in objects subjected to vibration

Master of Optomecatronics

Student: Ing. José Eduardo Gutiérrez Prado

Adviser: Dr. Bernardino Barrientos García

December 2017
León, Guanajuato, México

# To

God for giving me life and allowing me to achieve my goals.

My father and mother for all their love, support and effort to give me a good life: José G. Gutiérrez Prado and Marta E. Prado Gonzalez.

My brother and sisters for accompanying me along my life: Lucia M. Gutiérrez Prado, José G. Gutiérrez Prado, Carolina E. Gutiérrez Prado and Ana U. Gutiérrez Prado.

My grandfather and grandmother for supporting me all the time: Hilario Gutiérrez and Lily Gutiérrez.

My girlfriend for all her love and support along my master's degree: Dejanira Olmedo.

My friends for all their support and friendship.

# Acknowledgements

I wish to thank CONACyT, for having granted me a master's scholarship.
My deepest gratitude to CIO and my teachers for letting me reach this goal. Also, my thanks to my colleague students for their friendship; especially to Fernanda González for all her help and real friendship.

Besides, my recognition to Dr. Bernardino Barrientos García for his guidance on this work. Additionally, my gratitude to M. C. Ricardo Valdivia Hernández and M. O. Carlos Mares Castro, who assisted me with some synchronization circuits and mechanical stages of the vibration systems.

My sincere acknowledgments to the reviewers of this work, for their useful comments and suggestions: Dr. María del Socorro Hernández Montes and Dr. Damiano Sarocchi.

# TABLE OF CONTENTS

# SUMMARY

At present, the use of complex machines in the industry is quite common, where machines have to be productive and reliable. The design of each element of a machine is important, and we have to consider the presence of any strains, shears, moments and any other interaction force. All of these variables can be assessed by the measurement of displacement.

Several methods enable us to measure generally one Cartesian component of displacement. In this work, we propose a method to measure the three-dimensional deformation (out-plane and in-plane components of displacement) of an element subjected to a periodic force, using a combination of fringe projection and digital image correlation; this method is able to obtain simultaneously the out-plane and in-plane components of displacement by means of only one recording. For this purpose, we use color encoding. Fringe projection and digital image correlation methods are optical methods that are non-contact and full-field.

As application examples of the method, we analyze circular plates and membranes, which are made of different materials, when subjected to vibration. A high-speed camera is used for this purpose.

# 1.INTRODUCTION

Measurement of displacement (or deformation) is an important aspect of mechanical design and testing. For this purpose, there are several methods. Standard methods, such as calipers and gauges, are reliable, but they need to be in contact with the object under test. Besides, they generally allow us the measurement of displacement at only one spatial position.

With the introduction of optical methods, the latter disadvantages are overcome. In this category of methods, there are several types of them; we can mention broadly interferometric [1-3] and white-light methods [4-13].

Interferometric methods are based on the interference of multiple beams of coherent light; for example, in holography (or in speckle pattern interferometry, ESPI), two beams are combined at the sensor of a digital camera. The sensitivity in this case is extremely high, of the order on nm; however, such an extreme sensitivity gives rise to the problem of sensitivity to environment disturbances. Additional to this problem, is the inconvenience of using several sources of light or several cameras. The range of displacement sometimes becomes a problem as well, particularly in industrial applications, where displacement values of the order of several mm are not uncommon. All of these limitations are handled by white-light optical methods, such as moiré methods and correlation methods. In moiré methods, one technique that has been developed in the last 30 years is fringe projection, FP [4-12]. In this technique, the interference pattern arising in interferometric methods corresponds to a user-defined pattern; this pattern is usually generated on a computer and sent to a digital projector for projection purposes. In this case, the period of the pattern can be readily selected by the user, and therefore the sensitivity of the method can be appropriately adjusted. Since no interference of beams is necessary, FP is one of the most robust techniques. The simplicity of the setup makes it to be preferred as well: the setup consists of the above-mentioned projector and a digital camera. An angle between the observation direction (optical axis of the camera lens) and the projection direction is allowed in order to have sensitivity to displacement along the optical axis of the imaging lens (camera lens); this component of displacement is the out-of-plane component.

A similar technique to FP is digital image correlation, DIC [13-17]. The same setup is used, but in this case the signal is not a fringe pattern as in FP, but it corresponds to the image of the texture of the object under test. Therefore, any displacement contained in a plane perpendicular to the optical axis can be measured; this component of displacement can be thought of two component of displacements mutually perpendicular, which are known as in-plane components of displacement.

As recently shown in [18-23], the three-components of displacement (three-dimensional displacement) can be measured simultaneously by a combination of FP and DIC (FP-DIC technique). In this case, the signal for each technique is encoded on the RGB signal fed to the digital projector. Then, by using a color camera, when images are registered, the information from each color channel can be readily separated by software and then it can be used for analysis.

The FP-DIC method is applied to the measurement of vibration of membranes and plates. The materials of the objects under analysis vary from completely flexible, such as latex and rubber, and those with rigidity, e.g. aluminum.

To have a wider insight of the deformation nature, two types of loading is tested: uniformly distributed and point-wise. For the first type, a speaker is used, and for the second one, a shaker.

The results are accompanied by analytical comparisons, as well as numerical simulations by ANSYS.

This work is organized as follows. The rest of it is organized in 4 chapters. In Chapter 2, the theory of FP and DIC is given. Additionally, the fundamental basis of vibration of thin plates and membranes is included. Then, in Chapter 3, results from analytical and simulation approaches is presented. Experimental results are incorporated in Chapter 4. Here, a wide range of application examples is discussed. Finally, in Chapter 5, the general conclusions and future work are drawn out.

## 1.1 REFERENCES


1. R. Jones and C. Wykes, *Holographic and speckle interferometry*, 2nd Ed., Cambridge University Press, Cambridge (2009).
2. D. W. Robinson, *Interferogram analysis (digital fringe pattern measurements),* IOP Publishing Ltd., Philadelphia (1993).
3. K. J. Gasvik, *Optical Metrology*, 3rd Ed., John Wiley and Sons, Sussex, UK (2003).
4. R. Weller and B. M. Shepperd, "Displacement measurement by mechanical interferometry," Proc. Soc. Exp. Stress. Anal. (SESA), **6**(1), 35-38 (1948).
5. S. H. Rowe and W. T. Welford, "Surface topography of non-optical surfaces by projected interference fringes," Nature, **216**, 786-787 (1967).
6. D. M. Meadows, W. O. Johnson, and J. B. Allen, "Generation of surface contours by moiré patterns," App. Opt., **9**(4), 942-947 (1970).
7. B. Dessus, M. Leblanc, "The 'fringe method' and its application to the measurement of deformations, vibrations, contour lines and differences of objects," Optoelectronics 5, 369-391 (1973).
8. G. Indebetouw, "Profile measurement using projection of running fringes," App. Opt., **17**(18), 2930-2933 (1978).
9. M. Takeda, H. Ina, and S. Kobayashi, "Fourier-transform method of fringe –pattern analysis for computer-based topography and interferometry," JOSA, **72**(1), 156-160 (1982).
10. V. Srinivasan, H. C. Liu, and M. Halioua, "Automated phase-measuring profilometry of 3-D diffuse objects," App. Opt., **23**(18), 3105-3108 (1984).
11. A. K. Asundi, "Moiré methods using computer-generated gratings," **32**(1), Opt. Eng., 107-116 (1993).
12. B. Barrientos, M. Cywiak, W. K. Lee, and P. Bryanston-Cross, "Measurement of dynamic deformation using a superimposed grating," Rev. Mex. Fis. **50**(1), 12-18 (2004).
13. N. A. Fomin, *Speckle photography for fluid mechanics measurements*, Springer, Berlin (1998).
14. M. Raffel, C. Willert, and J. Kompenhans, *Particle image velocimetry*, Springer, Berlin (1998).
15. W. H. Peters and W. F. Ranson, "Digital imaging techniques in experimental stress analysis," Opt. Eng., **21**, 427-431 (1981).
16. M. A. Sutton, W. J. Wolters, W. H. Peters, W. F. Ranson, and S. R. McNeill, "Determination of displacements using an improved digital correlation method," Ima. and Vision Comp., **1**(3), 133-139 (1983).
17. B. Pan, K. Quian, H. Xie, and A, Asundi, "Two-dimensional digital image correlation for in-plane displacement and strain measurement: a review," Meas. Sci. Technol., **20**, 062001 (2009).
18. B. Barrientos, M. Cerca, J. García-Márquez, and C. Hernandez-Bernal, "Three-dimensional displacement fields measured in a deforming granular-media surface bycombined fringe projection and speckle photography," J. Opt. A: Pure Appl. Opt., **10**, 104027 (2008).
19. H. Weber, R. Lichtenberger, and T. Wolf, "The combination of speckle correlation and fringe projection for the measurement of dynamic 3-D deformations of airbags caps," in *Proceedings of IUTAM Symposyum on Advanced Optical Methods and Applications in Solid Mechanics*, A. Lagarde, ed. (Kluwer Akademic Publishers, 2000), pp. 619–626.
20. C. J. Tay, C. Quan, T. Wu, and Y. H. Huang, "Integrated method for 3-D rigid-body displacement measurement using fringe projection," Opt. Eng., **43**(5), 1152-1159 (2004).
21. P. Siegmann, V. Alvarez-Fernandez, F. Diaz Garrido, and A. E. Patterson, "A simultaneous in- and out-of-plane displacement measurement method," Opt. Lett. **36**(1), 10–12 (2011).
22. C. Mares, B. Barrientos, and A. Blanco, "Measurement of transient deformation by color encoding," Opt. Express **19**, 25712–25722 (2011).
23. C. Mares, B. Barrientos, and R. Valdivia, "Three-dimensional displacement in multi-colored objects," Opt. Express, **25**(10), 11652–11672 (2017).

# 2. THEORY

## 2.1 FRINGE PROJECTION, FP

Fringe projection is an optical method to obtain the profile of an object's surface. We project a grating, generated by software, onto a plane surface, known as the reference surface; if the projection comes from infinity, we can assume that the projected grating is not distorted (its period is constant throughout the whole surface). The intensity of the reference image is then represented by [1]

$$I_R(x) = a + b\cos\left(\frac{2\pi x}{p}\right), \tag{2.1}$$

where $a$ is the background illumination level, $b$ is the modulation of the signal amplitude, $x$ is the Cartesian coordinate and $p$ is the grating period.

The grating is reflected by the surface and impinges on the camera sensor. The captured image is different from the projected one; to visualize this, in Fig. 2.1 we illustrate cross sections of these two images; note that the profile in (b) is not a perfect sinusoidal function as the one in part (a). This arises from the transfer function of the imaging system (combination of camera and lens).

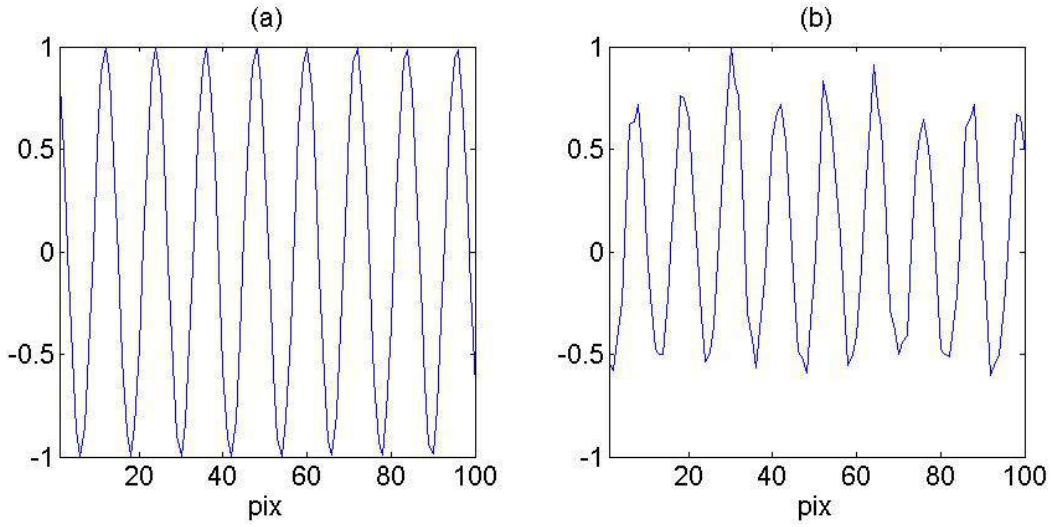


*Fig 2.1. Cross-section of projected-fringe image; (a) computer-generated image; (b) captured image.*

When an object replaces the reference plane, the optical paths of the projected image are modified, as shown in Fig. 2.2. The camera is focused on the reference plane, so the camera sensor captures the image of the grating projected onto the object as if it came from the reference plane; note that the grating period is shifted proportionally to the object's topography.

The deformed grating shows a lateral modulation due to the object height, represented by $\Delta x$. The image of the displaced grating can be represented as

$$I_d(x) = a + b\cos\left[\frac{2\pi(x+\Delta x)}{p}\right], \tag{2.2}$$

This equation can be rewritten as

$$I_d(x) = a + b\cos\left(\frac{2\pi x}{p} + \frac{2\pi\Delta x}{p}\right). \tag{2.3}$$

where the second term of the argument of the cosine is a phase difference between Eq. 2.1 and Eq. 2.2, that is

$$I_d(x) = a + b\cos\left(\frac{2\pi x}{p} + \Delta\phi\right), \tag{2.4}$$

where

$$\Delta\phi = \frac{2\pi\Delta x}{p}. \tag{2.5}$$

The phase difference has the information of the object topography. There are several methods to obtain $\Delta\phi$; in Secs. 2.1.1 and 2.1.2 two methods are described, phase stepping and Fourier transform.

Once the phase difference is obtained, the object height distribution can be computed. The transverse displacement is related to the height distribution by (see Fig. 2.2)

$$\frac{\Delta x}{B} = \frac{h}{H - h}; \tag{2.6}$$

where $h$ is the local object height, $B$ is the base distance and $H$ is the distance between the reference plane and the sensor plane.

Combining Eqs. 2.5 and 2.6, we obtain

$$h = \frac{H}{1 + \frac{2\pi B}{p\Delta\phi}}; \tag{2.7}$$

which recovers the topography of the object from the phase difference. To simplify Eq. 2.7, $h = \frac{H}{\frac{2\pi B}{p\Delta\phi}}$ consider that $B$ is much greater than $p$, then ; and considering that $\tan\theta = \frac{B}{H}$, Eq. 2.7 yields

$$h = \frac{p\Delta\phi}{2\pi\tan\theta}. \tag{2.8}$$

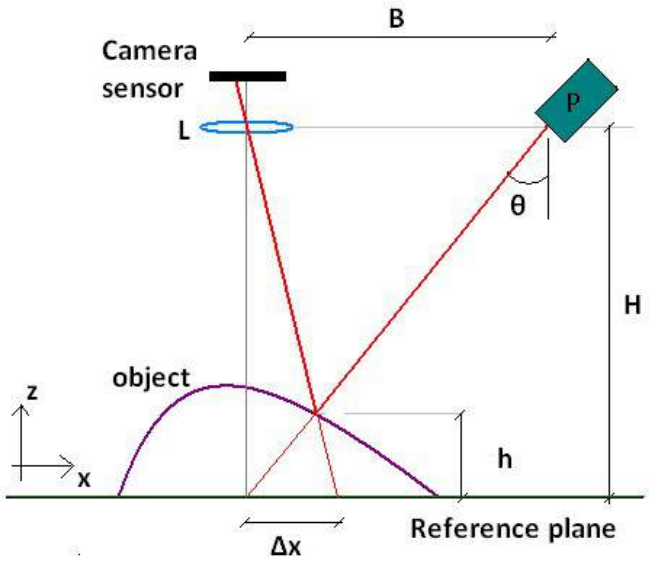


*Fig. 2.2 Basic arrangement of fringe projection. Here P and L correspond to digital projector and imaging lens, respectively.*

### 2.1.1 Phase stepping

From Eq. 2.1, to calculate $\phi$ for any position, we can use the phase stepping method, which consists of introducing a known phase term into the argument of the cosine [1],

$$I = a + b\cos\left(\phi + \alpha\right), \tag{2.9}$$

and is introduced experimentally for automatization purposes.

In Eq. (2.9), since intensity, $I$, can be measured, we have three unknowns ($a, b$ and $\phi$) requiring a minimum of three different equations to determine the phase. Therefore, the following system can be formed,

$$I_1 = a + b\cos\left(\phi + \alpha_1\right), \tag{2.10}$$

$$I_2 = a + b\cos\left(\phi + \alpha_2\right), \tag{2.11}$$

$$I_3 = a + b\cos\left(\phi + \alpha_3\right), \tag{2.12}$$

where $\alpha_1$, $\alpha_2$ and $\alpha_3$ are the prescribed phase steps.

To determine the phase, calculate

$$I_1 - I_2 = b\left[\cos\left(\phi + \alpha_1\right) - \cos\left(\phi + \alpha_2\right)\right], \tag{2.13}$$

$$I_3 - I_2 = b\left[\cos\left(\phi + \alpha_3\right) - \cos\left(\phi + \alpha_2\right)\right]. \tag{2.14}$$

Dividing Eq. 2.13 by Eq. 2.14, we have

$$\frac{I_1 - I_2}{I_3 - I_2} = \frac{\cos\left(\phi + \alpha_1\right) - \cos\left(\phi + \alpha_2\right)}{\cos\left(\phi + \alpha_3\right) - \cos\left(\phi + \alpha_2\right)}. \tag{2.15}$$

From the trigonometric identity, $\cos(\alpha + \beta) = \cos\alpha\cos - \sin\alpha\sin\beta$, Eq. 2.15 can be expressed as

$$\frac{I_1 - I_2}{I_3 - I_2} = \frac{\cos\phi\cos\alpha_1 - \sin\phi\cos\alpha_1 - \cos\phi\cos\alpha_2 + \sin\phi\sin\alpha_2}{\cos\phi\cos\alpha_3 - \sin\phi\cos\alpha_3 - \cos\phi\cos\alpha_2 + \sin\phi\sin\alpha_2}, \tag{2.16}$$

regrouping terms

$$\frac{I_1 - I_2}{I_3 - I_2} = \frac{\cos\phi(\cos\alpha_1 - \cos\alpha_2) - \sin\phi(\cos\alpha_2 - \sin\alpha_1)}{\cos\phi(\cos\alpha_3 - \cos\alpha_2) - \sin\phi(\cos\alpha_2 - \sin\alpha_3)}. \quad (2.17)$$

After mathematical manipulation, this expression gives

$$\tan\phi = \frac{(I_3 - I_2)\cos\alpha_1 - (I_3 - I_2)\cos\alpha_2 - (I_1 - I_2)\cos\alpha_3 + (I_1 - I_2)\cos\alpha_2}{(I_1 - I_2)\sin\alpha_2 - (I_1 - I_2)\sin\alpha_3 - (I_3 - I_2)\sin\alpha_2 + (I_3 - I_2)\sin\alpha_1}. \quad (2.18)$$

In particular, by using $\alpha_1 = \frac{\pi}{4}$, $\alpha_2 = \frac{3\pi}{4}$, $\alpha_3 = \frac{3\pi}{4}$, Eq.2.18 results

$$\phi = \tan^{-1}\frac{I_3 - I_1}{I_1 - I_2}. \quad (2.19)$$

As observed, this algorithm is immune to the background level and to the modulation amplitude, because the background is eliminated by the subtraction in Eq. 2.19 and the modulation amplitude is eliminated by the division in Eq. 2.19. A disadvantage is that the object has to remain unchanged during the time the images are captured.

### 2.1.2 Fourier transform method

An alternative to phase stepping is the Fourier method, which has the advantage of calculating $\phi$ by using only one image [1]. In this case, a carrier frequency, $f_o = \frac{1}{p}$, should be introduced, instead of the phase steps. Hence, Eqs. 2.1 and 2.4 are written as

$$I_r(x) = a + b\cos(2\pi f_0 x), \quad (2.20)$$

$$I_d(x) = a + b\cos(2\pi f_0 x + \Delta\phi). \quad (2.21)$$

Taking one of them, for example expression in Eq. 2.21, it can be written in complex form as

$$I_d(x) = a + \frac{b}{2}e^{i\Delta\phi}e^{i2\pi f_0 x} + \frac{b^*}{2}e^{-i\Delta\phi}e^{-i2\pi f_0 x}; \quad (2.22)$$

applying the Fourier transform, it gives

$$\pounds\{I_d(x)\} = \int_{-\infty}^{\infty} ae^{-i2\pi fx}dx + \int_{-\infty}^{\infty}\frac{b}{2}e^{i\Delta\phi}e^{i2\pi xf_0}e^{-i2\pi xf}dx + \int_{-\infty}^{\infty}\frac{b^*}{2}e^{-i\Delta\phi}e^{-i2\pi xf_0}e^{-i2\pi xf}dx, \quad (2.23)$$

where $\pounds$ denotes the operator of Fourier transform, and $e^{-i2\pi fx}$ is the kernel of the Fourier transform, with $f$ being the spatial frequency coordinate. Therefore,

$$\pounds\{I_d(x)\} = \int_{-\infty}^{\infty} ae^{-i2\pi fx}dx + \int_{-\infty}^{\infty}\frac{b}{2}e^{i\Delta\phi}e^{-i2\pi x(f-f_0)}dx + + \int_{-\infty}^{\infty}\frac{b^*}{2}e^{-i\Delta\phi}e^{-i2\pi x(f+f_0)}dx; \quad (2.24)$$

consider that

$$\int_{-\infty}^{\infty} e^{-i2\pi fx}dx = \delta(f), \quad (2.25)$$

then Eq. 2.24 results as

$$\pounds\{I_d(x)\} = a\delta(f) + C(f - f_0) + C^*(f + f_0), \quad (2.26)$$

where $C(f)$ is $\pounds\left\{\frac{b}{2}e^{i\Delta\phi}\right\}$. The graphical representation of Eq. 2.26 is illustrated in Fig. 2.3. The peak centered on the origin represents the contribution of the average intensity of the whole image, a constant value; the two side lobes centered on $f_0$ and $-f_0$ correspond to the frequency content of the object height. Thus, arbitrarily filtering one of them, we have

$$\pounds\left\{I_{d,filter}(x)\right\} = C(f - f_0). \tag{2.27}$$

By applying the inverse Fourier transform, it gives

$$\pounds^{-1}\left\{\pounds\left\{I_{d,filter}(x)\right\}\right\} = \frac{b}{2}e^{i(2\pi x f_0 + \Delta\phi)}; \tag{2.28}$$

it follows that

$$I_{d,filter}(x) = \frac{b}{2}e^{i(2\pi x f_0 + \Delta\phi)}. \tag{2.29}$$

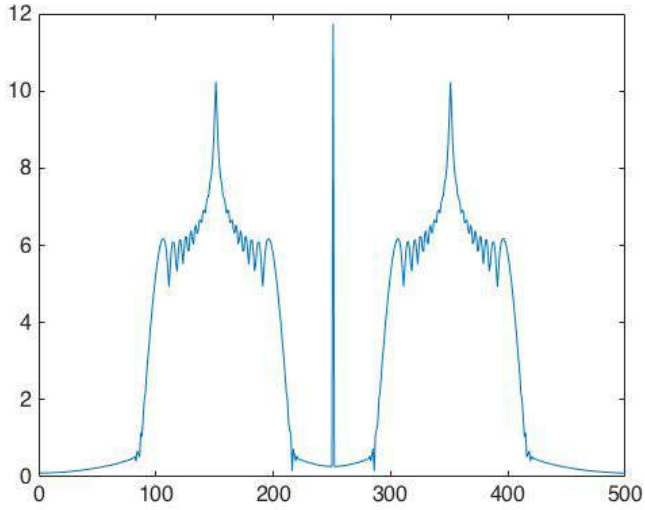


*Fig. 2.3 An example of Eq. (2.29).*

To obtain the argument, $\theta_d = 2\pi x f_0 + \Delta\phi$, we can write

$$\tan\theta_d = \frac{Im\left\{I_{d,FT}\right\}}{\mathrm{Re}\left\{I_{d,FT}\right\}} = \frac{\sin(2\pi x f_0 + \Delta\phi)}{\cos(2\pi x f_0 + \Delta\phi)}, \tag{2.30}$$

so

$$\theta_d = \tan^{-1}\left[\frac{Im\left\{I_{d,FT}\right\}}{\mathrm{Re}\left\{I_{d,FT}\right\}}\right]; \tag{2.31}$$

remember that $\theta_d$ corresponds to the deformed image, so

$$\theta_d = 2\pi x f_0 + \Delta\phi. \tag{2.32}$$

Doing the same procedure for Eq. 2.20, we have

$$\theta_r = 2\pi x f_0, \tag{2.33}$$

and subtracting Eq. 2.32 from Eq. 2.33

$$\theta_d - \theta_r = \Delta\phi. \tag{2.34}$$

### 2.1.3 Phase unwrapping

In sections 2.1 and 2.2, we found a solution to obtain the phase from a fringe image [1],

$$\theta = \tan^{-1}\left(\frac{A}{B}\right), \tag{2.35}$$

where $A$ and $B$ are intensity recorded functions.

The $\tan^{-1}$ function is multivalued, so the solution for $\theta$ results in a saw tooth function with discontinuities every $2\pi$, as shown in Fig. 2.4(a).

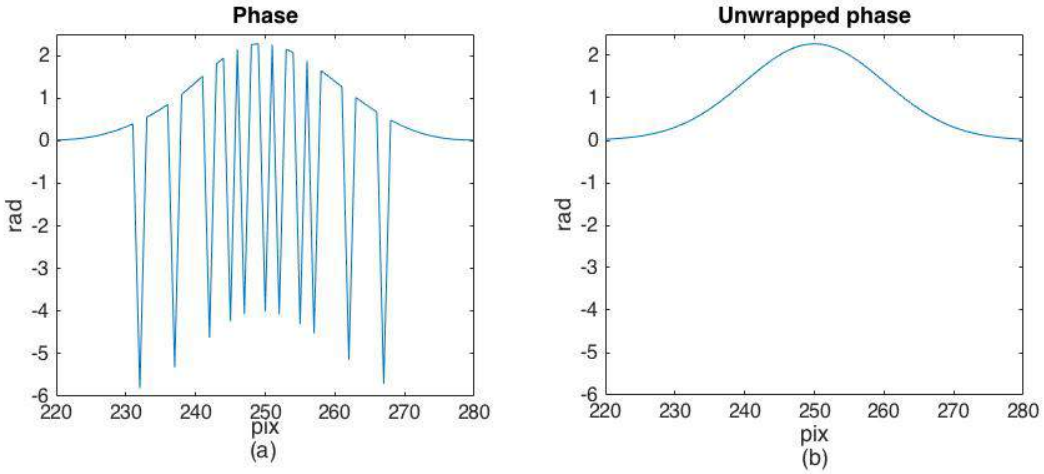


*Figure 2.4 (a) Wrapped phase map and (b) corresponding unwrapping phase map.*

The unwrapping algorithm makes use of the following. If $\phi$ increases, the slope of the function is positive; if $\phi$ decreases, the slope is negative. Then, to remove the discontinuities, the phase along a line adds or subtracts $2\pi$-multiples according to the sign of the difference between two neighbor pixels.

For the fringe projection, a simple method is sufficient to unwrap the phase, as a sequential scan through the data (line by line). At each pixel the gradient phase is calculated by differentiation

$$\Delta\phi = \phi_n - \phi_{n-1}, \tag{2.36}$$

where $n$ is the actual pixel position. If $|\Delta\phi|$ exceeds $\pi$, then a $2\pi$ discontinuity is assumed and this is corrected by the addition and subtracting of $2\pi$ according to the sign of $\Delta\phi$.

The effectiveness of unwrapping phase algorithms is related the ability to accurately detect the $2\pi$ phase jumps; this is difficult if the images contain noise [see Fig. 2.4(b)].

## 2.2 DIGITAL IMAGE CORRELATION, DIC

Literally, correlation means level of similarity, i.e., it refers to the degree to which the values of one function relate to the values of another function [2]. The correlation indicates the strength and the direction of the similarity between functions [3].

Starting with the simplest example, consider a one-dimensional function. If this function is spatially displaced in x-direction, we can assume that a new function is the original function displaced by $\Delta x$.

The correlation integral of two functions $f$ and $g$ is expressed as [2]

$$c(\Delta x) = \int_{-\infty}^{\infty} f(x)g(x - \Delta x)dx \,. \tag{2.37}$$

By calculating the correlation integral for many values of $\Delta x$ we will obtain a maximum when $\Delta x$ corresponds to the original function displacement.

Figure 2.5 shows an example of correlation; in this figure the functions $f$ and $g$ represent the same function. Setting $f$, then $g$ is shifted from left to right; in Fig. 2.5 (a), $g$ is on the left side of $f$ without overlap and the result of correlation is zero. As $g$ is shifted to the right, Fig. 2.5(b), the result of the correlation increases linearly. When $g$ is completely overlapped with $f$, the product of the integral is a maximum. If $g$ is further shifted to the right, the result of the integral decreases, Fig. 2.5(c), until the result of the integral becomes zero [Fig 2.5(d)].

The result of the correlation along the x-direction is a triangle function, Fig. 2.6(e), where the maximum value corresponds to the shift with the greatest similarity between functions. If $g$ is a copy of $f$, but with a spatial shift, we can assume that the position of the maximum value corresponds to the displacement between functions.

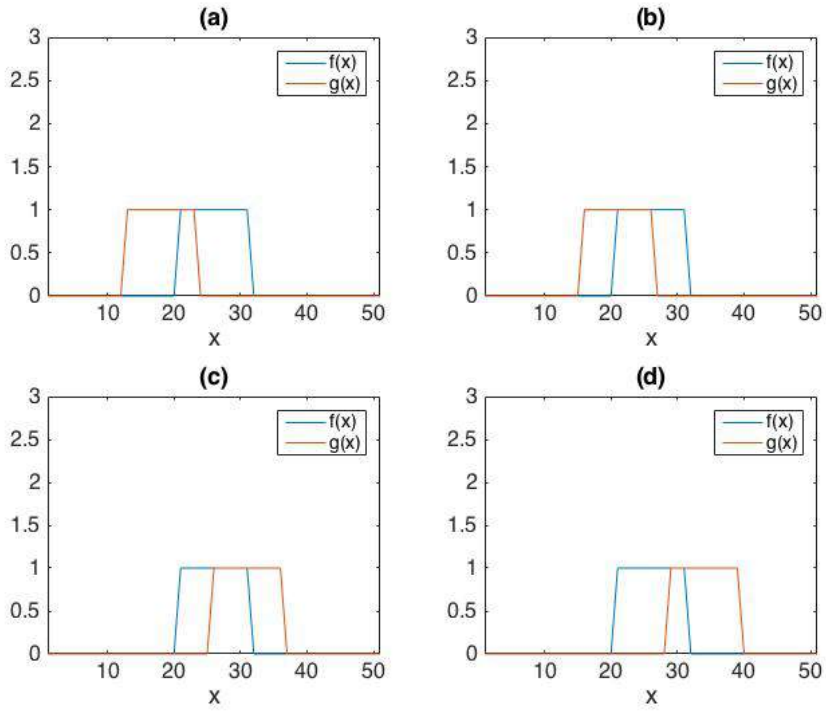

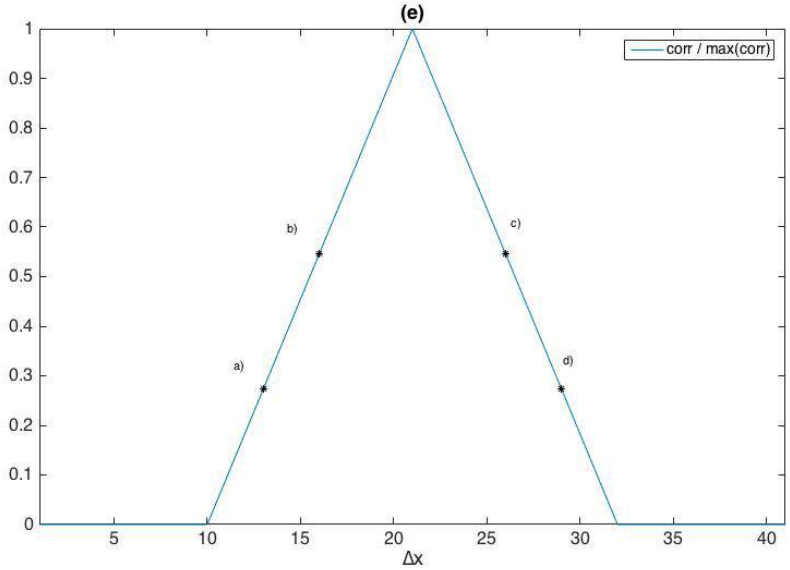


(e)

*Figure 2.5 Correlation of two functions. (a), (b), (c) and (d) are part of the process to shift spatially one function with respect to another. (e) Result of the correlation.*

### 2.2.1 Two-dimensional correlation

Analogous to the linear correlation, Eq. 2.38, the two-dimensional correlation is given as [2]

$$c(\Delta x, \Delta y) = \int_{-\infty}^{\infty} \int_{-\infty}^{\infty} f(x,y) g(x - \Delta x, y - \Delta y) dx dy \,, \tag{2.38}$$

and its discrete form, useful to analyze images, is given by

$$c(\Delta x, \Delta y) = \sum_{\Delta p=1}^{M} \sum_{\Delta q=1}^{N} f(x,y) g(x - \Delta p, y - \Delta q) \,, \tag{2.39}$$

where $M$ and $N$ are the image dimensions, in pixels (pix).

To calculate the correlation between two images using Eq. 2.39, each image has to be centered into a three times larger image, filled with zeroes all around and the result is cut to the size of the original image. The resultant image is called correlation map.

As an example, in Fig. 2.6, we have a reference image with a random speckle field generated by Matlab; the deformed image is the reference image shifted in x-direction and in y-direction (10 and -2 pix, respectively). Applying Eq. 2.39 to Figs. 2.6(a) and (b), we obtain Fig. 2.6(c); the maximum values of the correlation function correspond to the prescribed values [Fig. 2.6(d)].

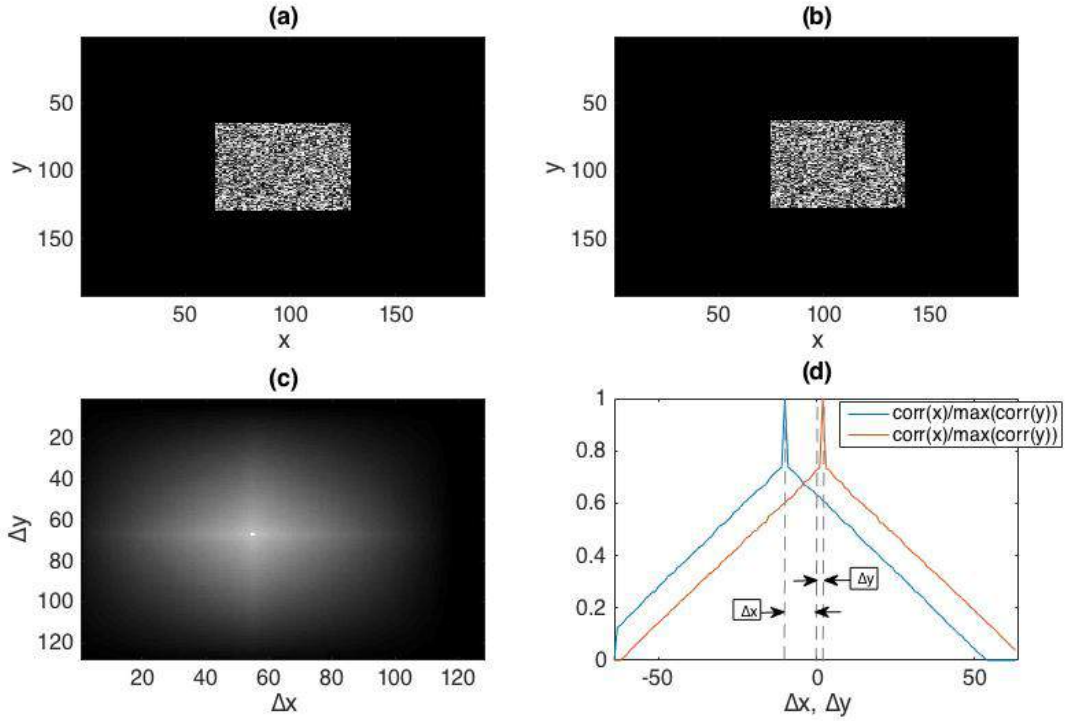


*Figure 2.6 Correlation between two images, each image (64x64 pix) is centered in a three-time larger image than the original. (a) Reference image, (b) deformed image (reference image shifted), (c) correlation map, and (d) cross-section of the correlation map located on the coordinate of the position of the correlation maximum.*

When using correlation to study mechanical deformation, we project an image of randomly located spots over an object, and then a force is applied to the object. If we take an image of the object before and after deformation, then we divide each recorded image in subimages and calculate the correlation using each pair of subimages (reference and deformed), to obtain a correlation map; Fig. 2.7 is the result obtained for the latter example.

In the correlation map, the arrows represent the direction and magnitude of the deformation at a certain point.

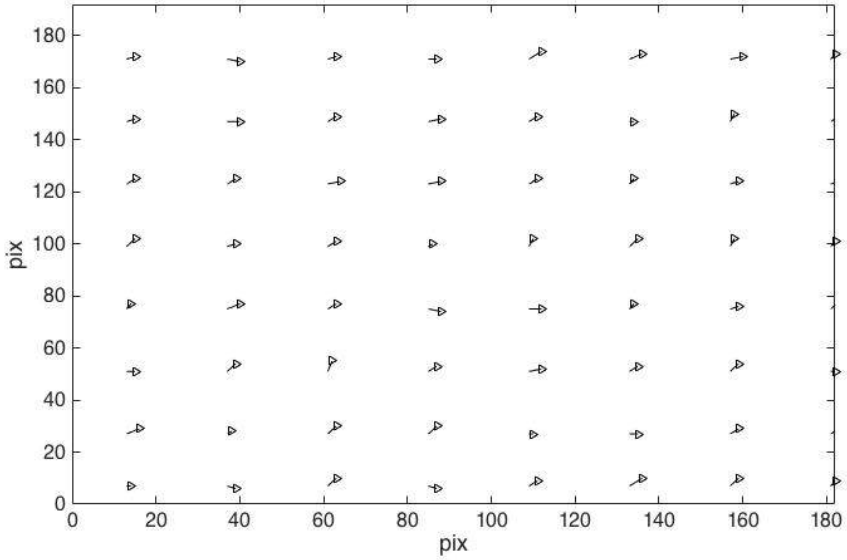


*Figure 2.7 Displacement map, using subimages of 24x24 pix.*

To calculate the two-dimensional discrete correlation, it is necessary to apply Eq. 2.39 to each subimage, which as a whole represents a heavy computing time.

### 2.2.2 Correlation by Fourier transform

A faster algorithm than the discrete correlation, to obtain correlation, is the use of the Fourier transform. By taking the Fourier transform of the correlation of two functions, Eq. 2.40 [2]

$$\Im\{c(\Delta x,\Delta y)\}=\int_{-\infty}^{\infty}\int_{-\infty}^{\infty}\int_{-\infty}^{\infty}\int_{-\infty}^{\infty}f(x,y)g(x-\Delta x,y-\Delta y)dxdy\exp\left[-i2\pi(u\Delta x+v\Delta y)\right]\Delta x\Delta y\,,$$

where $u$ and $v$ are the frequency coordinates. This may be written as [2, 4]

$$\Im\{c(\Delta x,\Delta y)\}=F(u,v)G^{*}(u,v). \tag{2.41}$$

This represents the Fourier transform of function $f$ multiplied by the complex conjugate of Fourier transform of function $g$.

By applying the inverse Fourier transform to Eq. 2.41, the result is

$$c(\Delta x,\Delta y)=\Im^{-1}\left\{F(u,v)G^{*}(u,v)\right\}. \tag{2.42}$$

Equation 2.42 gives us a faster way to calculate the correlation of two functions, since the Fourier transform can be calculated by using the fast Fourier transform.

## 2.3 THEORY OF VIBRATION OF CIRCULAR PLATES

In this section, we describe to two types of vibrations, one when the object has a behavior as a membrane and the other when the object corresponds to a thin plate.

For a membrane, when the object is vibrating only tension is considered, because the membrane does not support bending. On the other hand, for thin plates, we assume the presence of bending, shear forces and strains (extensional and shearing). In Section 2.3.1, we describe the vibration modes of a membrane; Section 2.3.2 describes the vibration modes in a thin plate, and in Section 2.3.3 we compare the values of the resonance frequencies for each case.

### 2.3.1 Vibration modes of a membrane

Let us start with one of the simplest examples of vibration, a string vibrating in the xy-plane. The string is along the x-direction from $0$ to $L$, and its vibration is limited to the xy-plane.

Letting $y = y(x,t)$ be the position function of a point of the string, for a certain time $t$, then, as illustrated in Fig. 2.8, the out-of-plane displacement, $y$, arises from the tensile forces acting on the string, Fig. 2.8(b) and the inertial effect.

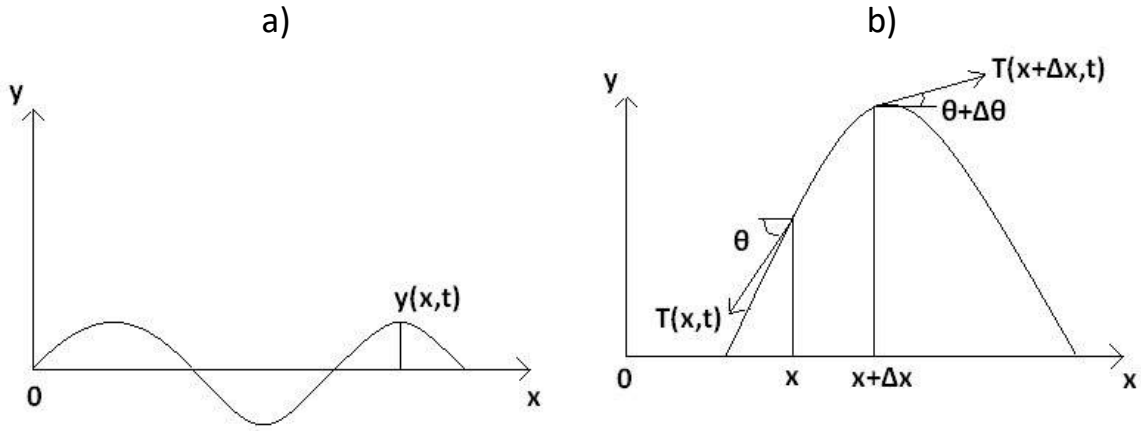


*Fig. 2.8 (a) Vibrating string and (b) forces acting on a differential element of the string.*

Neglecting the damping forces, such as air resistance and string weight, we can suppose that the string tension acts always tangentially and the mass per unit length ( $\lambda$) is constant.

Taking a segment of the string between $x$ and $x+\Delta x$, we apply the second law of Newton

$$F = ma\,, \tag{2.43}$$

where $F$ is the net force on the segment due to tension, $m$ is the mass of the string segment, and $a$ is the acceleration of the string. For a small $\Delta x$ subjected to tension $T$, the vertical component of Eq. 2.43 is [5]

$$T(x+\Delta x,t)\sin(\theta+\Delta\theta) - T(x,t)\sin(\theta) = \lambda\Delta x \frac{\partial^2 y\left(\bar{x},t\right)}{\partial t^2}\,, \tag{2.44}$$

where $\bar{x}$ is the centroid of $\Delta x$

If $\Delta x$ tends to zero, $x$ tends to $\bar{x}$, Eq. 2.44 can then be rewritten as

$$\frac{\partial V(x,t)}{\partial x} = \rho \frac{\partial^2 y\left(\bar{x},t\right)}{\partial t^2}\,, \tag{2.45}$$

where $V(x,t) = T(x,t)\sin(\theta)$.

For small angles of deformation, we can obtain

$$\frac{\partial^2 y}{\partial t^2} = c^2 \frac{\partial^2 y}{\partial x^2}\,, \tag{2.46}$$

where $c^2 = T/\lambda$ is the mechanical wave speed squared.

For a two-dimensional membrane element lying on the xy-plane, Eq. 2.44 may be written as [5]

$$\begin{aligned}\sigma dxdy\frac{\partial^2 z}{\partial t^2} &= \frac{\partial}{\partial x}\left(T_l dy\frac{\partial z}{\partial x}\right)dx + \frac{\partial}{\partial y}\left(T_l dx\frac{\partial z}{\partial x}\right)dy \\ &= T_l\left(\frac{\partial^2 z}{\partial x^2}+\frac{\partial^2 z}{\partial y^2}\right)dxdy\end{aligned}, \tag{2.47}$$

where $\sigma$ is the superficial mass density and $T_l$ the tension per unit length (also $\frac{\partial z}{\partial x}\approx \sin\theta \approx \tan\theta$, for small angles of deflection). Then,

$$\frac{\partial^2 z}{\partial x^2}+\frac{\partial^2 z}{\partial y^2}-\frac{1}{c^2}\frac{\partial^2 z}{\partial t^2}=0,$$

where $c^2 = T_l/\sigma$ and $z(x,y,t)=w(x,y,t)$ is the **out-of-plane displacement**; notice that also $c^2 = T/(A\rho)$, with $T$ being the loading tensile stress along the circumference of the plate, $A$ is the transverse area, and $\rho$ in this case represents the standard or volumetric mass density; further, $\sigma=\rho h$, where $h$ is the thickness of the membrane.

To find an expression that represents the vibration of a circular membrane, Eq. 2.47 is expressed in cylindrical coordinates (see Fig. 2.9)

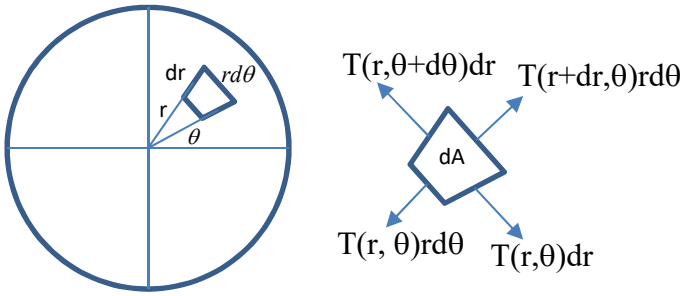


*Fig. 2.9 Acting forces over a circular area.*

$$\begin{aligned}\sigma r dr d\theta\frac{\partial^2 z}{\partial t^2} &= \frac{\partial}{\partial r}\left(Tr d\theta\frac{\partial z}{\partial r}\right)dr + \frac{1}{r^2}\frac{\partial}{\partial \theta}\left(T dr\frac{\partial z}{\partial \theta}\right)r d\theta \\ &= T\left[\frac{1}{r}\frac{\partial}{\partial r}\left(r\frac{\partial z}{\partial r}\right)+\frac{1}{r^2}\frac{\partial^2 z}{\partial \theta^2}\right]r dr d\theta\end{aligned},$$

so that

$$\frac{\partial^2 w}{\partial r^2}+\frac{1}{r}\frac{\partial w}{\partial r}+\frac{1}{r^2}\frac{\partial^2 w}{\partial \theta^2}-\frac{1}{c^2}\frac{\partial^2 w}{\partial t^2}=0\,. \tag{2.48}$$

To solve Eq. 2.48, we propose a solution by the separation of variables method

$$w(r,\theta,t)=M(r)O(\theta)N(t). \tag{2.49}$$

Calculating the differential terms, we obtain

$$\frac{\partial u}{\partial t}=M(r)O(\theta)N'(t),\quad \frac{\partial^2 u}{\partial t^2}=M(r)O(\theta)N''(t),$$
$$\frac{\partial u}{\partial r}=M'(r)O(\theta)N(t),\quad \frac{\partial^2 u}{\partial r^2}=M''(r)O(\theta)N(t)$$

$$\frac{\partial u}{\partial \theta} = M(r)O'(\theta)N(t) \quad , \quad \frac{\partial^2 u}{\partial \theta^2} = M(r)O''(\theta)N(t) \quad . \tag{2.50}$$

By substituting Eq. 2.50 into Eq. 2.48

$$M(r)O(\theta)N''(t) = c^2\left( M''(r)O(\theta)N(t) + \frac{1}{r}M'(r)O(\theta)N(t) + \frac{1}{r^2}M(r)O''(\theta)N(t)\right)$$

and regrouping the variables, this equation can be rewritten as

$$\frac{N''(t)}{c^2 N(t)} = \frac{M''(r)}{M(r)} + \frac{1}{r}\frac{M'(r)}{M(r)} + \frac{1}{r^2}\frac{O''(\theta)}{O(\theta)} = -k^2 , \tag{2.51}$$

where the equality to a positive constant $k^2$ is valid since each member depends on different variables and since this equation is valid for any $t$, $r$ and $\theta$. The negative sign is selected as to obtain propagating functions as solutions.

Then we can write

$$\frac{N''(t)}{c^2 N(t)} = -k^2,$$

which readily yields,

$$\begin{aligned} N(t) &= A\cos(kct) \\ &= A\cos(\omega t) \end{aligned} \tag{2.52}$$

where $A$ is an arbitrary constant, and the angular frequency is

$$\omega = kc.$$

Proceeding as before with the azimuthal part,

$$\frac{O''(\theta)}{O(\theta)} = -m^2,$$

so,

$$O(\theta) = B\cos(m\theta) + C\sin(m\theta),$$

with $B$ and $C$ are two other arbitrary constants. Now by assuming periodicity of $2\pi$, $\theta = \theta + 2\pi$, $m$ should be an integer. Also, by forcing symmetry in theta with respect to at least one diameter,

$$\begin{aligned} O(\theta) = B\cos(m\theta) + C\sin(m\theta) = O(-\theta) = B\cos(m\theta) - C\sin(m\theta)\,, \\ O(\theta) = C\cos(m\theta). \end{aligned} \tag{2.53}$$

From Eq. 2.51, then we write

$$\frac{M''(r)}{M(r)} + \frac{1}{r}\frac{M'(r)}{M(r)} - \frac{1}{r^2}m^2 + k^2 = 0\,,$$

and

$$r^2 M''(r) + rM'(r) + \left(k^2 r^2 - m^2\right)M(r) = 0\,. \tag{2.54}$$

We recognize Eq. 2.54 as the Bessel equation of order $m$. This type of equation has two independent solutions, (making a change of variable, $s = kr$)

$$M(r) = eJ_m(kr) + e'Y_m(kr),$$

where $e,\quad e'$ are arbitrary constants, and $J_m(kr),\quad Y_m(kr)$ are the Bessel functions of the first and second kinds, respectively, of order $m$, which are the two solutions of the second order differential equation.

Since $Y_n(kr) \to -\infty$ when $r \to 0$ (membrane center), this in practical terms is not feasible, and this solution is neglected; that is, we choose $e' = 0$,

$$M(r) = eJ_m(kr). \tag{2.55}$$

As the membrane is fixed to a circumferential frame, $M(kR) = 0$, for $t > 0$. This condition is fulfilled if $J_m(z_{mn}) = 0$, being $z_{mn}$ the positive zeroes of $J_m(z_n)$, with $z_{m1} > z_{m2} > z_{m3} > \ldots$; and thus

$$k_{mn} = \frac{z_{mn}}{R},$$

with $R$ the radius of the membrane, and $m = 0,1,2,\ldots$ and $n = 1,2,\ldots$

Substituting Eqs. 2.52, 2.54, and 2.55 into Eq. 2.49, we find a possible solution as

$$w_{mn}(r,\theta,t) = C_{mn}J_m(z_{mn}r/R)\cos(m\theta)\cos(\omega_{mn}t), \tag{2.56}$$

where

$$\omega_{mn} = k_{mn}c.$$

Therefore,

$$\omega_{mn} = \frac{z_{mn}}{R}\sqrt{\frac{T}{A\rho}}. \tag{2.57}$$

The radial nodes correspond to $m$ and the circle nodes (circumferential nodes) to $n$. The first zeros are given in Table 2.1.

| | $z_{mn}$ | | | | |
|---|---|---|---|---|---|
| | m=0 | 1 | 2 | 3 | 4 |
| n=1 | 2.41 | 3.83 | 5.14 | 6.38 | 7.59 |
| 2 | 5.52 | 7.02 | 8.42 | 9.76 | 11.06 |
| 3 | 8.65 | 10.17 | 11.62 | 13.02 | 14.37 |

*Table 2.1 Frequencies of vibration modes for a membrane.*

The order in frequency of the modes is 01 [no radial nodes, one circle node (along the circumference): fundamental mode], 11 [one radial node, one circle node (along the circumference): first harmonic mode], 21, 02, 31, 12, 41, 22, 03, 51, etc. These modes are further analyzed in next Chapter.

### 2.3.2 Vibration modes of a thin plate

In this section, we describe how to obtain the frequencies corresponding to the modes of vibration for a thin plate. A plate is considered as thin when the deformation is less than its thickness. A mode of vibration does not depend on time, that is, it is stationary.

Starting with the equation of the motion of an isotropic circular plate [6], the out-of-plane deflection can be expressed as

$$D\nabla^2\nabla^2 w + \sigma\ddot{w} = 0 \quad , \tag{2.58}$$

where $D = \frac{Eh^3}{12\left(1-\nu^2\right)}$ is the flexural rigidity. Here $E$ is the Young's modulus and $\nu$ is the Poisson's ratio. The temporal part is given as in the case of membranes, $w(\vec{r},t) = W(\vec{r})\cos(\omega t)$, where $\vec{r}$ is the position vector. Hence Eq. 2.58 yields

$$\nabla^4 W - k^4 W = 0\,,$$

with

$$k^4 = \frac{\sigma\omega^2}{D}. \tag{2.58p}$$

It is convenient to rewrite Eq. 2.58 as the fourth order differential equation

$$\left(\nabla^2 + k^2\right)\left(\nabla^2 - k^2\right)W = 0\,,$$

which in turn can be expressed as

$$\begin{matrix}\left(\nabla^2 - k^2\right)W = W_1 \\ \left(\nabla^2 + k^2\right)W_1 = 0\end{matrix}.$$

The first part is similar to the one appearing in a membrane; and when considering that the membrane is circular and is fixed along its circumference ($W(R) = 0, \quad \partial W(R)/\partial r = 0$), the complete solution is [7]

$$w_{mn}(r,\theta,t) = \left[A_{mn}J_m(k_{mn}r) + B_{mn}I_m(k_{mn}r)\right]\cos(m\theta)\cos(\omega_{mn}t)\,, \tag{2.59}$$

with $A$ and $B$ arbitrary constants and $I(kr)$ being the modified Bessel function of the first type. Also, $k_{mn} = \frac{z_{mn}}{R}$ is related to the roots of $J_m(z_{mn})I_{m+1}(z_{mn}) + I_m(z_{mn})J_{m+1}(z_{mn}) = 0$, with $m = 0,1,2,\ldots$ and $n = 1,2,\ldots$ In this way, by using Eq. 2.58p,

$$\omega_{mn} = \sqrt{\frac{D}{\sigma}}\frac{z_{mn}^2}{R^2}. \tag{2.60}$$

The first zeroes of the latter function are given in Table 2.2. The number of nodal diameters (radial nodes) is $m$ and of nodal circles (circumferential nodes) is $n$; the order of the vibration modes by frequencies is exactly the same as in the membrane.

| | $z_{mn}^2$ | | | | |
|---|---|---|---|---|---|
| | m=0 | 1 | 2 | 3 | 4 |
| n=1 | 10.22 | 21.26 | 34.88 | 51.04 | 69.67 |
| 2 | 39.77 | 60.82 | 84.58 | 111.01 | 140.11 |
| 3 | 89.10 | 120.08 | 153.81 | 190.30 | 229.52 |

*Table 2.2 Frequencies of vibration modes for a thin plate.*

### 2.3.3 Relationship between frequencies of the modes for a membrane and a thin plate

The ratio between consecutive frequencies of corresponding vibration modes are different for a thin plate and a membrane, Eq. 2.57 and Eq. 2.60; Table 2.3 shows the normalized values for both frequencies.

| | $\omega_{mn,plate}$ , $\omega_{mn,membrane}$ | | | | |
|---|---|---|---|---|---|
| $k$ | 0 | 1 | 2 | 3 | 4 |
| 1 | 1 , 1 | 2.081 , 1.593 | 3.414 , 2.136 | 4.994 , 2.647 | 6.817 , 3.149 |
| 2 | 3.893 , 2.295 | 5.935 , 2.917 | 8.279 , 3.500 | 10.862 , 4.049 | 13.709 , 4.589 |
| 3 | 8.787 , 3.598 | 11.754 , 4.23 | 15.056 , 4.831 | 18.620 , 5.402 | 22.457 , 5.962 |

*Table 2.3 Normalized frequencies of vibration modes for a thin plate [8] and a membrane [9].*

As noticed from the last table, by measuring the ratios of consecutive frequencies is straightforward to show whether the object under test corresponds to a membrane or to a thin plate. Additionally, observe that the frequency modes for a plate are more separated than for a membrane.

## 2.4 References


1. K. J. Gasvik, *Optical Metrology*, 3rd Ed., John Wiley and Sons, Sussex, UK (2003).
2. C. Mares, *Medición de velocidad de fluidos en 3D*, Centro de Investigaciones en Óptica, México (2010).
3. W. Navidi, *Estadística para ingenieros y científicos*, 6th Ed., MC Grawhill (2008).
4. H. P. Hsu, *Análisis de Fourier*, Pearson, Michigan (1970).
5. J. Reddy, *Theory and analysis of elastic plates and shells*, Taylor and Francis Group (2007).
6. A. W. Leissa, *Vibration of plates*, Ohio State University, Columbus, Ohio.
7. Wikipedia, "Vibrations of a circular membrane", " https://en.wikipedia.org/wiki/Vibrations_of_a_circular_membrane".

# 3. NUMERICAL SIMULATIONS

With the purpose of finding the optimal parameters of the methods used in this work, fringe projection (FP) and digital image correlation (DIC), we carry out numerical simulations using Matlab. Several parameters are tested and the results are analyzed by computing the relative error.

## 3.1 FRINGE PROJECTION, FP

### 3.1.1 Simulation procedure

First, the period and size of the image are evaluated; we create a matrix where each value corresponds to the carrier frequency given by Eq. 2.1; this is the reference image. To create the object image (deformed image), Eq. 2.8 is employed, where the modulation phase due to the objects is included.

Part of our analysis corresponds to the addition of noise into the images (in the phase term); a random value between 0 and $\pi$ rad is selected. The level of noise is selected by using a low pass filter by Fourier transform. Then the noise level added to the reference is different from that added to the deformed image. Fig. 3.1(a) shows the reference image and (b) shows the deformed image. The object changes locally the period of the grating; the grating is deformed following the shape of the object and the noise causes blurring of the images. Figures 3.1(c) and (d) are cross-sections in the horizontal direction of the reference and deformed images, respectively.

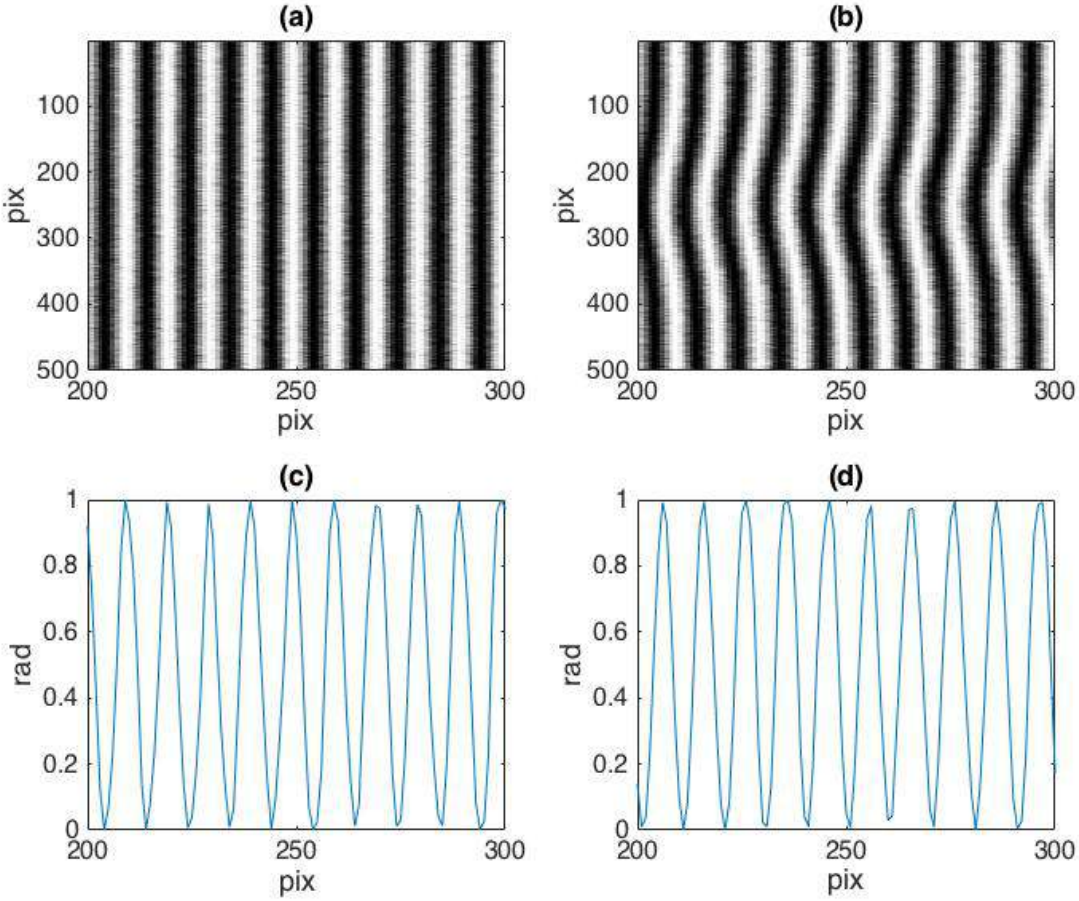


*Figure 3.1 Reference image, (a), deformed image, (b), and their respective cross-sections, (c) and (d). The images present noise, it is different for each image. The period is 10 pix per cycle, the object has a Gaussian profile with a scale of 10 pix/cm, the angle between the projector and the sensor is 20°.*

The next step is to process the images with Fourier transform, explained in Section 2.1.2. The result is a matrix with the phase difference between the two images, this phase is proportional to the topography of the object expressed in radians; Fig. 3.2(a) shows a cross-section of it. Notice that the phase is wrapped.

To unwrap the phase, the algorithm described in section 2.1.3 is utilized. The unwrapped phase is shown in Figure 3.2(b), note that the phase profile becomes continuous.

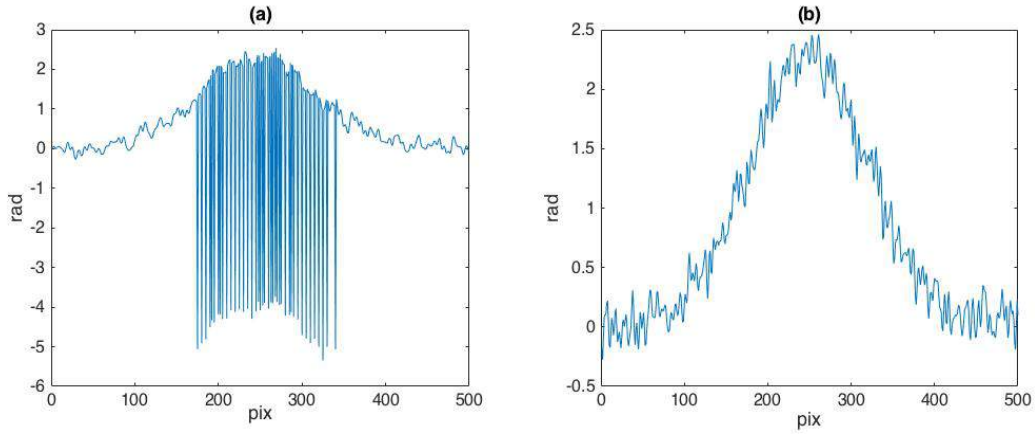


*Figure 3.2 An example of unwrapped phase function, (a) wrapped phase, and (b) unwrapped phase.*

Finally, we recover the object height distribution by using Eq. 2.8. Figure 3.3 shows both the original and the recovered values; note the object is similar, but the recovered object presents noise. The noise is added with the purpose to illustrate how the noise affects the method.
To compare the results, we use the standard deviation [1] to calculate the percentage relative error, using the maximum value of the original height as the reference value (object's height is 10 pix).

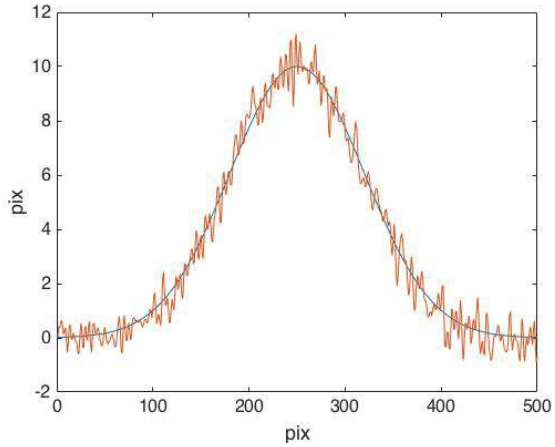


*Figure 3.3 Comparison between original and recovered height profiles.*

### 3.1.2 Period

The period is the way to sample the object; the object modulates the cosine function and the comparison between the original function and the deformed function gives the object height. Accuracy of the recovered height depends on the value of the period.
In Fig. 3.4(a), for periods bigger than 3.6 pix (pixel), the error is relatively small; for shorter values, the error increases, as shown in Fig. 3.4(b)—notice the oscillations for smaller periods, which arise from undersampling of the images, as described below.

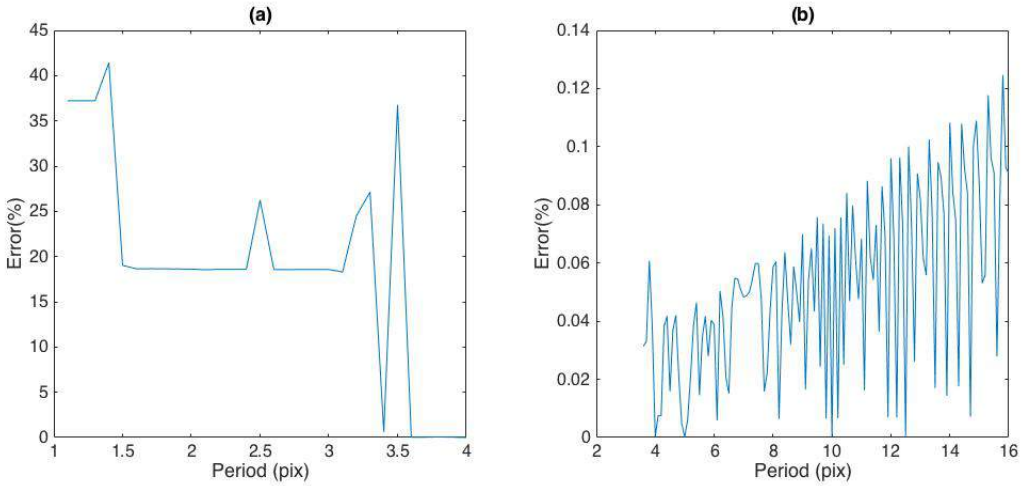


*Fig. 3.4 Error in FP as a function of period; the projection angle is 20°; (a) range with small periods and (b) with large periods.*

Figure 3.5 illustrates one example of images with undersampling [reference image, (a) and (c), and deformed image, (b) and (d)]. Note that the wave crests are truncated periodically and causes information loses. The reference image consists of a sinusoidal wave ( $im(j,i) = 0.5\cos\left(\frac{2\pi i}{p} + 0.5\right)$ ), where $p$ is period and $i$, $j$ are dummy indices, Fig. 3.5(a); the period is too small that sampling fails, so the result is a different wave, (d).

The Nyquist theorem states that to recover a band-limited signal, the sampling frequency must be at least twice the bandwidth.

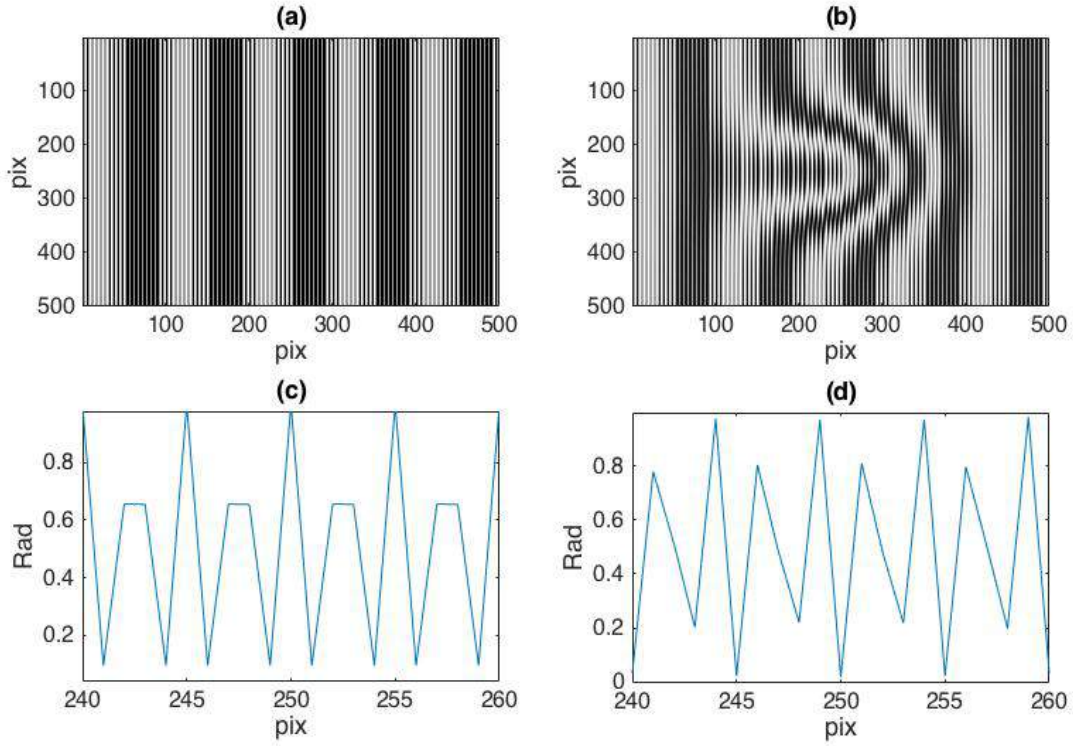


*Fig. 3.5 An example of the projected lines on the reference plane and on the object; (a) reference image, (b) object image, (c) cross-section of (a), and (d) cross-section of (b).*

### 3.1.3 Projection angle

The angle between the camera and the projector influences the sensitivity of the setup; small values of angles imply small sensitivity, and vice versa.

Inspecting Fig. 3.6, the error is high when the angle is small, then the error has a behavior resembling a logarithm function, Fig. 3.6(a), until the error takes its minimum value; beyond this, the error has a behavior like an exponential function, Fig. 3.6(b).

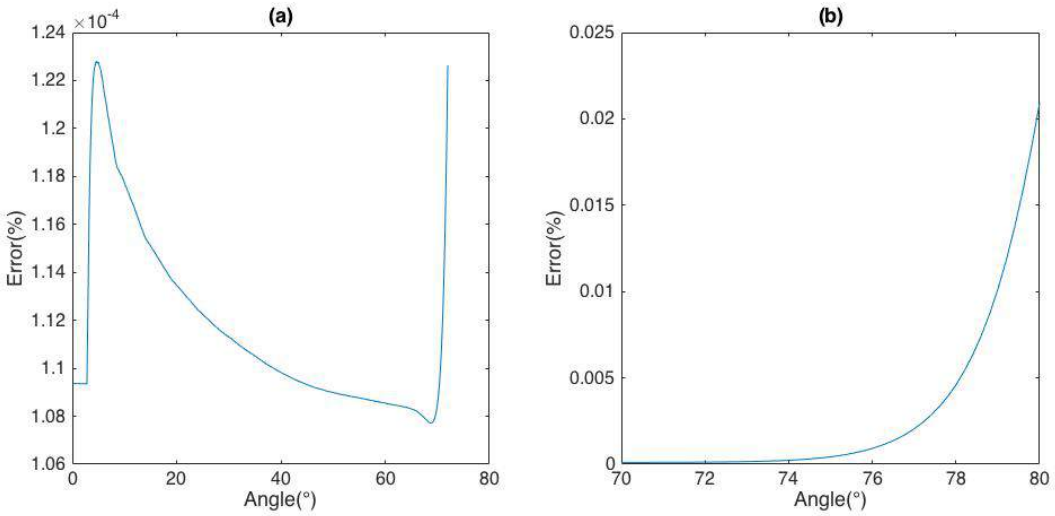


*Fig. 3.6 Simulation of error in FP as a function of projection angle; a period of 10 pix is assumed; (a) small values of angle and (b) larger values of angles, within 70° and 80°.*

### 3.1.4 Noise level

In this section we analyze the influence of noise level on the accuracy of FP. We consider that the period is 10 pix and the projection angle, 20°, and that noise is added to the phase term (10% level, where 100% is $2\pi$ rad); the noise in the reference image is different from the noise in the deformed image.

An example of the resultant recovered profile object of the fringe projection method is illustrated in the Fig. 3.7; the original object shape corresponds to a Gaussian profile. The resultant object is similar to the original, but it presents noise.

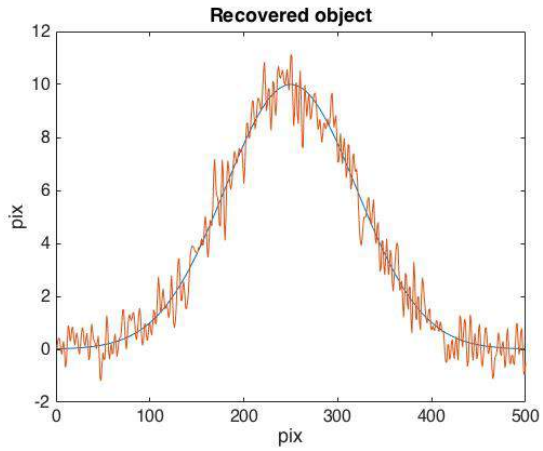


*Fig. 3.7 Prescribed and recovered object profile, by FP. The recovered image presents noise.*

In Fig. 3.8 we show the effect of the noise on the error; the error increases linearly until a level of 18 %; after that, the error increases exponentially; the noise level has to be low for a satisfactory result.

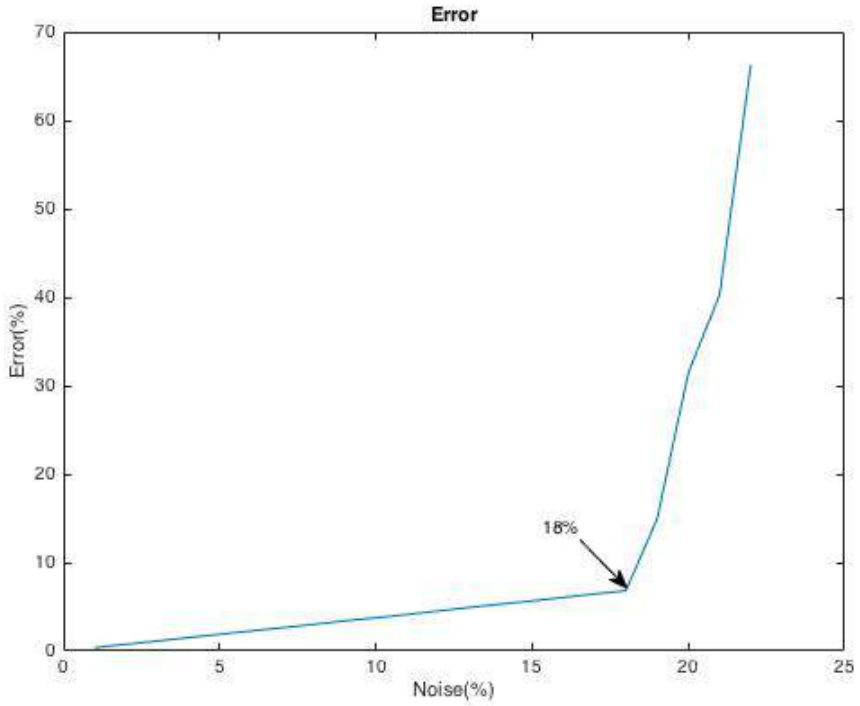


*Fig. 3.8 Error simulation of FP, adding noise within phase term of images, with period of 10 pix and projection angle of 20°.*

### 3.1.5 Conclusions

The period has to be large enough to correctly sample the object and small enough to capture the details of the object; however, for small values, the error tends to be large.
It is recommended that the projection angle be within a range of 10° to 50°; small values should be used for low sensitivity setups.

## 3.2 DIGITAL IMAGE CORRELATION, DIC

### 3.2.1 Simulation procedure

A reference image is initially embedded with zeroes. By using the random function of Matlab; we generate the coordinates (x,y) for each particle and assign a value of unity to these positions.
The reference image is divided into windows of 24x24 pix and the algorithm creates a matrix with the values of the displacements for each window.
The algorithm takes one window at a time, Fig. 3.9(a); then it uses the Fourier transform to calculate the convolution of the window and a similar window with a 3D Gaussian distribution centered in the image. The result is a new window with Gaussian particles centered on each point particle of the original window, (b), and the new window is placed in a new image in the same place where the original was taken.
With the same procedure, the algorithm uses the displacements matrix and the translation property of the Fourier transform to create the deformed image, (c).

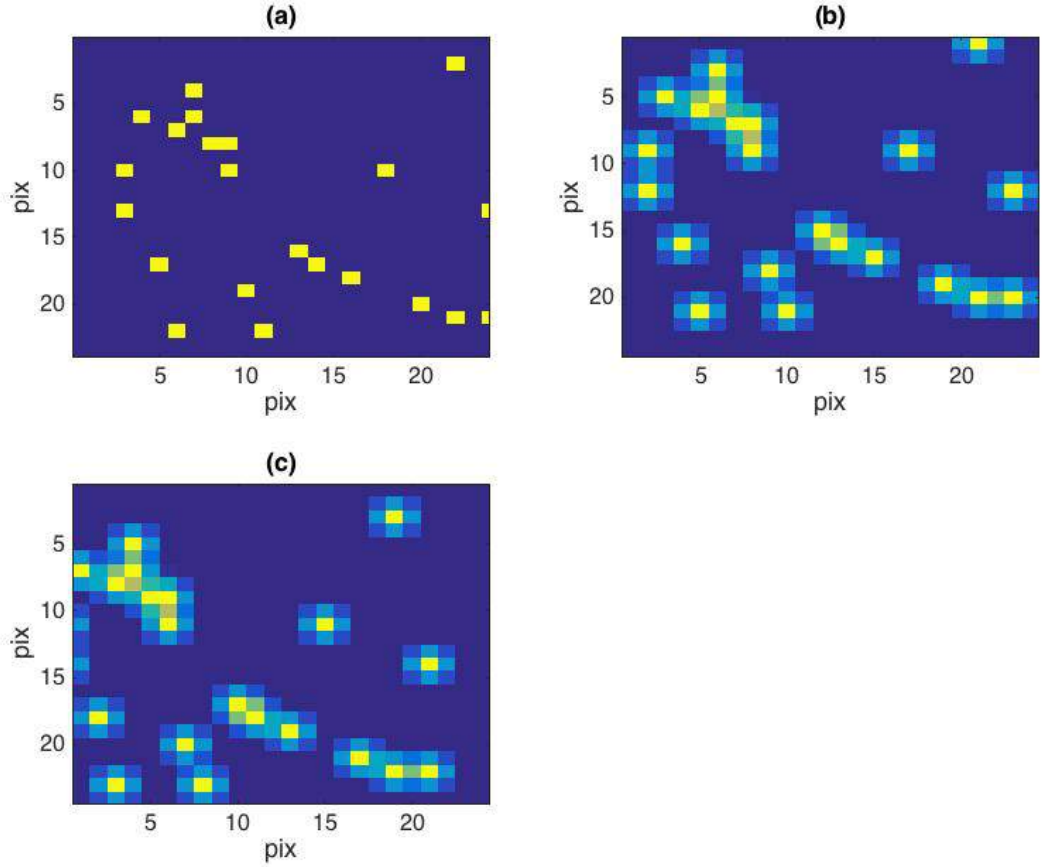


*Figure 3.9 (a) A 24x24 pix image with a random distribution of particles of diameter 1 pix, b) particles of (a) are converted into Gaussian particles using the convolution theorem and (c) the particles of (b) are displaced using the translation property of Fourier transform.*

Once the images, reference and displaced, have been created the algorithm uses them to calculate their correlation, as described in Section 2.3. The result of the correlation corresponds to the calculated displacements between the images; these displacements are placed in two matrixes, one for x-direction and another for y-direction.
To calculate the error of DIC; we use the discrete standard deviation [1] using the matrix with the original displacements and the matrix with the calculated displacements; the result is the percentage relative error for both x-direction and y-direction displacements.

### 3.2.2 Point particles

The first test is with point particles (diameter of 1 pix), using DIC between the reference and deformed image, to find the optimum number of particles (this parameter is represented by the fill percentage that is defined as the ratio between the total number of point particles and the number of pixels of the image).
Figure 3.10 shows the error of DIC, (a) for the displacements in x-direction and (b) for the displacements in y-direction; note that for fill percentages less than 2.5, the error is almost zero.

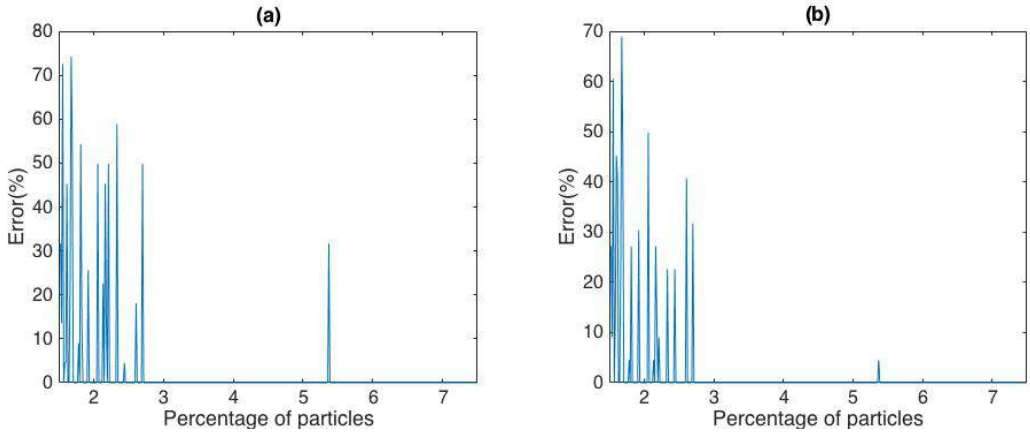


*Fig. 3.10 DIC error simulation; we assume displacements of -2 pix in x-direction, 2 pix in y-direction and point particles; (a) error in x-direction and (b) error in y-direction.*

### 3.2.3 Gaussian particles

We proceed to the next case: using Gaussian particles instead of point particles, with the purpose to analyze the behavior of the error. Consider a Gaussian function with unit amplitude and centered at the origin

$$v(u) = e^{\frac{-u^2}{2\sigma^2}},$$

where $\sigma$ is the standard deviation. Taking the particle's radius ($r$) as the value of $u$ that correspond to 30% of the maximum value of $v(u)$, it gives

$$\sigma = \sqrt{\frac{-r^2}{\ln 0.3}}.$$

For sections 3.2.3 and 3.2.4, we set the diameter as 2 pix. In section 3.2.5 we analyze how the diameter of the particle affects the accuracy of DIC.

Using particles of 2 pix, the error of DIC, Fig. 3.11, shows a similar behavior with respect to the latter case, the error decreases while the percentage of particles increases; the error in x-direction, (a), and y-direction, (b), are similar.

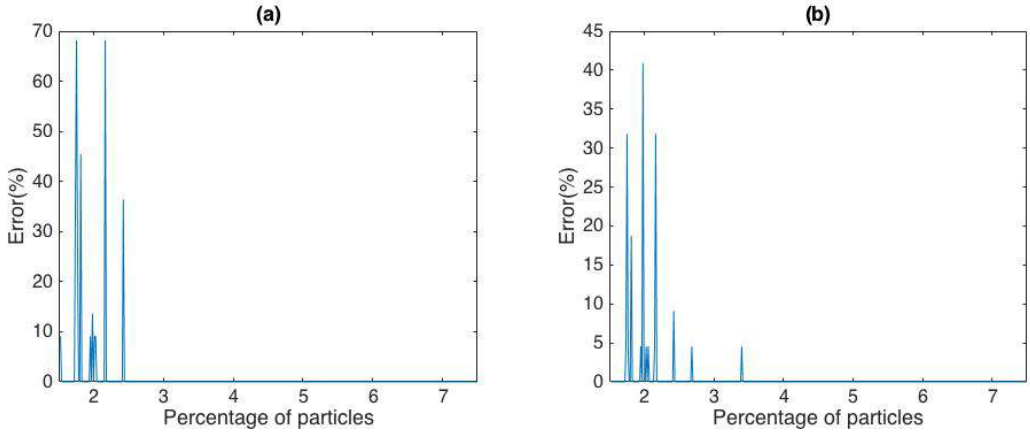


*Fig. 3.11 A DIC simulation with displacements of -2 pix in x-direction and 2 pix in y-direction and Gaussian particles; (a) error in x-direction and (b) error in y-direction. Diameter of particle is 2 pix.*

The previous test shows the error of DIC assuming a constant displacement; the next test is with randomly displaced particles, shown in Fig. 3.12, (a) for the x-direction, and (b) for y-direction. The magnitude of the error is lower than particles constantly displaced (only integer values are allowed), because the displacements of every group of particles are chosen randomly ranging from zero to a certain maximum value, therefore in this test most of the displacements are smaller than the particles constantly displaced.

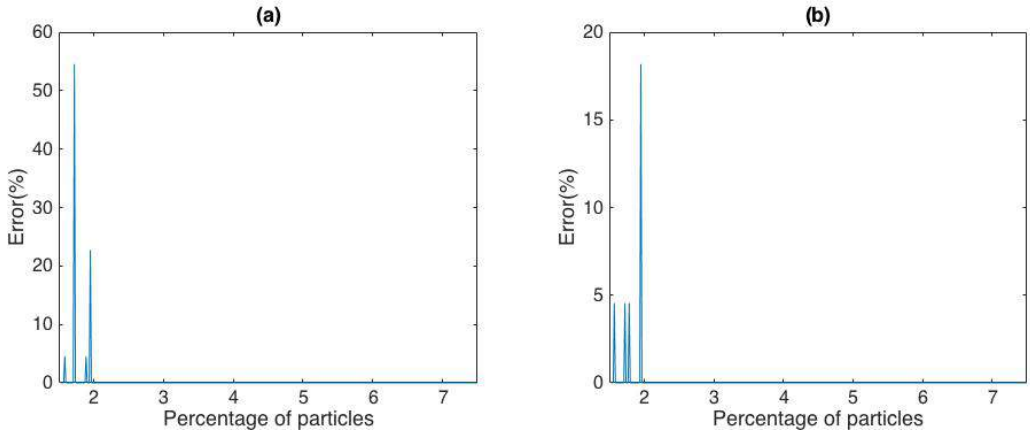


*Fig. 3.12 A DIC simulation with displacements within a range between 0 and -2 pix in x-direction and between 0 and 2 pix in y-direction, for Gaussian particles; (a) DIC error in x-direction and (b) DIC error in y-direction. Diameter of particles is 2 pix.*

### 3.2.4 Displacements in fractions of pixels

Consider the case when the particles are displaced in fractions of pixels, the displacements are randomly chosen within a range of 0 and 2 pix for x-direction, Fig. 3.13(a), and -2 and 0 pix for y-direction, Fig. 3.13(b).

Notice that the error of DIC takes high values when the fill percentage is relatively small; when the fill percentage increases, the error of DIC shown a linear tendency.

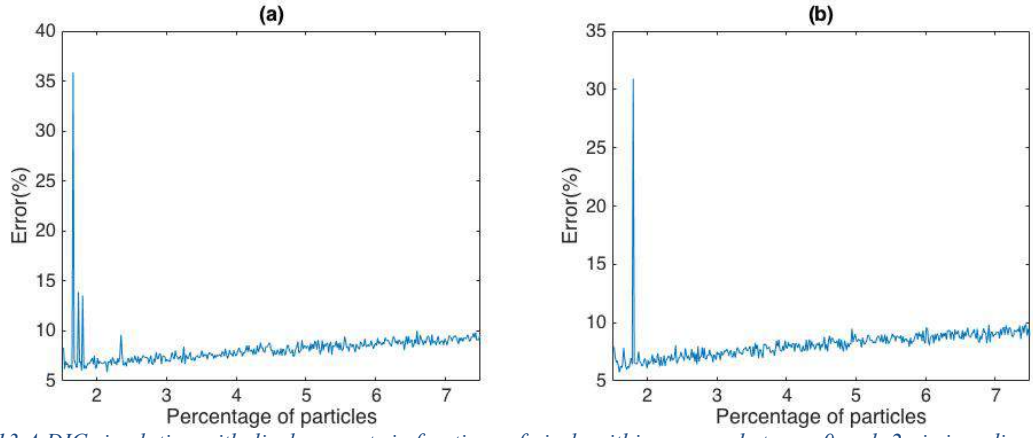


*Fig. 3.13 A DIC simulation with displacements in fractions of pixels within a range between 0 and -2 pix in x-direction and between 0 and 2 pix in y-direction; Gaussian particles are assumed; (a) DIC error in x-direction and (b) DIC error in y-direction. Diameter of particle is 2 pix.*

### 3.2.5 Particle diameter

It is necessary more information to take a decision about the appropriate number of particles; note that the diameter of the Gaussian particles affects indirectly the filling percentage. Then, the error is computed as a function of these two variables: filling percentage and particle diameter.

Figure 3.14 shows the error of DIC with random integer displacements; (a) shows the error for displacements in x-direction, and (b) the error for the displacements in y-direction.

The error of DIC increases for large fill percentage and large particle diameters; both conditions reduce the number of spatial structures that are essential for correlation to work.

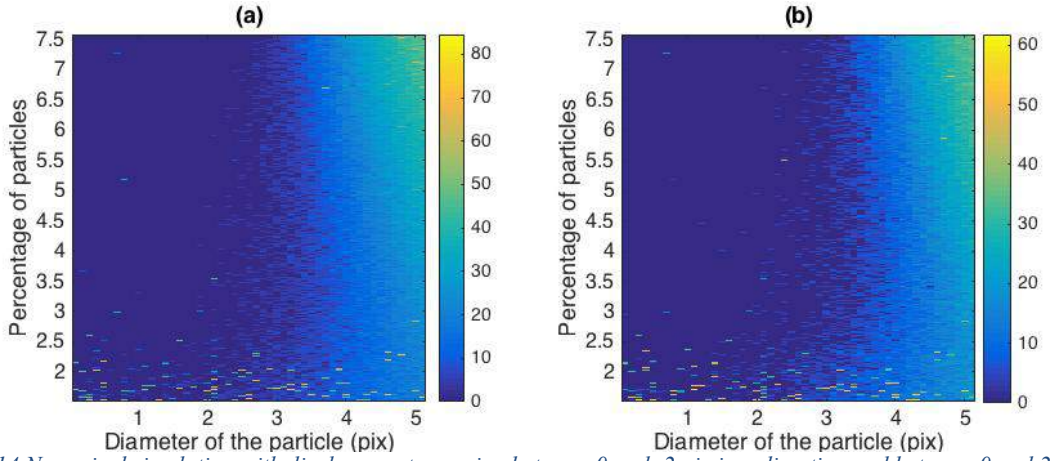


*Fig. 3.14 Numerical simulation with displacements ranging between 0 and -2 pix in x-direction and between 0 and 2 pix in y-direction; (a) DIC error in x-direction and (b) DIC error in y-direction. Integer displacements are assumed.*

Figure 3.15 shows the same test as before, but assuming random fractional displacements [(a) for x-direction and (b) for y-direction]; as the latter case, the error of DIC increases with the fill percentage and the particle diameter, but its magnitude is smaller.

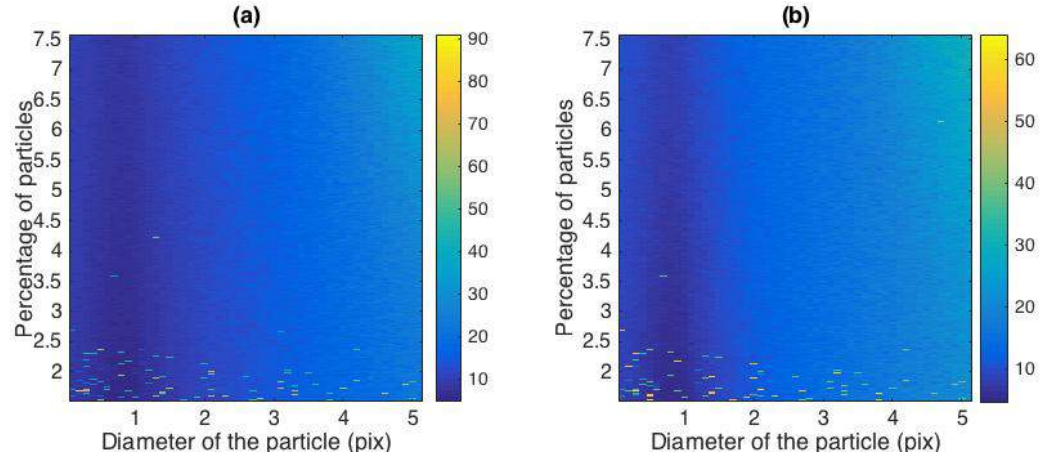


*Figure 3.15 Numerical simulation with fractional displacements within a range between 0 and -2 pix in x-direction and between 0 and 2 pix in y-direction; (a) DIC error in x-direction and (b) DIC error in y-direction.*

### 3.2.6 Magnitude of displacements

To illustrate how DIC is affected by the magnitude of the displacements, in Fig 3.16 we present the DIC error for a test with a filling percentage of 3.5% and Gaussian particles of diameter of 2

pix. The image is divided into windows of 24x24 pix and each window has a random integer displacement between 0 and the maximum value of displacements.
Figure 3.16(a) shows the error for negative displacements and (b) positive displacements.

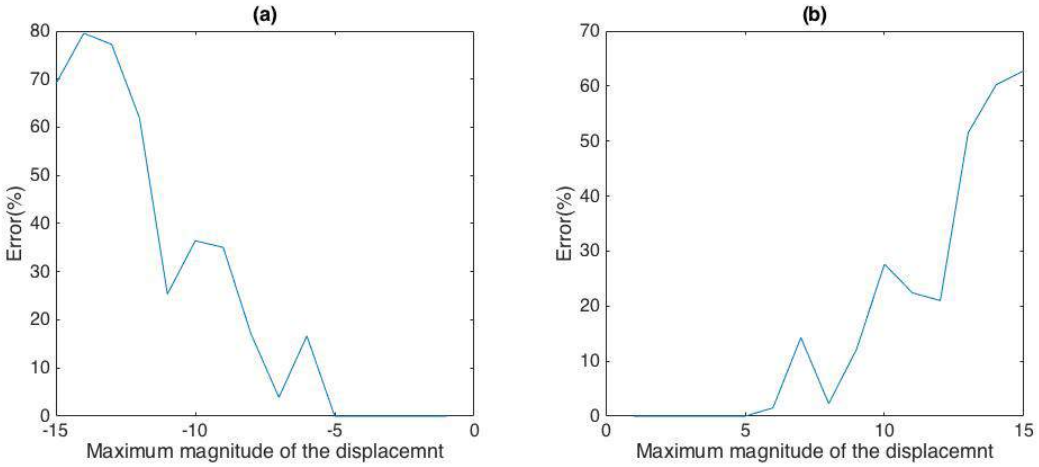


*Figure 3.16 DIC simulation with Gaussian particles. Diameter of particle is 2 pix; DIC error using (a) negative displacements and (b) positive displacements.*

### 3.2.7 Conclusions

To avoid high values of error in DIC, the fill percentage must be between 3% and 4%. Also, the diameter of the particle should be selected between 1 and 2 pix.
Besides, relatively small displacements produce low errors. To assure that displacements are not too large, the time between recordings of consecutive images should be selected accordingly.

## 3.3 VIBRATION OF A CIRCULAR PLATE

In this section, we present an analytical and numerical analysis of a vibrating plate. We obtain the spatial distributions of various resonance modes and their corresponding frequencies, according to section 2.3.
We consider a circular membrane of aluminum alloy whose properties are shown in Table 3.1.

| Properties | Value | Units |
|---|---|---|
| Radius | 147.5 | mm |
| Thickness | 0.7 | mm |
| Poisson ratio | 0.33 | - |
| Young's modulus | 6.96E+09 | Pa |
| Density | 2770 | $kg/m^3$ |

*Table 3.1 Mechanical properties of the plate.*

### 3.3.1 Simulations in Matlab

We simulate the spatial distribution of each mode of vibration by Matlab, according to the theory described in Section 2.3.2.

The simulation for each normal mode of vibration (Figure 3.17(a) corresponds to the fundamental mode 01; other modes are depicted in (b) mode 02, (c) mode 11, (d) mode 12, (e) mode 21, (f) mode 22, (g) mode 31, and (h) mode 32.
The first number of the modes corresponds to the number of radial nodal lines and the second number corresponds to the number of circumferential nodal lines (circular peaks). In this way, mode 01 displays just one peak, with the nodal line along the plate´s circumference.

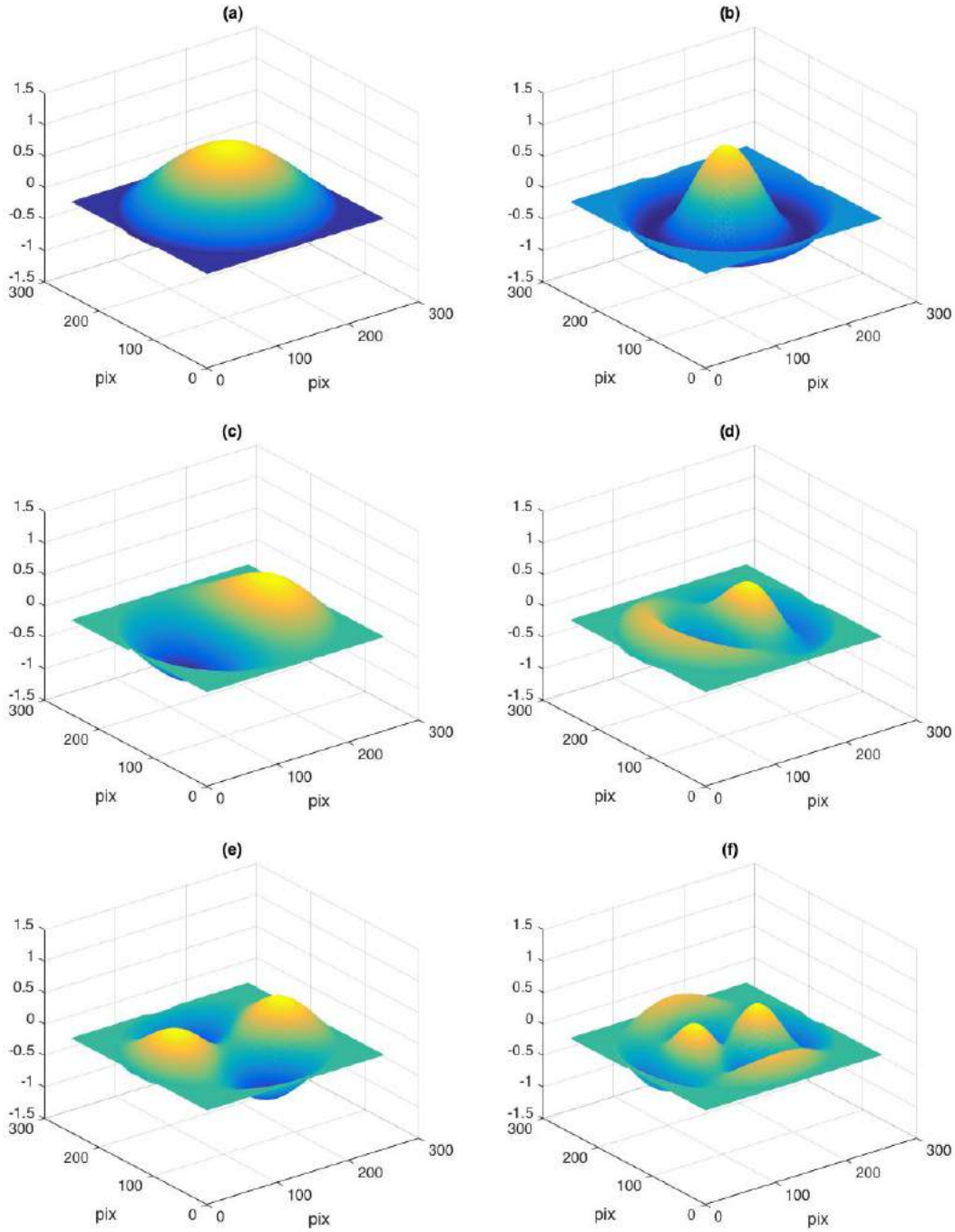

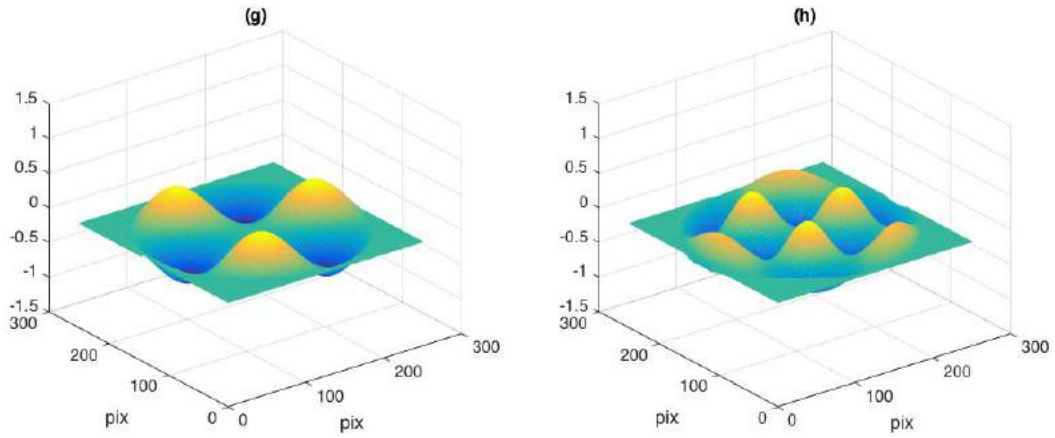


*Fig. 3.17 Normal modes of vibration of a circular plate, (a), (b), (c), (d), (e), and (f) correspond to the vibration mode 01, 02, 11, 12, 21, 22, 31, and 32, respectively. Simulation in Matlab with unitary amplitude at t=0.*

To obtain the frequencies for each mode, we use Eq. 2.60 and the results are presented in Table 3.2; they are in order regarding frequency.

| Mode | Frequency (Hz) |
|---|---|
| 01 | 80.09 |
| 11 | 164.6 |
| 21 | 248.64 |
| 02 | 312.18 |
| 31 | 321.13 |

*Table 3.2 Frequencies of first vibration modes using Eq. 2.98 and table 3.1.*

### 3.3.2 Modal analysis by ANSYS

By using ANSYS, the circular membrane mentioned in section 3.3.1. can also be analyzed. The Modal analysis yields the natural frequencies for each vibration mode and the distribution of heights.

Table 3.3 includes the natural frequencies for the first five resonance modes computed by ANSYS. When comparing these values to those in Table 3.2, we can observe some discrepancies, which arise mainly from the types of parameters used for modelling the mesh.

| Mode | Frequency (Hz) |
|---|---|
| 01 | 81.755 |
| 11 | 170.13 |
| 21 | 279.08 |
| 02 | 318.24 |
| 31 | 408.3 |

*Table 3.3 Frequencies of the vibration modes using the Modal analysis of ANSYS and table 3.1.*

The distribution, given by ANSYS, of heights is shown in Fig 3.18, (a) mode 01, (b) mode 11, (c) mode 21, (d) mode 02, (e) mode 31, (f) mode 12, and (g) mode 41.

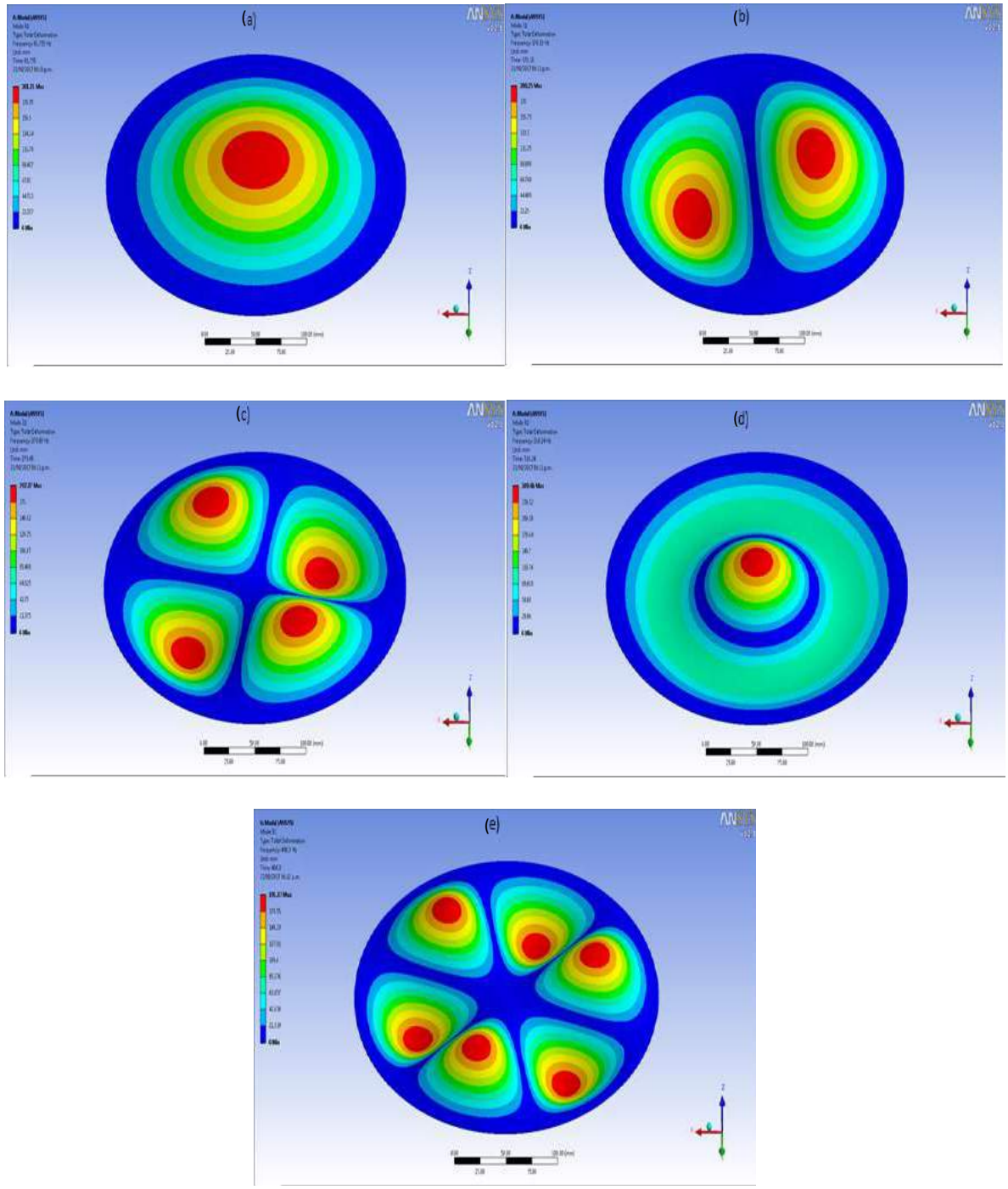


*Fig. 3.18 Normal modes of vibration of a circular membrane, by modal analysis of ANSYS; (a) mode 01, (b) mode 11, (c) mode 21, (d) mode 02, and (e) 31.*

### 3.3.3 Conclusions

The resonance frequency in plates varies inversely with thickness and diameter. On the other hand, for membranes, the frequency is additionally proportional to the applied tension.
The frequencies of the modes obtained with analytic (Eq. 2.60) and numerical (ANSYS) simulations are similar, see Table 3.2 and Table 3.3.

## 3.4 Conclusions

Regarding FP, it is recommended the use of the smallest period in order to increase the sensitivity of the technique; besides, a small projection angle is preferred to avoid the appearance of shadows.
In connection with DIC, important points to be considered are: use of particles of diameter of about 2 pix, and avoid displacements larger than around 8 pix. Enhancement of the naturally surface speckle is also recommended, through the use of relatively large projection angles (tending to the grazing condition) and the application of surface spraying.
For experimental measurements, the highest resonance frequency should be less than 1/10th the camera frame rate, which in this report is 5000 Hz. By measuring the ratio of consecutive resonance frequency values, it can be readily found whether the object corresponds to a thin plate (where the displacement is smaller than the thickness) or to a membrane.

## 3.5 References

1. W. Navidi, *Estadística para ingenieros y científicos*, 6th Ed., McGrawhill (2008).

# 4. EXPERIMENTAL ANALYSIS

The experimental results consist of two parts; the first part is a test of thin plates and the second part, of membranes. We analyze different materials of objects (latex, rubber, leather and aluminum) and different types of loading (point and uniform distributed load). In these results, we have used a combination of FP and DIC by resorting to color encoding.
Time series of snapshots covering a whole period of vibration are included for each mode of vibration.

## 4.1 EXPERIMENTAL SETUP

The object under test experiences in general two types of deformation, in-plane and out-of-plane. The experimental setup is configured to capture the two types of deformation in the same capture, using color codification. Setup's configuration is shown in Fig. 4.1.
The object is deformed either with a speaker (uniform loading) or a shaker (single-point loading). A synchronization signal is generated with a function generator and then is sent to an amplifier, and ultimately is made to drive the speaker or the shaker; the object is illuminated by a combination of a digital projector (Epson PowerLite 1776W WXGA, 3000 lm) and a matrix of red LEDs (540 LEDs per panel, 50 mW each, 50 V, 1 A). The projector projects an image with binary blue/black fringes (square-wave profile). To register images, we use a color high-speed camera, Photron Mini UX100 (1000x1280 pix at 5000 fps), which includes a Bayer filter.
The blue component of the RGB images correspond to the FP signal (Section 2.1), and the red component to DIC signal (Section 2.2). The software for FP is developed in Matlab and the software for DIC is proVISION by IDT.

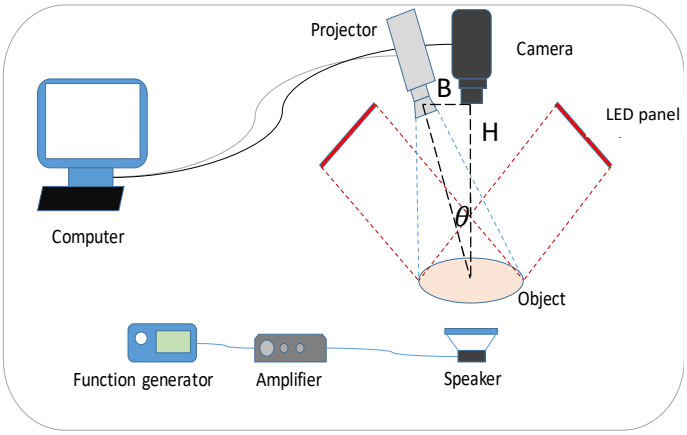


*Fig. 4.1 Setup's configuration.*

## 4.2 LEATHER PLATE

### *4.2.1 LEATHER DRUM (17-CM DIAMETER) DRIVEN BY SPEAKER*

First, for comparison reasons, we carry out some measurements by FP and DIC, but separately. This is done by using a leather drum. We use a speaker to apply uniform acoustic pressure over the drum (Fig. 4.2), and both methods, FP and DIC, are tested separately. Later, the same

measurements are performed but using the FP-DIC technique (simultaneity of measurements). The properties of the drum are shown in Table 4.1.

*Fig. 4.2 Leather drum (17-cm diameter).*

| Properties | Value | Units |
|---|---|---|
| Radius | 83.25 | mm |
| Thickness | 0.2032 | mm |
| Poisson ratio | 0.33 | - |
| Young modulus | 1.6911E+5 | Pa |
| Density | 683.5168 | $kg/m^3$ |

*Table 4.1 Properties of drum.*

To locate the vibration modes, we sweep the frequency of the signal that drives the speaker continuously until observing when the amplitude of displacement presents a maximum value.
By using the experimental or real frequencies for each mode and the Poisson's ratio, we calculate the Young's modulus, (Eq. 2.60), and then we obtain the theoretical harmonic frequencies. These values are shown in Table 4.2. The values do not agree exactly because of several causes: non-uniformity and uncertainty of parameters and weak-modeling of both loading and boundary conditions.

| Mode | $f_{theoretical}$ (Hz) | $f_{real}$ (Hz) |
|---|---|---|
| 01 | 229.0 | 229 |
| 11 | 470.7 | 492 |
| 21 | 710.9 | 659 |
| 02 | 892.6 | 742 |

*Table 4.2 Vibration mode frequencies.*

First we present results of FP, then results of DIC, and finally results of FP-DIC with simultaneity.

#### *4.2.1.1 Separated FP*

In this section, we firstly describe an example of FP, step by step. Table 4.3 shows setup's parameters of this test.

| $B$ (mm) | $H$ (mm) | $\theta$ (°) | $p$ (mm) |
|---|---|---|---|
| 160 | 407 | 21.5 | 1.24 |

*Table 4.3 Setup parameters.*

A sample original recorded image is shown in Fig. 4.3(a); by applying Fourier transform to the original image, we have (b); then, we filter one lobe with object information, and by applying inverse Fourier transform to the filtered result, we can calculate the phase map, (c). In a last step, we calculate the displacement field, in millimeters, (d). Notice that to obtain the displacement map, a filtered mask has been applied to filter out any information outside the circle of interest.

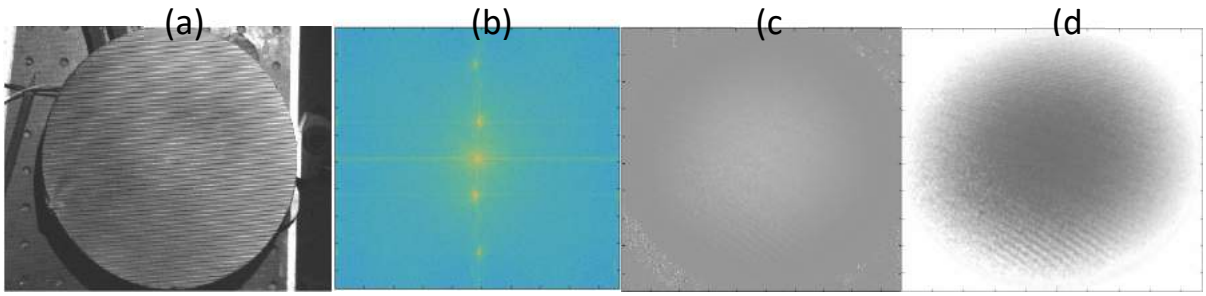


*Fig. 4.3 Example of FP; (a) original image, (b) Fourier transform of original image, (c) phase image, and (d) displacements in millimeters.*

Figure 4.4 illustrates cross-sections of the previous example, at different instants. Each part corresponds to a different level of power supply of the amplifier that drives the speaker. In part (a) we show mode 01 when the power supply is set to the maximum value (18 V); (b) corresponds to 9 V, and (c) is for 4.5 V. Notice that mode 01 follows the expected parabolic-like profile, with some content of noise. Further, we can observe that the maximum out-of-plane component of displacement (**OOPCD**) of a vibration mode is not proportional to the power supply.

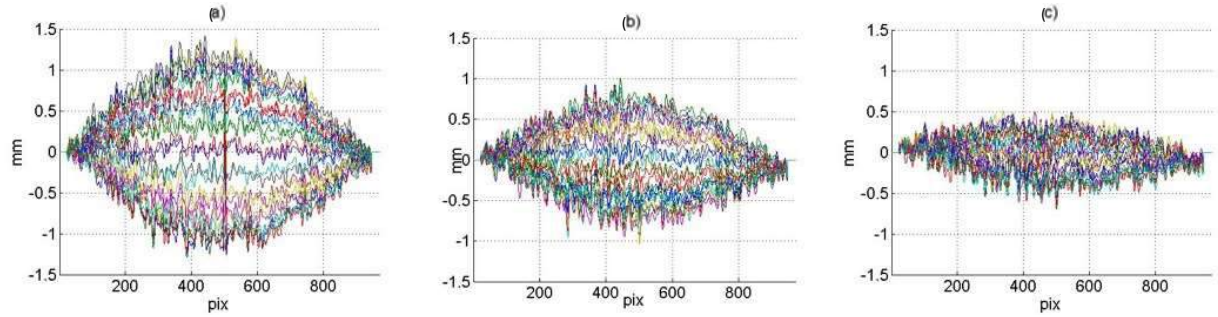


*Fig. 4.4 Time cross-sectional views of vibration mode 01, for different levels of amplifier voltage. (a) 18 V, (b) 9 V, and (c) 4.5 V.*

Similarly, time cross-sectional views for modes 11, 21 and 02 are shown in Fig. 4.5 (corresponding frequencies at 229, 492, 659 and 742 Hz, respectively). As shown, these modes are not pure modes, but a mixture of modes, where the predominant mode corresponds to the actual mode. Also, the maximum of displacement decreases with mode frequency.

In the next section, we include a description of each mode and maps with their spatial displacement distribution (first, out-of-plane and then in-plane).

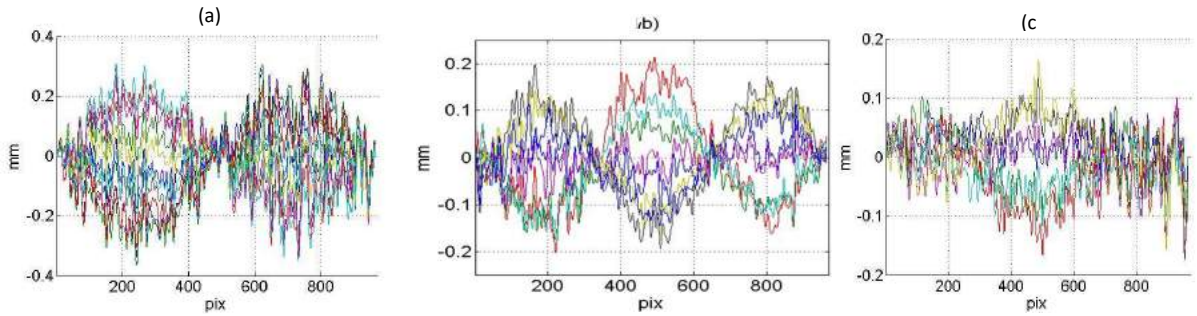


*Fig. 4.5 Cross-sections of modes (a) 11, (b) 21, and (c) 02.*

#### 4.2.1.1.1 Results

Here, we present the spatial distributions of OOPCD for the first 4 modes of resonance. More modes are not included because their displacement is beyond the resolution of FP, which is basically that arising from the Fourier transform phase method, one-twentieth of the period; for this test, it is around 60 μm.

The displacements are represented in color, where blue indicates displacements toward the camera, and red, receding from it. The units of the images' colorbar are millimeters.

##### 4.2.1.1.1.1 Mode 01 at **229 Hz**, 17-cm diameter drum

Mode 01 is located at 229 Hz. Fig. 4.6 shows snapshots covering a cycle of vibration. The behavior of the measured OOPCD resembles the theoretical ones: one azimuthal or circumferential node (along the fixed boundary of the drum) and zero radial nodes.

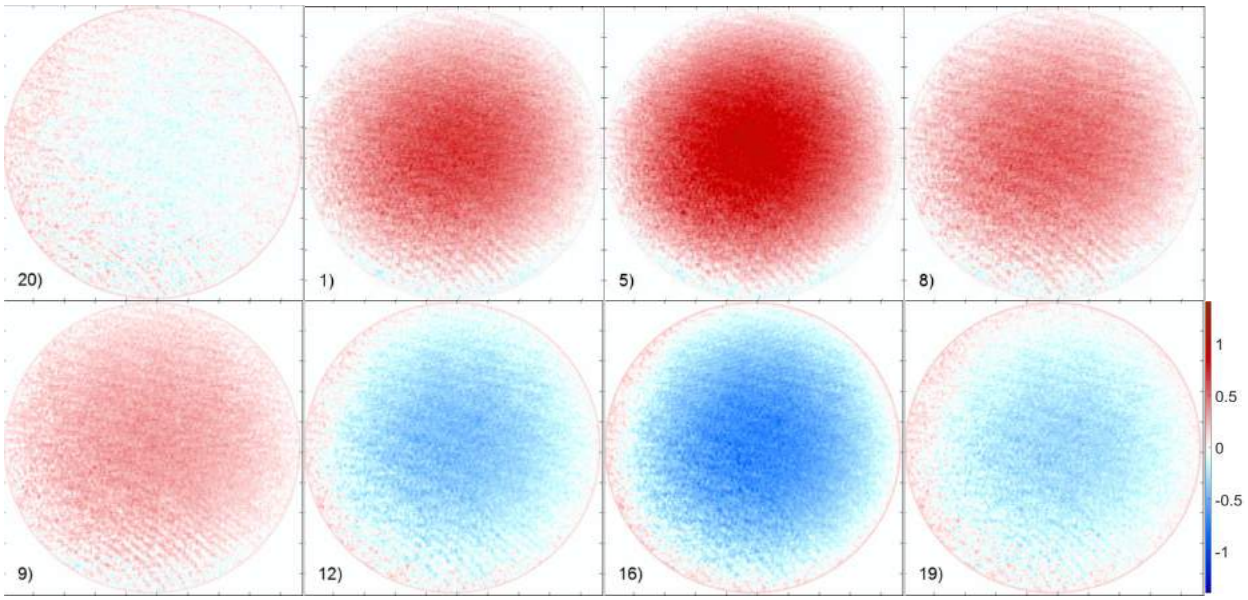


*Fig. 4.6 Results of FP, images taken at 229 Hz; time between consecutive snapshots is 0.55 ms.*

##### 4.2.1.1.1.2 Mode 11 at **492 Hz**, 17-cm diameter drum

At 492 Hz mode 11 is located. Fig. 4.7 shows the presence of one azimuthal node and one radial node. OOPCD are almost half of those in Fig. 4.6. Noise fringes are shown and apparently they are due to moiré effect between the projected grating and the matrix of pixels of the sensor.

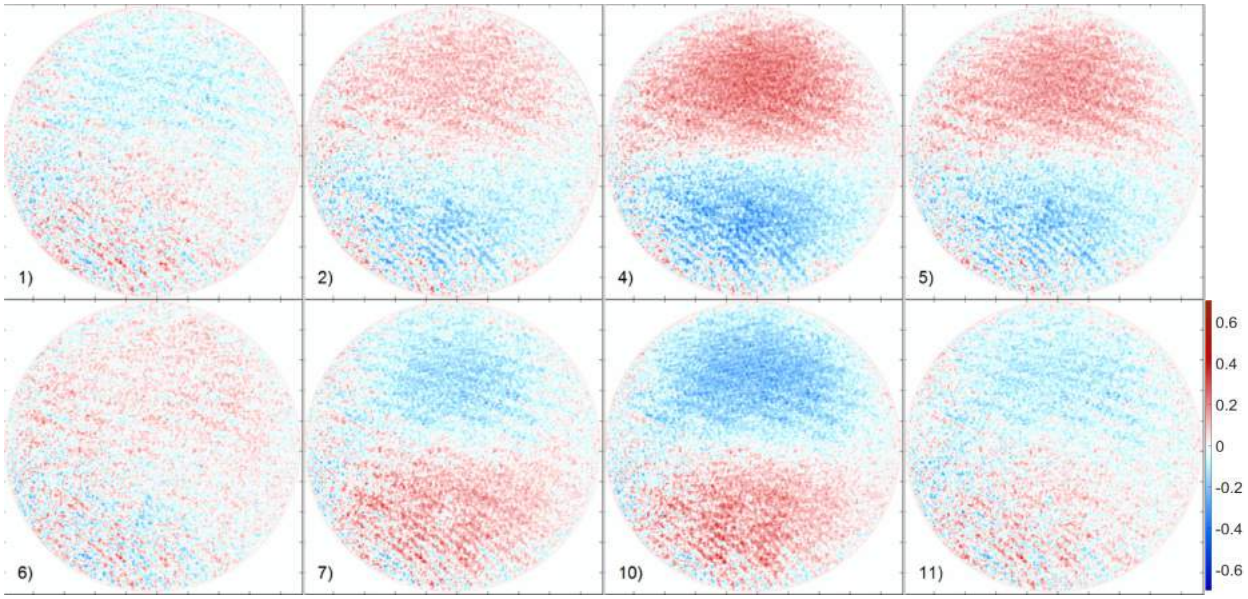


*Fig. 4.7 Results of FP, images taken at 492 Hz; time between consecutive snapshots is 0.25 ms.*

#### 4.2.1.1.1.3 Mode 21 at **659 Hz,** 17-cm diameter drum

Figure 4.8 shows mode 12, where it has one azimuthal node and two radial nodes; note that vertical lobes are not separated as the theory prescribes. OOCD are of almost the same magnitude than in Fig. 4.7.

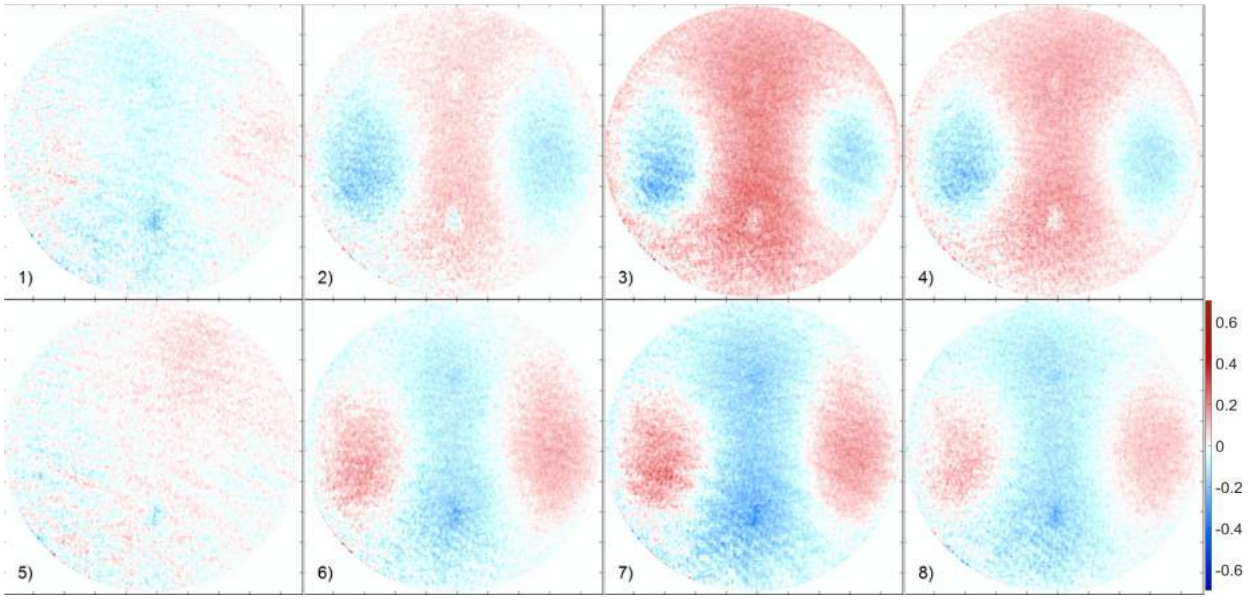


*Fig. 4.8 Results of FP, images taken at 659 Hz; time between consecutive snapshots is 0.19 ms.*

#### 4.2.1.1.1.4 Mode 02 at **742 Hz**, 17-cm diameter drum

Mode 02 is shown in Fig 4.9. The images show that the spatial distribution of this mode, overall, resembles the theoretical result. The displacements are in the limit of the setup resolution, and are close to noise level.

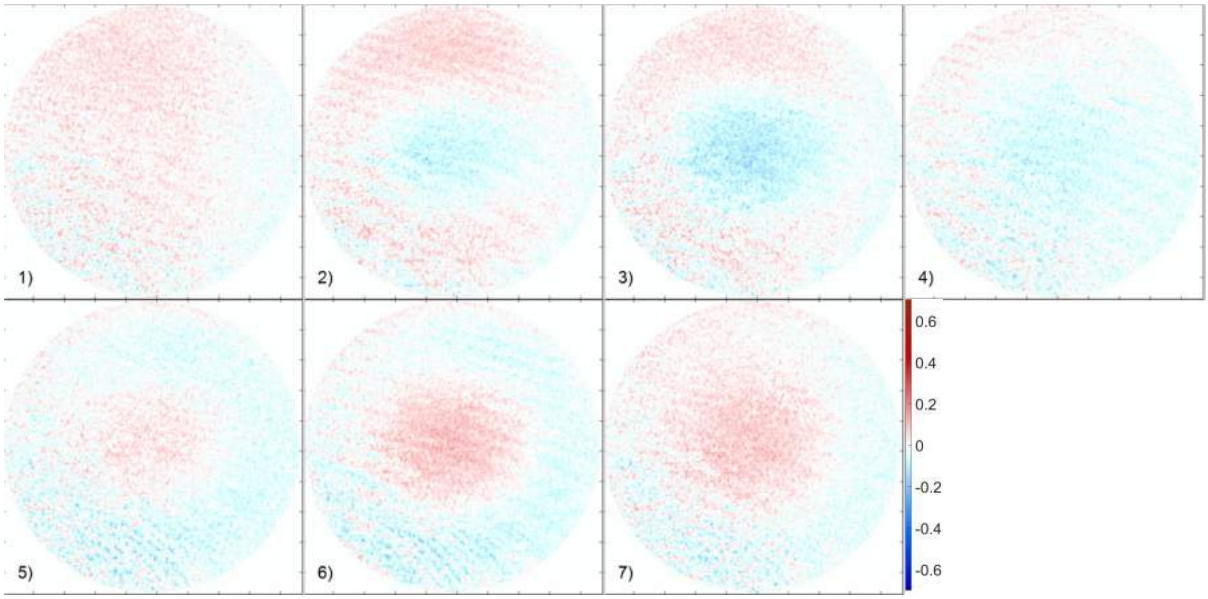


*Fig. 4.9 Results of FP, images taken at 742 Hz. Time between consecutive snapshots is 0.19 ms.*

In next section, the corresponding results for in-plane component of displacement (**IPCD**) are shown.

### *4.2.1.2 Separated DIC*

To implement DIC, we use proVISION with the parameters of Table 4.4; these parameters are used for all DIC calculations. We choose a 24x24-pix window correlation; the number of nodes is the quantity of points where the results are calculated; these results are obtained by interpolation.

| proVISION parameters | |
|---|---|
| Window correlation | 24x24 pix |
| Number of nodes | 40x40 nodes |

*Table 4.4 Used parameters in proVISION.*

An example of captured image is shown in Fig. 4.10 (a). When read in proVISION, a mesh of nodes is applied [Fig. 4.10 (b)], and the resulting vector map is obtained, Fig. 4.10 (c).

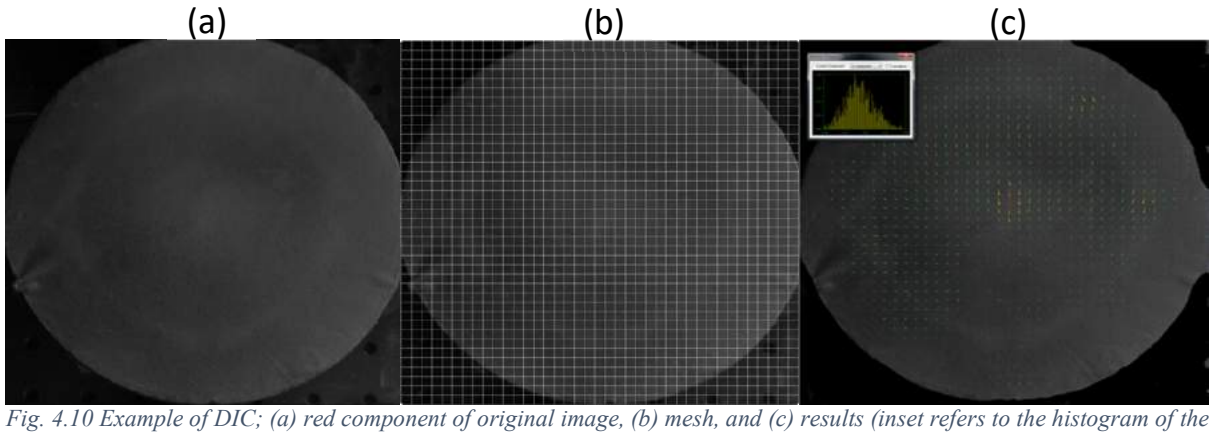


*Fig. 4.10 Example of DIC; (a) red component of original image, (b) mesh, and (c) results (inset refers to the histogram of the horizontal IPCD).*

### *4.2.1.3 Preliminary DIC test*

A comparison between results obtained by the in-house DIC algorithm (Section 3.2) and proVISION is included in parts (a) and (b) of Fig. 4.11, respectively, for a certain measurement. As proVISION yields better accuracy, all results related with DIC are computed by this package. The scale of the vectors is indicated by the horizontal vector located in the bottom right corner of each map, which in this case is 0.039 mm or equivalently 0.23 pix (value close to the limit of resolution).

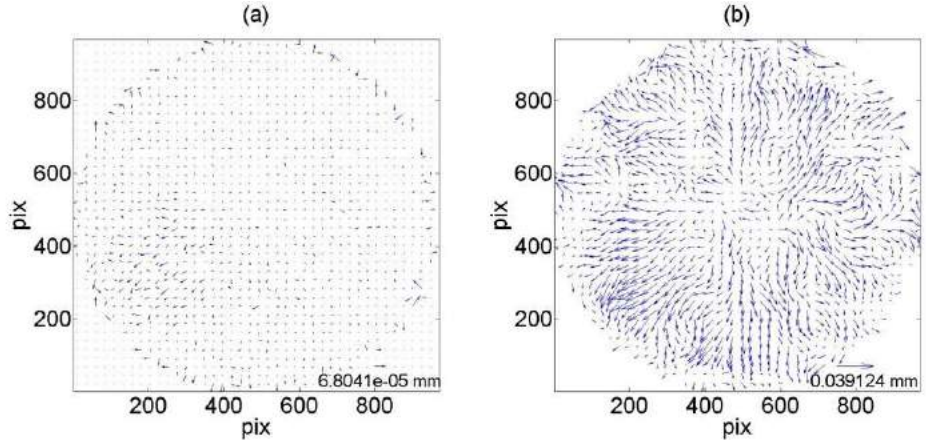


*Fig. 4.11 Results of DIC, using (a) an in-house algorithm, and (b) proVISION. IPCD of mode 01.*

#### 4.2.1.3.1 Results

Two vibration modes are measured by DIC alone. The resolution of DIC is related to that of proVISION, which has a resolution of 0.1 pix; in this case, this parameter is about 17 μm. In-plane displacements have a conversion factor of 0.17 mm/pix.

##### 4.2.1.2.1.1 Mode 01, **229 Hz**, 17-cm diameter drum

We captured in-plane images for a resonance frequency where out-of-plane modes are located (see previous section). Figure 4.12 illustrates the DIC results of mode 01. As it can be noticed, the magnitude of the IPCD is closely related with that obtained by FP. Additionally, vectors are directed inwardly when the OOPCD is directed away from the camera (red out-of-plane displacement). This suggests that the IPCD is in fact related to the cone of field of vision of the

imaging system as shown in the penultimate and last images. This type of displacement gives rise to errors when DIC alone is used and an OOPCD is incorporated in the measurement. From the geometry, the IPCD is $u(r) = rw(r)/H$, where $w(r)$ is the OOPCD at radial position $r$. This latter parameter can take values from 0 to $S/2$, with $S$ being the field of view, in mm [1]. The direction of $u(r)$ changes according to that of $w(r)$. In last part of Fig. 4.12, the displayed vector map assumes the OOPCD is constant throughout the field of view (only dependence on $r$ is assumed).

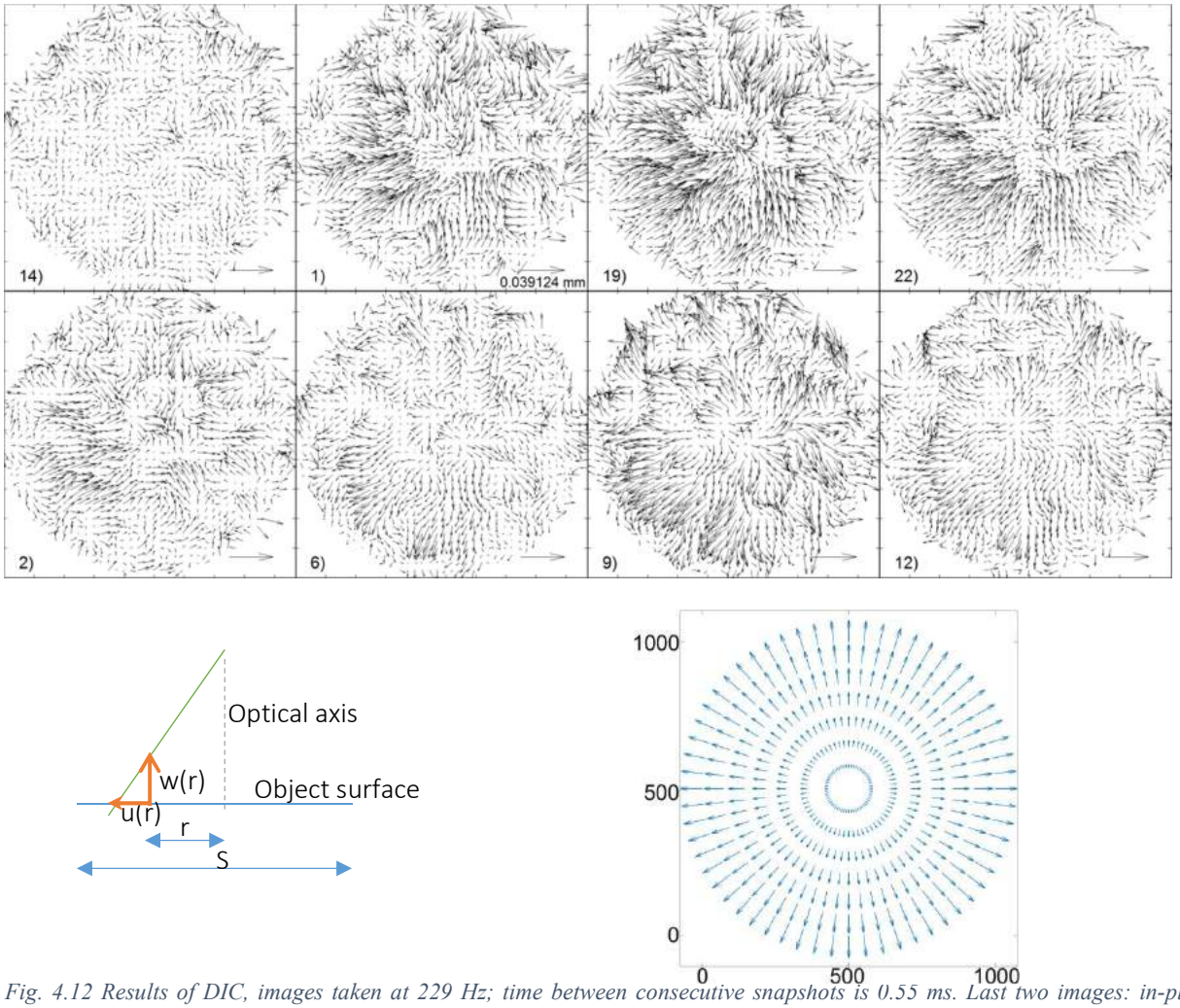


*Fig. 4.12 Results of DIC, images taken at 229 Hz; time between consecutive snapshots is 0.55 ms. Last two images: in-plane component arising from OOPCD, geometry and resulting vector map for uniform OOPCD (units are pix).*

#### 4.2.1.2.1.2 Mode 02, **492 Hz**, 17-cm diameter drum

In Fig. 4.13 we display the in-plane displacement map of mode 02; the maximum value is about the resolution of setup; therefore, the result is noisy and no spatial structure is well defined. The measurement of this mode is to be really improved when the FP-DIC (simultaneous measurements) is implemented, as shown in next section.

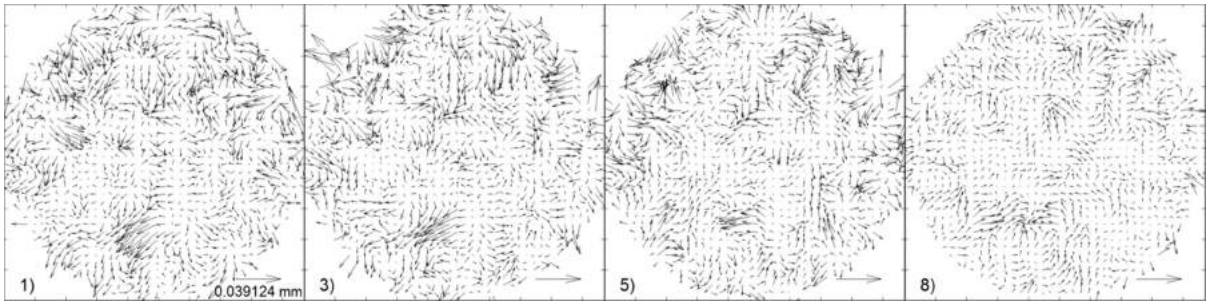


*Fig. 4.13 Vector fields at 492 Hz.*

IPCD of mode 21 and mode 02 are not shown, because in-plane displacements are beyond the resolution of the system.

#### *4.2.1.4 FP-DIC procedure*

By using color encoding, images are registered and separated by software; Fig. 4.14(a) shows a sample recorded image, and in (b) and (c) we include the images corresponding to the blue (FP, displayed in false color) and red (DIC) channels, respectively. Resulting three-dimensional fields are shown in next section.

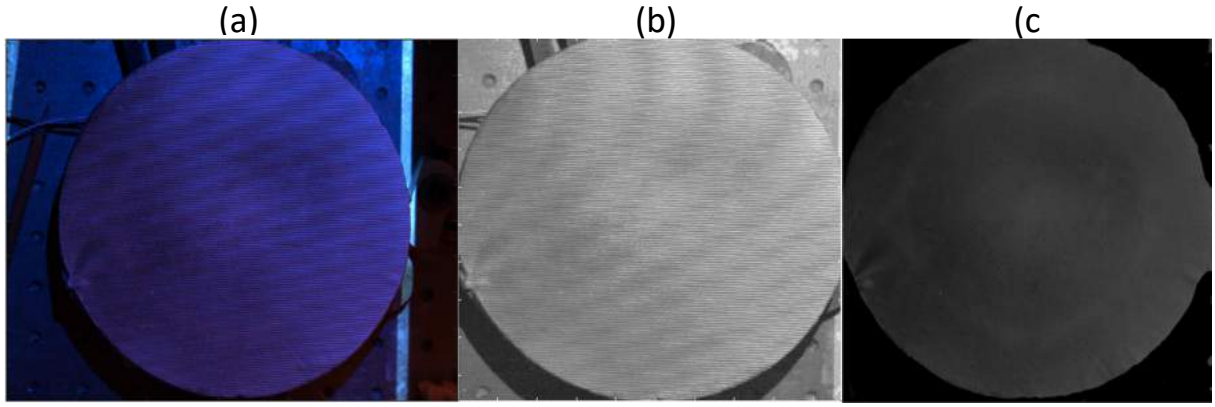


*Fig. 4.14 Example of FP-DIC; (a) original image, (b) FP image, and (c) DIC image.*

#### *4.2.1.5 Experimental FP-DIC*

The results to be presented correspond to the frequencies of out-of-plane modes. The object under analysis is the one used for the tests with techniques separated (Section 4.2.1).

##### 4.2.1.5.1 Results

The resolution of FP and DIC are 62 and 17 µm, respectively. In-plane displacements have a conversion coefficient of 0.17 mm/pix.

###### 4.2.1.5.1.1 Mode 01, **229 Hz**, 17-cm diameter drum

Figure 4.15 shows 3D-displacements maps for mode 01. IPCD follow the corresponding OOPCD according to the cone-of-vision effect, as described in Section 4.2.1.2.1.1. As observed, the center of the field of view is slightly downwards off-center. Besides, the quality of the maps for each technique is similar to that obtained when they are used separately.

Out-of-plane displacements in Fig. 4.15 are similar in magnitude to OOPCD in Fig. 4.6, but in-plane displacements of this section are twice than those in Fig. 4.12. This last observation arises from the fact that for the results, a different level of amplifier voltage is used.

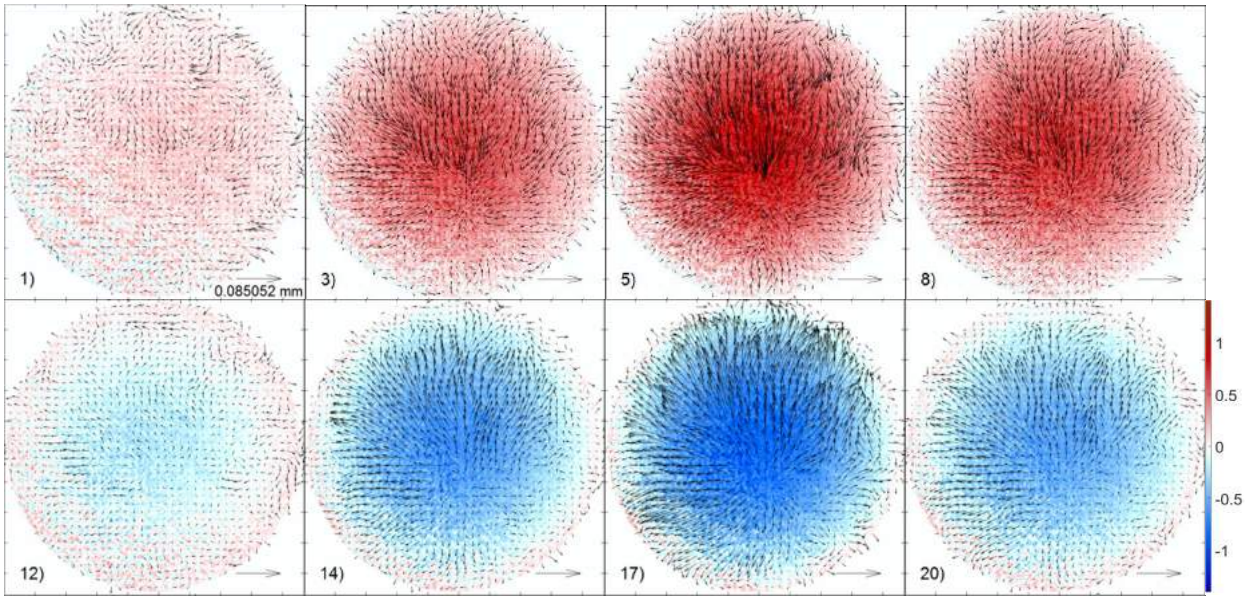


*Fig. 4.15 Results of FP-DIC, images taken at 229 Hz; time between consecutive snapshots is 0.55 ms.*

#### 4.2.1.5.1.2 Mode 11, **492 Hz**, 17-cm diameter drum

Figure 4.16 shows results for mode 11. OOPCD of this figure decreases in comparison with those in Fig. 4.15; in-plane displacements are close to the limit of resolution, and therefore the observed spatial structures are slightly misleading; for example, vectors in red zones should point inwards, but they do it almost randomly.

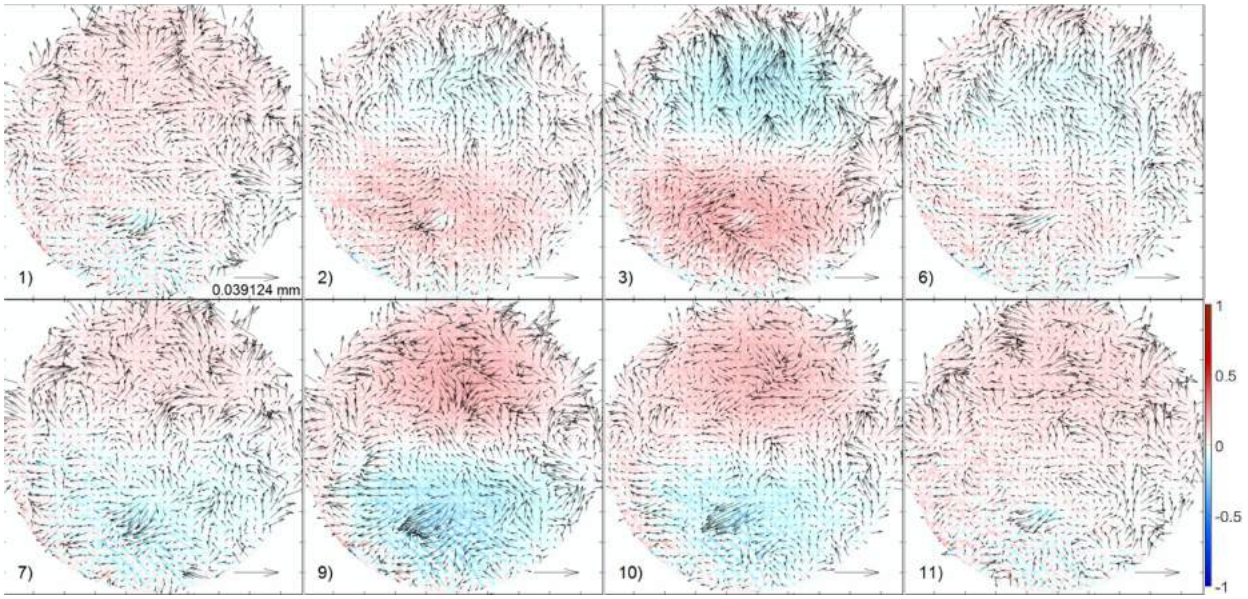


*Fig. 4.16 3D deformation at 492 Hz; time between consecutive snapshots is 0.25 ms.*

#### 4.2.1.5.1.3 Mode 21 **659 Hz**, 17-cm diameter drum

Figure 4.17 displays the results for mode 21. The dynamics of the OOPCD obtained in Sec. 4.2.1.1.1.3 is similarly obtained here. The IPCD follows the behavior shown in Fig. 4.16: in red and blue regions, the vector direction is inverted; further, where the magnitude of the OOPCD is close to the resolution limit, the computed IPCD is unreliable.

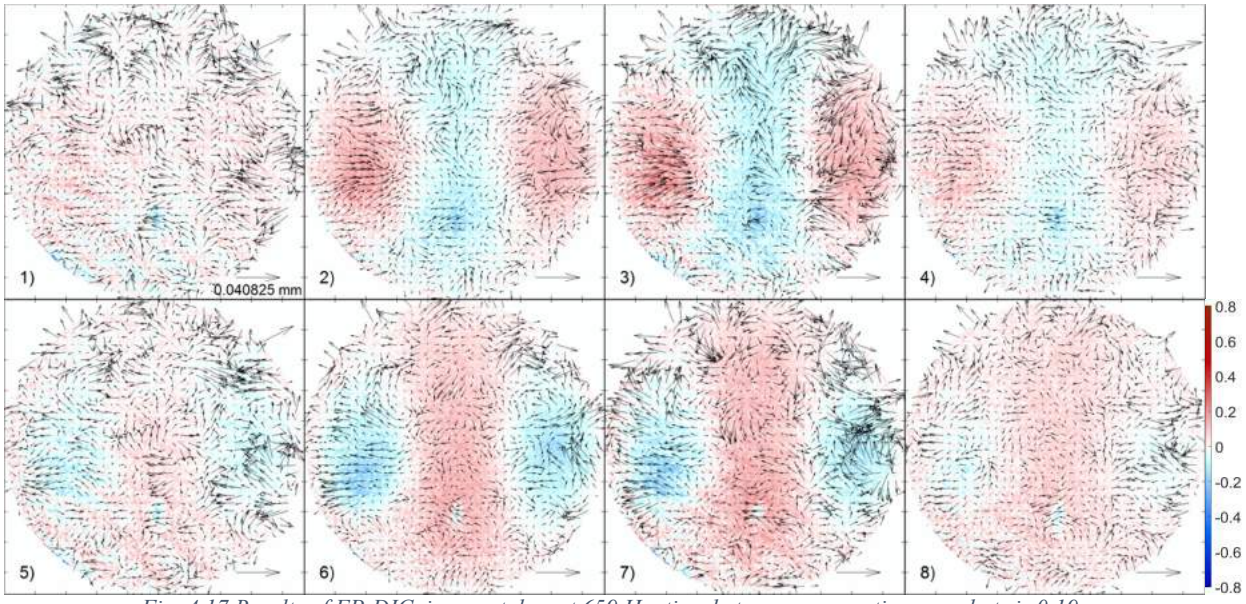


*Fig. 4.17 Results of FP-DIC, images taken at 659 Hz; time between consecutive snapshots is 0.19 ms.*

#### 4.2.1.5.1.4 Mode 02, **742 Hz**, 17-cm diameter drum

Results for mode 02 are shown in Fig. 4.18. As the magnitude of the OOPCD is relatively small, the IPCD becomes noisy and not valid. We need to remember that in red regions the IPCD should point inwards and in blue regions, outwards.

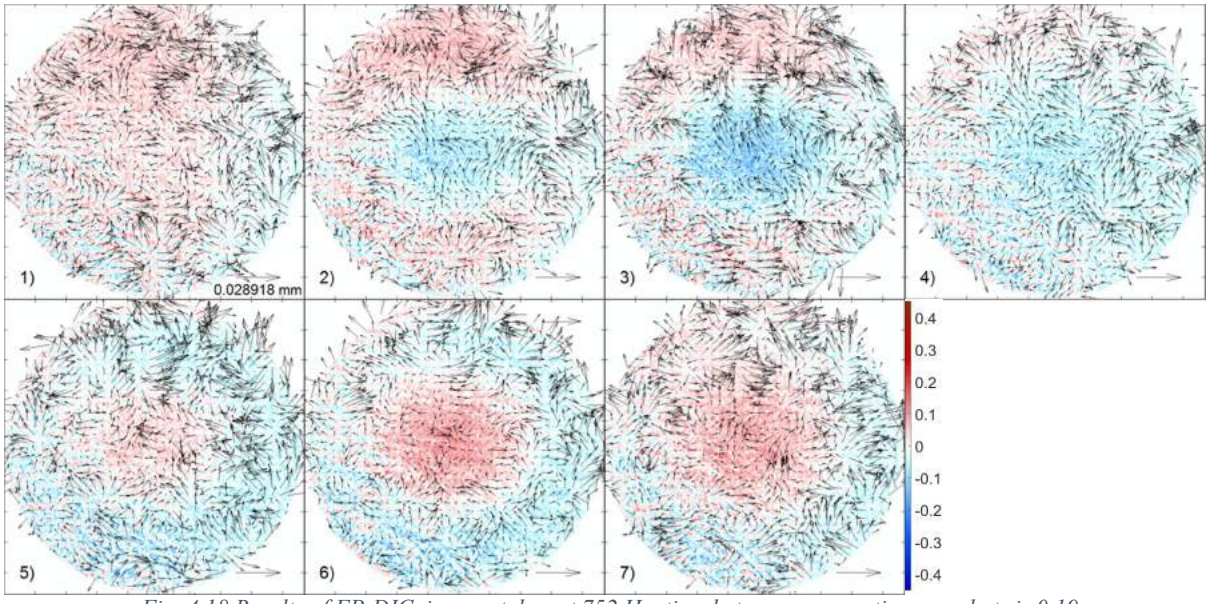


*Fig. 4.18 Results of FP-DIC, images taken at 752 Hz; time between consecutive snapshots is 0.19 ms.*

#### *4.2.1.6 Conclusions*

The experimental frequencies of modes depart from the theoretical values. This may be due to the non-uniformity of the loading and the uncertainty of the fixing along the drum boundary. Also, the non-uniformity and uncertainty of the Young modulus and Poisson ratio may contribute to the observed differences.

Measurements by FP-DIC demonstrate the proof-of-principle of the method. The IPDC comprises mainly the projection of the OOPCD, which arises from the cone of vision of the imaging lens.

Vibration modes are not located in a well-defined value of frequency, but within a frequency bandwidth. These values decrease with the order of vibration.

Drum (17-cm diameter) has a thin-plate behavior; its vibration mode frequencies follow approximately the proportions of Table 2.2.

The frequencies of vibration modes of the drum are unstable, the environment conditions affect the leather of the drum and this tends to change its properties.

### *4.2.2 LEATHER DRUM (25-CM DIAMETER) DRIVEN BY SPEAKER*

In this section, the object to be analyzed is a larger leather drum (Fig. 4.19) than in previous section; its properties are listed in Table 4.5; the properties are obtained using the real frequencies of vibration modes which are measured at the start of the tests. Table 4.6 shows setup parameters.

*Fig. 4.19 The drum is mounted on the setup.*

| Properties | Value | Units |
|---|---|---|
| Radius | 122.5 | mm |
| Thickness | 1.4732 | mm |
| Poisson ratio | 0.33 | - |
| Young modulus | 3.9354E+3 | Pa |
| Density | 638.5168 | $kg/m^3$ |

*Table 4.5 Properties of the leather drum.*

| $B$ (mm) | $H$ (mm) | $\theta$ (°) | $p$ (mm) |
|---|---|---|---|
| 190 | 625 | 16.9 | 1.48 |

*Table 4.6 Setup parameters.*

Table 4.7 shows the frequencies of the vibration modes; note that the frequencies decreases in comparison with those in Table 4.2 due to an increase in radius and thickness, according to Eq. 2.60 . As before, the theoretical values depart from the experimental ones. The reasons are the same as before.

| Mode | $f_{theorical}$ (Hz) | $f_{real}$ (Hz) |
|---|---|---|
| 01 | 117.0 | 117 |
| 11 | 240.5 | 241 |
| 21 | 363.2 | 361 |
| 02 | 456.1 | 410 |

*Table 4.7 Vibration modes frequencies.*

### *4.2.2.1 Results*

The resolution of FP is 74 µm and of DIC is 29 µm. The scale factor is 0.255 mm/pix.

#### 4.2.2.1.1 Mode 01, **117 Hz**, 25-cm diameter drum

The presence of mode 01 dominates the OOPCD; IPCD follow the OOPCD in the way of projections, and they therefore have a radial distribution; Fig. 4.20 shows the displacements. Magnitudes of OOPCD and IPDC are larger than those in Fig. 4.15, while maintaining the same driving voltage.

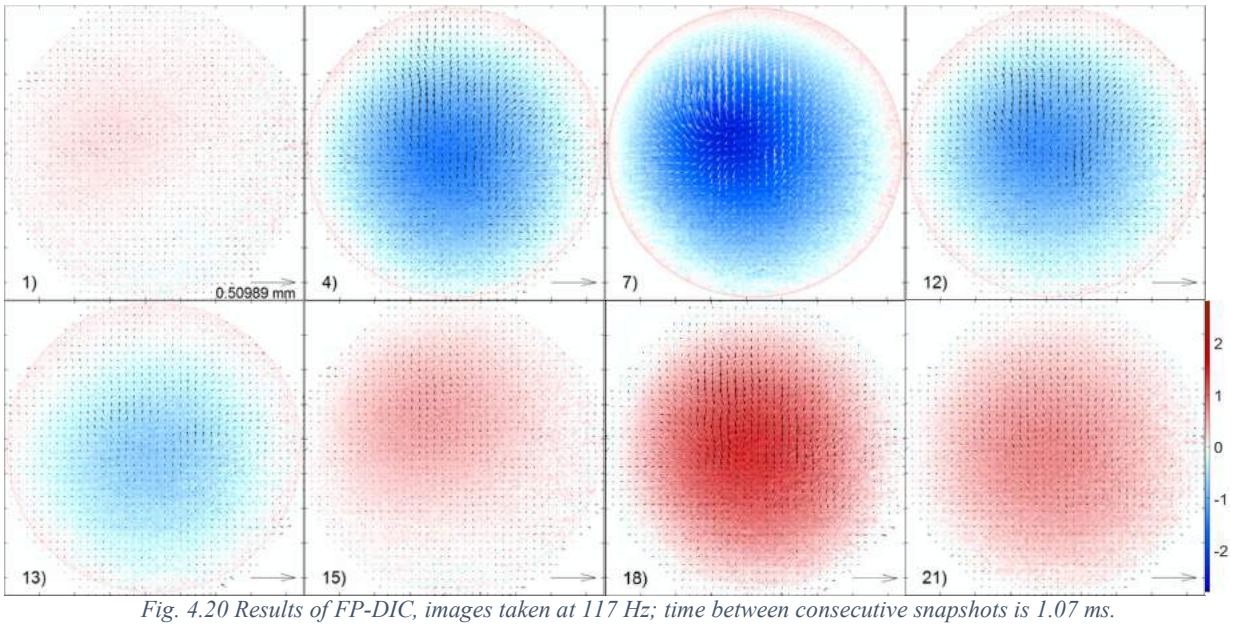


*Fig. 4.20 Results of FP-DIC, images taken at 117 Hz; time between consecutive snapshots is 1.07 ms.*

#### 4.2.2.1.2 **241 Hz**, 25-cm diameter drum

Mode 11 is presented; both OOPCD and IPCD are close to their respective resolution limits and no valid results for IPDC can be estimated, as illustrated in Fig. 4.21. The mode is not clearly shown because it is not a pure one, but a mixture of neighbor modes; however, mode 11 predominates.

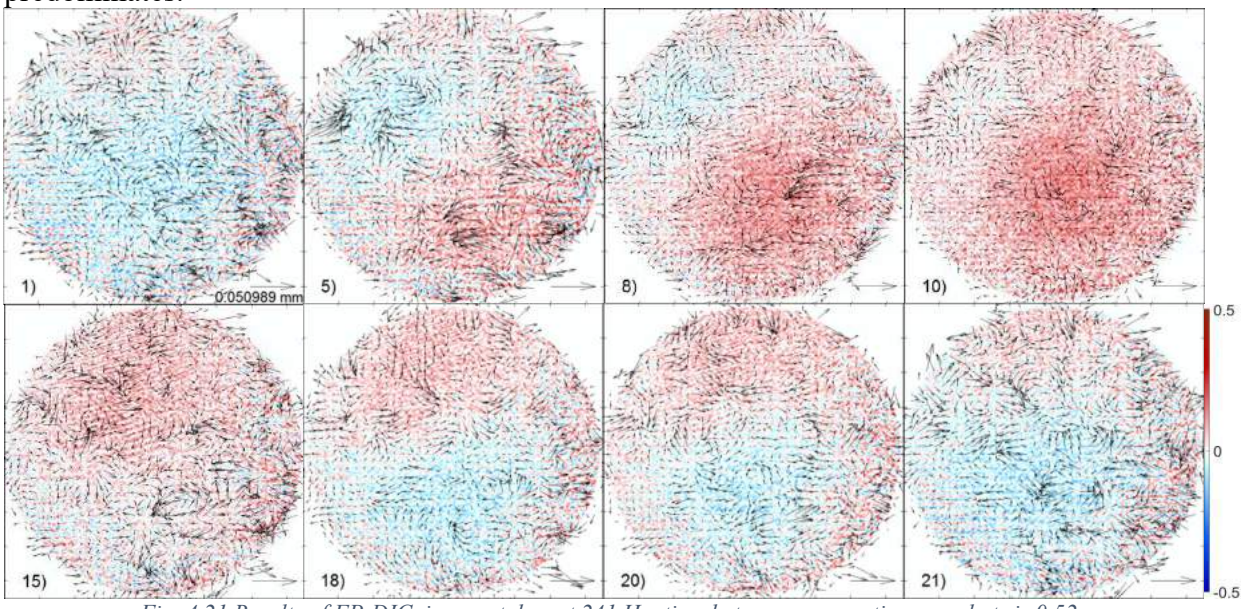


*Fig. 4.21 Results of FP-DIC, images taken at 241 Hz; time between consecutive snapshots is 0.52 ms.*

#### 4.2.2.1.3 Mode 21, **361 Hz**, 25-cm diameter drum

Mode 21 is shown in Fig. 4.22. It consists in fact, as in the last case, of a mixture of modes. This is the reason, the OOPCD increases regarding mode 11. The presence of mode 02 is noticed, for example in panels 1 and 15.

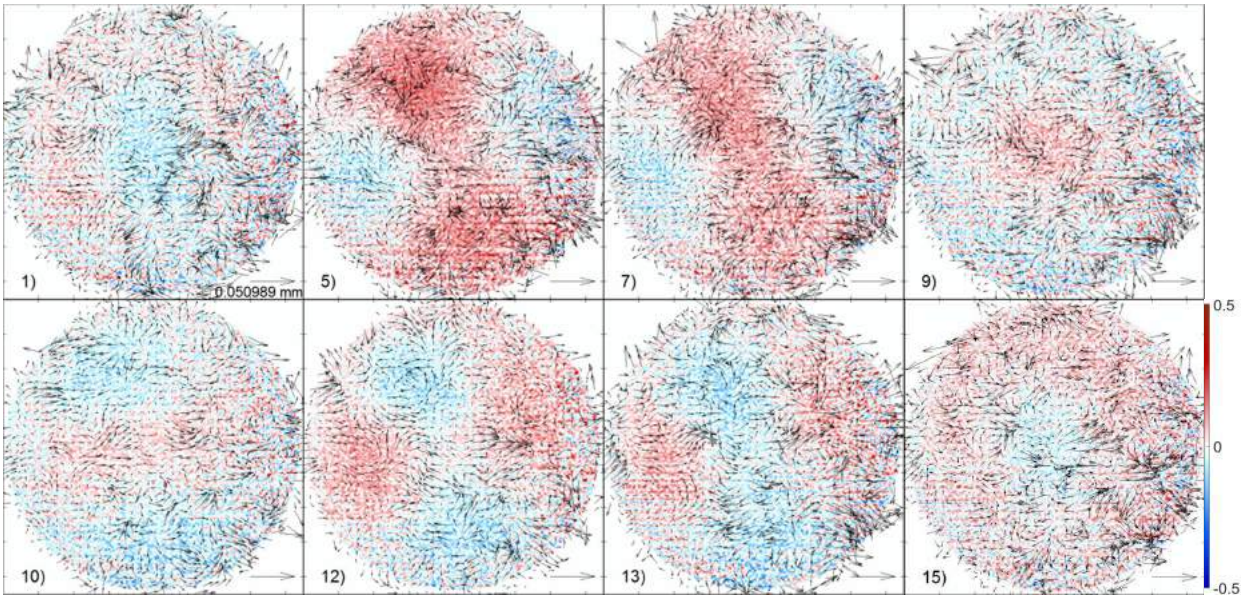


*Fig. 4.22 3D displacement at 361 Hz; time between consecutive snapshots is 0.35 ms.*

#### 4.2.2.1.4 Mode 02, **410 Hz**, 25-cm diameter drum

Composition of mode 02 is more pure than previous modes, as presented in Fig. 4.23.

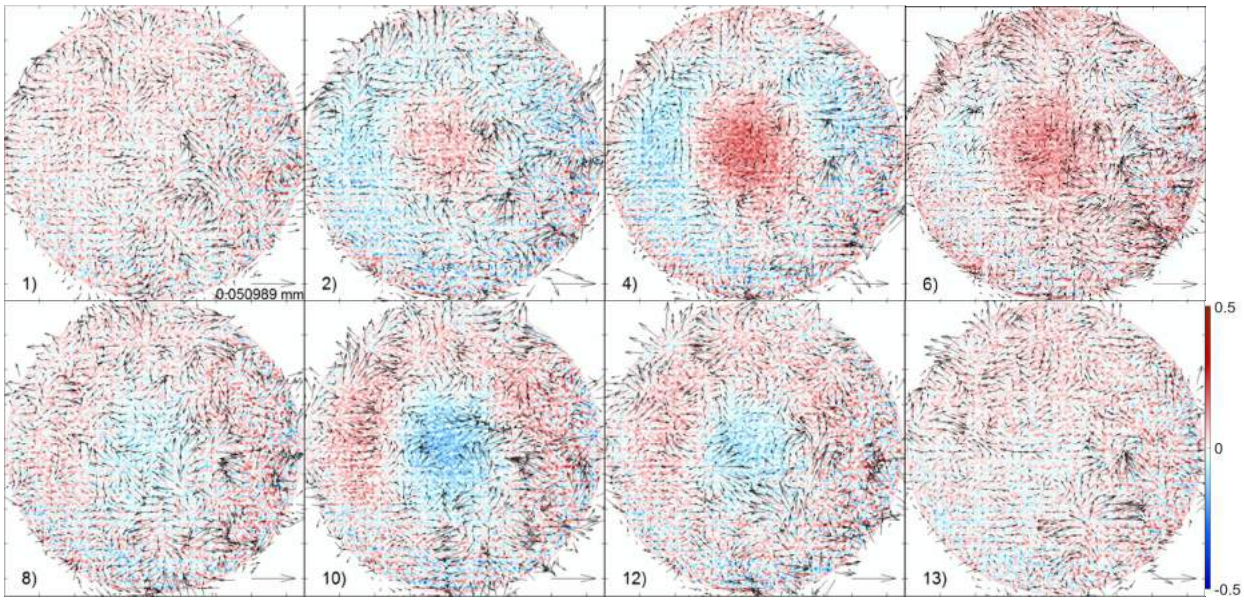


*Fig. 4.23 3D displacement at 410 Hz; time between consecutive snapshots is 0.31 ms.*

### *4.2.2.2 Conclusions*

The 25-cm diameter drum has a thin plate behavior as well; its vibration mode frequencies are more stable than those of the 17-cm diameter drum; this is due to its better manufacturing. As diameter and thickness of this drum are larger than those of the 17-cm diameter drum, frequencies of vibration increase according to Eq. 2.60. Besides, the spatial form of the higher modes is not clearly defined as before.

Results when this drum is subjected to point loading is presented next.

## *4.2.3 LEATHER DRUM (25-CM DIAMETER) DRIVEN BY SHAKER*

We analyze the differences when applying point loading to the drum of last section; loading is applied by a shaker, which is fixed to the center of drum. We use a combination of screw and nut to fix the shaker to the leather by using glue (Resistol 500).

Some of the real frequencies in Table 4.9 are slightly different than those in Table 4.7; but in general they resemble one another.

| Mode | $f_{theoretical}$ (Hz) | $f_{real}$ (Hz) |
|---|---|---|
| 01 | 117.0 | 117 |
| 11 | 240.5 | 221 |
| 21 | 363.3 | 355 |
| 02 | 456.1 | 410 |

*Table 4.9 Vibration modes frequencies.*

### *4.2.3.1 Results*

Resolution hold at 74 µm and 29 µm for FP and DIC, and the conversion factor is 0.261 mm/pix. The fundamental mode and mode 02 do not change their frequency values in comparison with Table 4.7; while mode 11 decreases 8.3% and mode 21 decreases 1.66%.

#### 4.2.3.1.1 Mode 01, **117 Hz**, 25-cm diameter drum

Results are shown in Fig. 4.24. The OOPCD shows a departing structure from the ideal case when its value is relatively small. On the other hand, the IPCD shows a distribution that overrides the OOPCD projection; this IPCD does not depend on the magnitude or direction of the OOPCD. This may be due to the loading condition, but it should be expected to be constant, as representing rigid-body displacement.

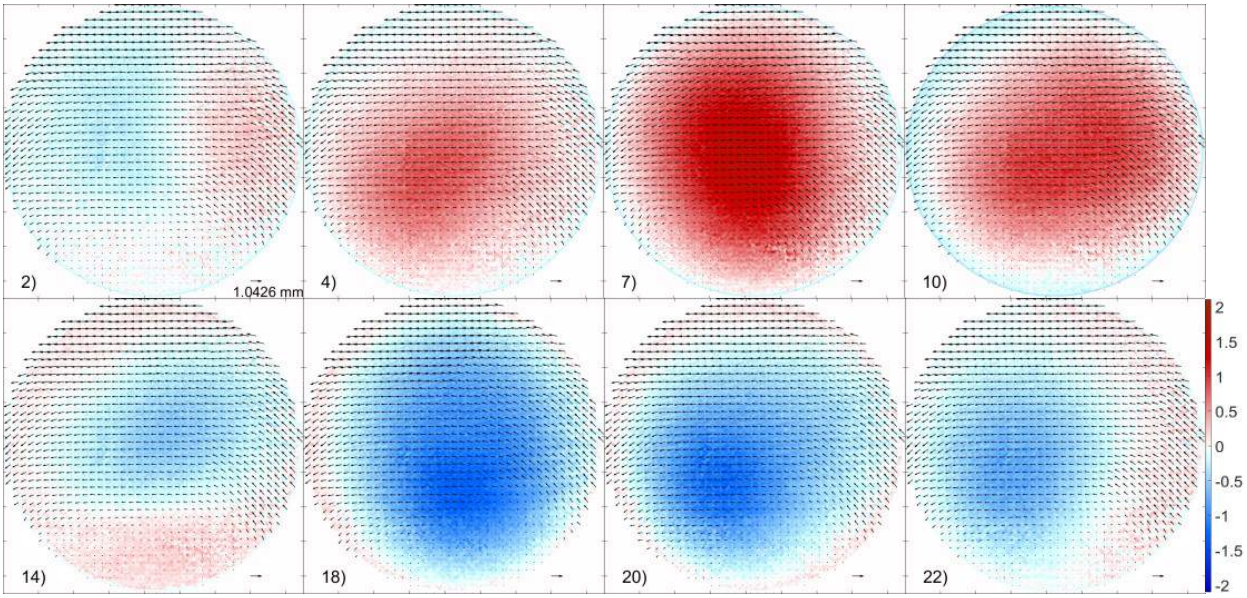


*Fig. 4.24 Results of FP-DIC, vibration at 117 Hz; time between consecutive snapshots is 1.07 ms.*

#### 4.2.3.1.2 Mode 02, **221 Hz**, 25-cm diameter drum

Figure 4.25 shows that in this case, the displacement for mode 11 does contain less noise and is purer than when driven by the speaker. A non-expected circumferential IPCD is reported and it overrides the projected OOPCD. The origin of this distribution is unknown. We can observe that the direction of the IPCD maintains unchanged.

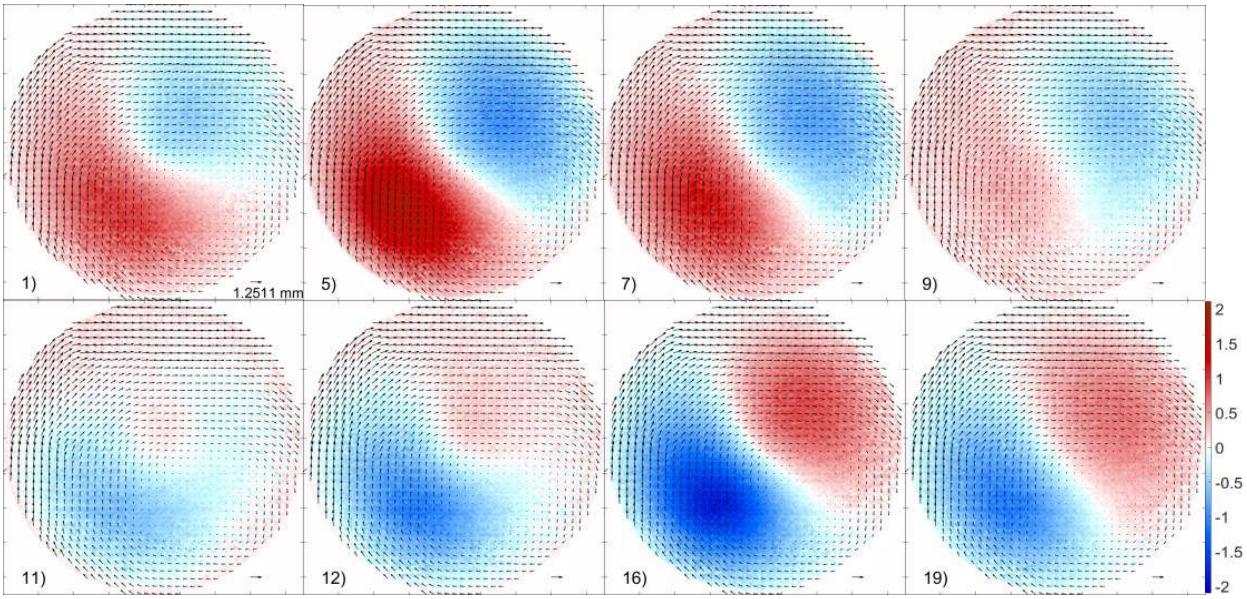


*Fig. 4.25 Results at 221 Hz; time between consecutive snapshots is 0.57 ms.*

#### 4.2.3.1.3 Mode 21, **355 Hz**, 25-cm diameter drum

For Mode 21, Figure 4.26, the structure of a pair of lobes prevails, especially when the OOPCD is relatively large. For small OOPCD, presence of mode 02 is observed.

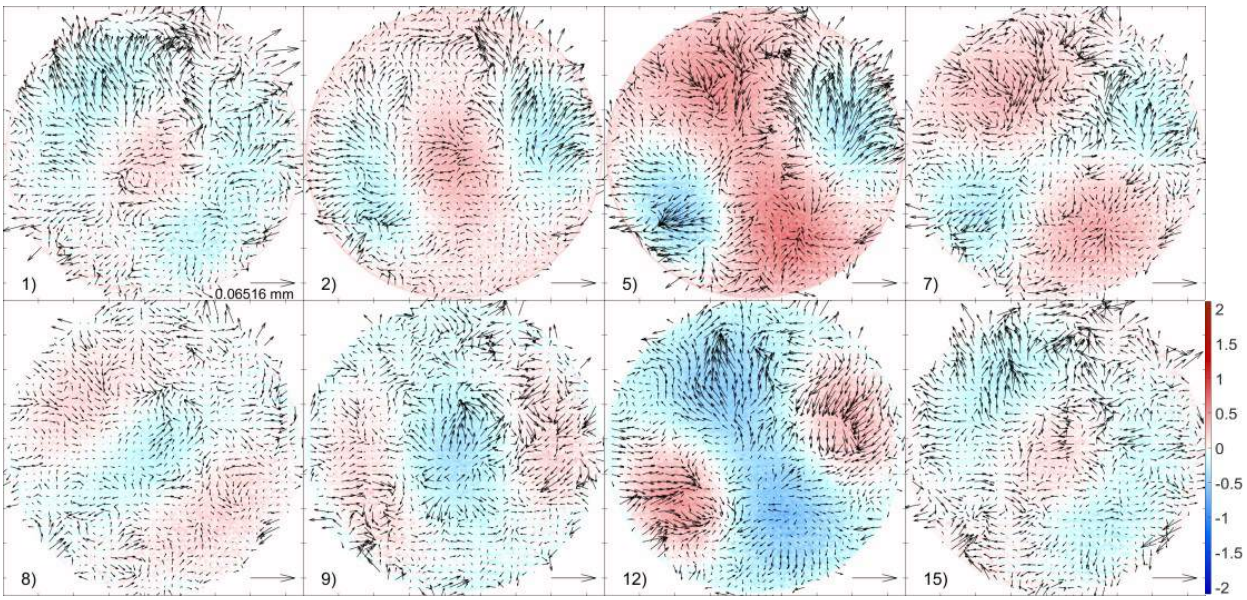


*Fig. 4.26 3D displacement at 355 Hz; time between consecutive snapshots is 0.35 ms.*

#### 4.2.3.1.4 Mode 02, **410 Hz**, 25-cm diameter drum

In Fig. 4.27 the 3D displacement maps related to mode 02 is reported. This mode is the weakest one. The IPCD tends to follow the expected directions that the OOPCD projections dictate, but their magnitudes are not reliable.

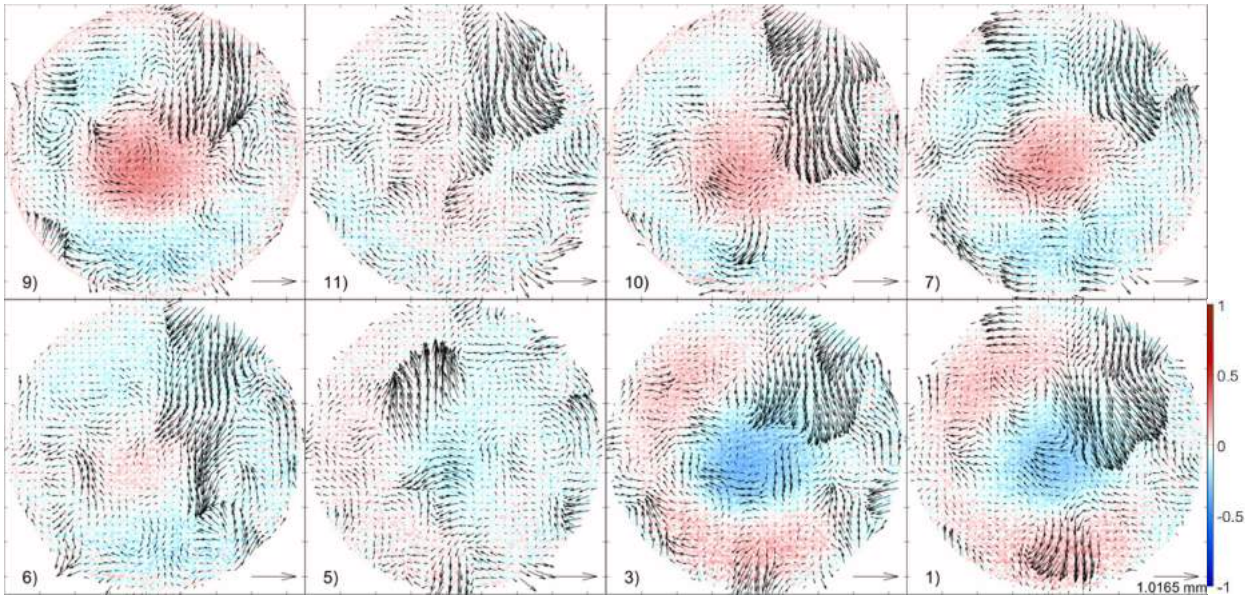


*Fig. 4.27 Results of FP-DIC, images taken at 410 Hz; time between consecutive snapshots is 0.30 ms.*

### *4.2.3.2 Conclusions*

The type of force excitation affects the IPCD content of the vibration mode displacement. IPCD of Fig. 4.24 and Fig. 4.25 have a circumferential distribution; we have not information to determine the origin of this movement.

## 4.3 ALUMINUM PLATE

In this section, two aluminum plates with different thickness are analyzed (diameter of 29.5 cm), Fig 4.28; their properties are shown in Table 4.10. We present results, for each plate, for two different loadings, by a speaker (uniform loading) and by a shaker (single-point loading).

*Fig. 4.28 The aluminum plate mounts on the setup.*

| Properties | Value | Units |
|---|---|---|
| Radius | 147.5 | mm |
| Poisson ratio | 0.33 | - |
| Young modulus | 6.96E+10 | Pa |
| Density | 2770 | $kg/m^3$ |

*Table 4.10 Properties of aluminum plate.*

### *4.3.1 ALUMINUM PLATE (0.1-MM THICKNESS) DRIVEN BY SPEAKER AND SHAKER*

The setup parameters for this object are listed in Table 4.11. Row 1 refers to parameters for loading by the speaker and row 2, for loading by the shaker.

| $B$ (mm) | $H$ (mm) | $\theta$ (°) | $p$ (mm) |
|---|---|---|---|
| 150 | 715 | 11.8 | 1.705 |
| 175 | 720 | 13.7 | 1.161 |

*Table 4.11 Setup parameters.*

The vibration mode frequencies are reported in Table 4.12. In this case no real frequencies of resonance are found. By the properties and parameters of the object, we computed the theoretical values. The numerical values are computed similarly, but in this case ANSYS is used. The values of frequencies are too close between them; therefore, the vibration modes are expected to present mixed modes.

| Mode | $f_{theoretical}$ (Hz) | $f_{numerical}$ (Hz) | $f_{real}$ (Hz) |
|---|---|---|---|
| 01 | 11.4 | 11.5 | - |
| 11 | 23.5 | 24.0 | - |
| 21 | 35.5 | 39.4 | - |
| 02 | 44.6 | 45.0 | - |
| 31 | 45.9 | 57.7 | - |

*Table 4.12 Vibration mode frequencies.*

#### *4.3.1.1 Results*

For this setup, for speaker loading, the FP and DIC resolutions are 85 µm and 30 µm, respectively, and for point loading, they are 58 and 30 µm. Since no pure modes are found, we proceed to make a frequency scan every 10 Hz. The conversion factor is 0.295 mm/pix.

The results of FP-DIC at 40 Hz are shown on bottom row of Fig. 4.29; no pure vibration mode is recognized. On bottom row of images, we include the results for point loading. In general, for frequency values smaller than 15 Hz and greater than 70 Hz no well-defined OOPCD is observed. The reported results for point loading correspond to 55 Hz. In this case, OOPCD starts to be significant at about 30 Hz instead of 15 Hz. Further, the point of contact of the shaker

stands out in the maps, and is at the center of the images. Mode shapes from both types of loadings do not resemble each other.

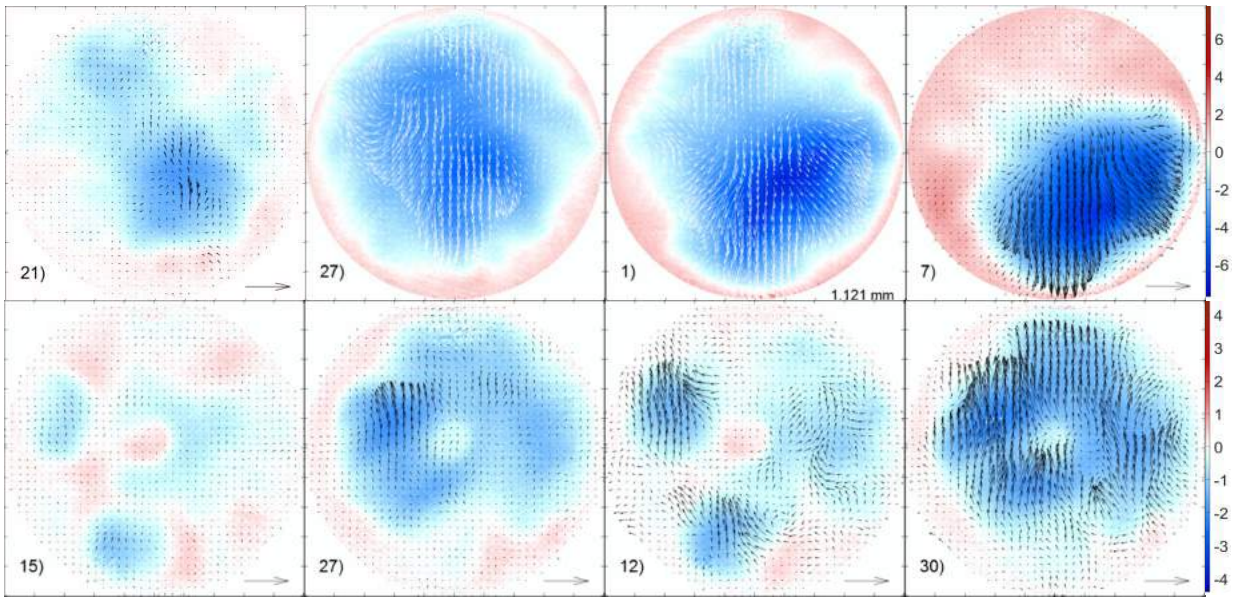


*Fig. 4.29 Speaker loading, at 40 Hz (upper row); shaker loading, at 55 Hz (bottom row).*

### *4.3.1.2 Conclusions*

The vibration modes are mixed and are not pure. This mostly is because of the thickness of the plate, where modes become too close to each other in frequency. By inspection of the whole set of images corresponding to a vibration cycle, we notice that the deformation changes smoothly in time (in live observation, it seems the plate is so rigid that the motion switches extremely fast, producing a continuous loud noise).

In next section, we present the results when the thickness of the plate is increased.

## *4.3.3 Aluminum plate (0.71-mm Thickness) driven by speaker and shaker*

Increasing the thickness of the aluminum plate let us separate the vibration mode frequencies. This study case is numerically simulated. Table 4.15 includes setup parameters.

| $B$ (mm) | $H$ (mm) | $\theta$ (°) | $p$ (mm) |
|---|---|---|---|
| 180 | 720 | 14.0 | 1.178 |

*Table 4.15 Setup parameters.*

The obtained vibration mode frequencies are shown in Table 4.16; experimentally, mode 11 appears first than mode 21 and mode 31 appears first than mode 02. This implies the presence of strong mixing of modes.

| Mode | $f_{theoretical}$ (Hz) | $f_{numerical}$ (Hz) | $f_{real}$ (Hz) |
|---|---|---|---|
| 01 | 80.1 | 81.8 | 78 |
| 11 | 164.6 | 170.1 | 280 |
| 21 | 248.6 | 279.1 | 219 |
| 02 | 312.2 | 318.2 | 354 |
| 31 | 321.1 | 408.3 | 340 |

*Table 4.16 Vibration modes frequencies.*

### *4.3.2.1 Results*

In the section, we have a resolution of FP is 59 µm and a resolution of DIC is 30 µm. The conversion factor is 0.295 mm/pix. In the following results for each resonance frequency and each figure, the first two rows of images correspond to results with speaker and the two other rows, to shaker.

#### 4.3.2.1.1 Mode 01, **78 Hz**, 0.71-mm thickness aluminum plate

For mode 01, results are given in Fig. 4.30; the magnitude of both OOP and IPCD are larger than those observed for the leather drum.

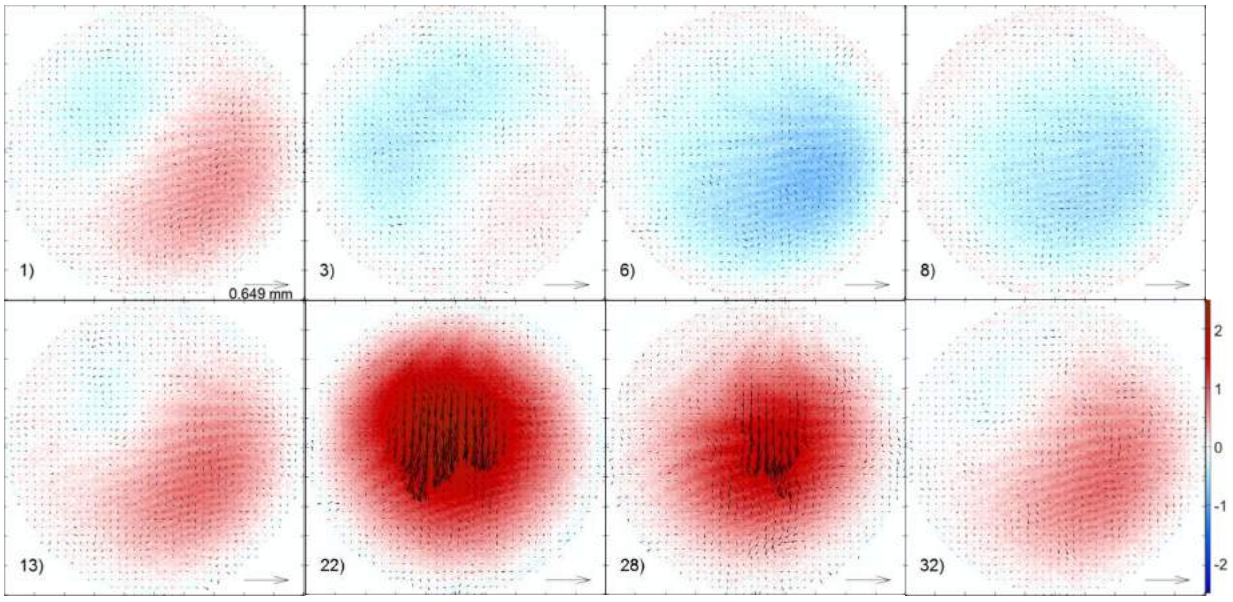

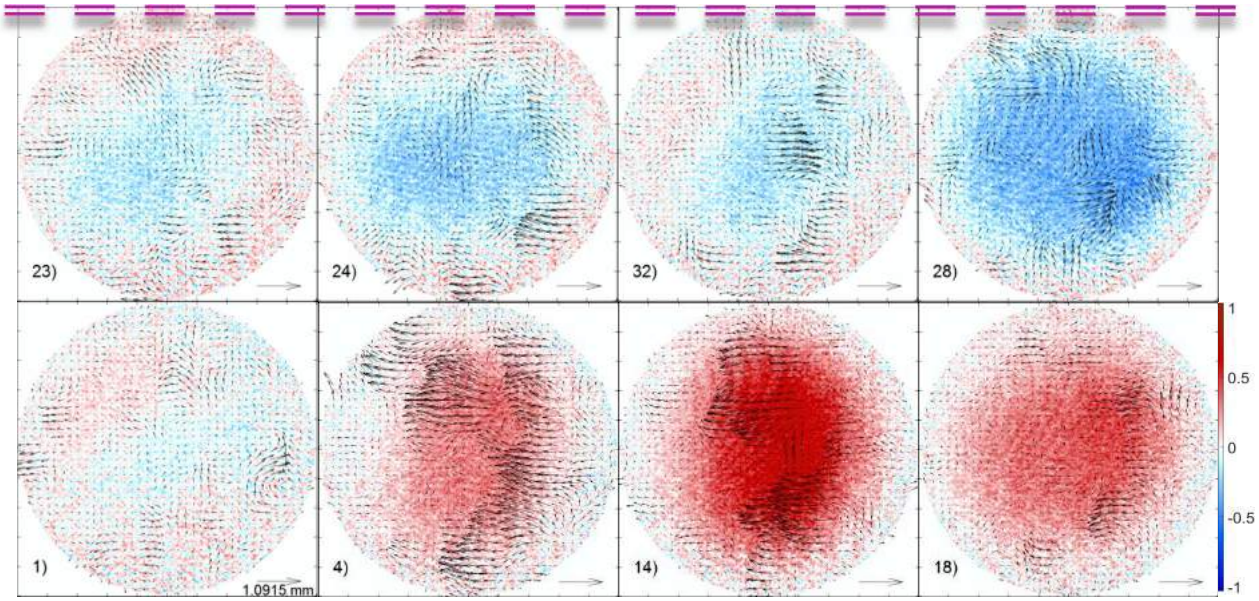


*Fig. 4.30 Mode 01 at 78 Hz; time between consecutive snapshots is 1.6 ms.*

We can observe that the content of noise of the results with shaker es larger than those with speaker; the cause of this effect is the application of a gain boost to the blue channel in the first case. The magnitud of the OOPCD is fairly the same for both cases; however, the IPCD is almost twice in the shaker case, and its nature stems mainly from OOPCD projections. For the speaker loading, panels 1, 3, 13, and 32 reveal the presence of mode 11.

#### 4.3.2.1.2 Mode 21, **219 Hz**, 0.71-mm thickness aluminum plate

In Fig. 4.31 mode 21 displacement maps are shown. Theoretically, mode 11 should be first than mode 21, but it turns out to be reversed in both types of loading; this may be due to the existence of strong coupling of modes. Also, as it is observed, the magnitude of OOPCD is smaller for the speaker loading. What appears to be similar, it is the appearance of a strong component of in-plane displacement, but reversed when they are compared.

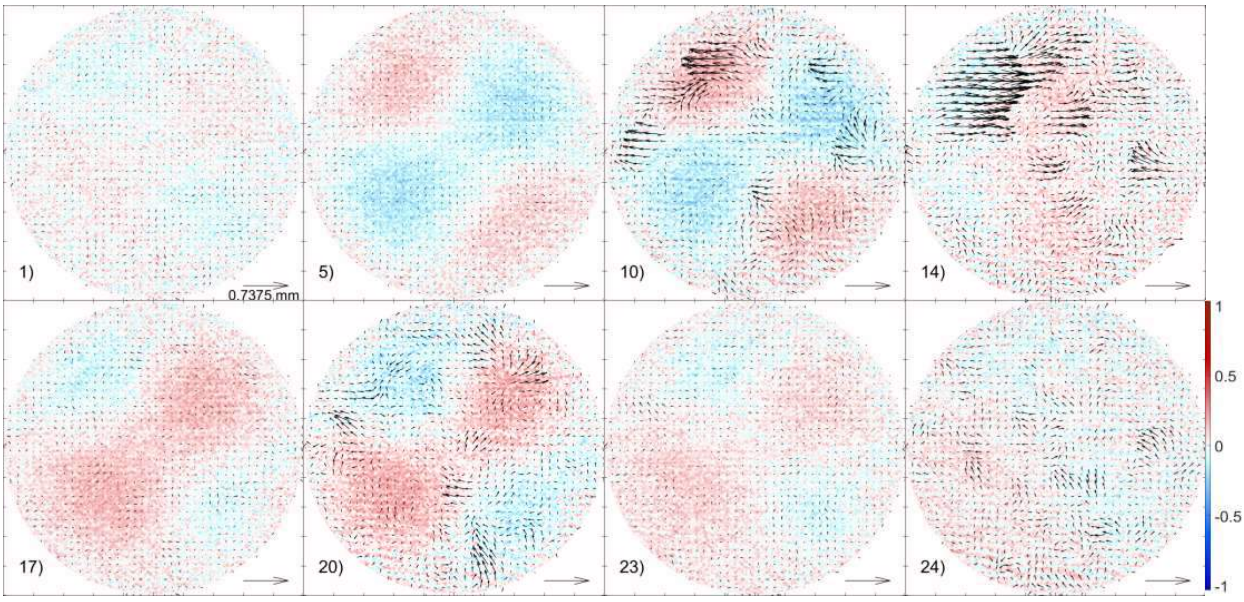

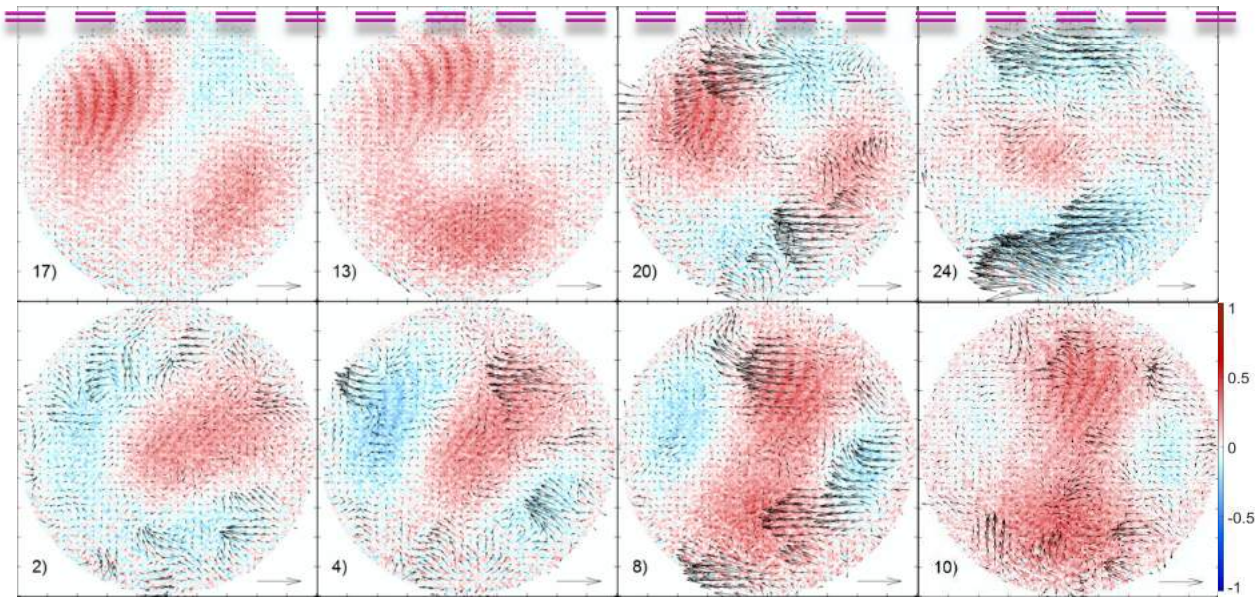


*Fig. 4.31 Mode 11, 219 Hz; time between consecutive snapshots is 0.57 ms.*

#### 4.3.2.1.3 Mode 11, **280 Hz**, 0.71-mm thickness aluminum plate

As mentioned in the preceding section, mode 11 appears after mode 21, something unexpected from theory. Figure 4.32 shows three-dimensional maps of displacement for time snapshots, for both types of loading. Also, position of the OOPCD lobes is not the same. Mode 02 contribution is mostly revealed when the OOPCD is relatively small (see panels 1, 17 and 9).

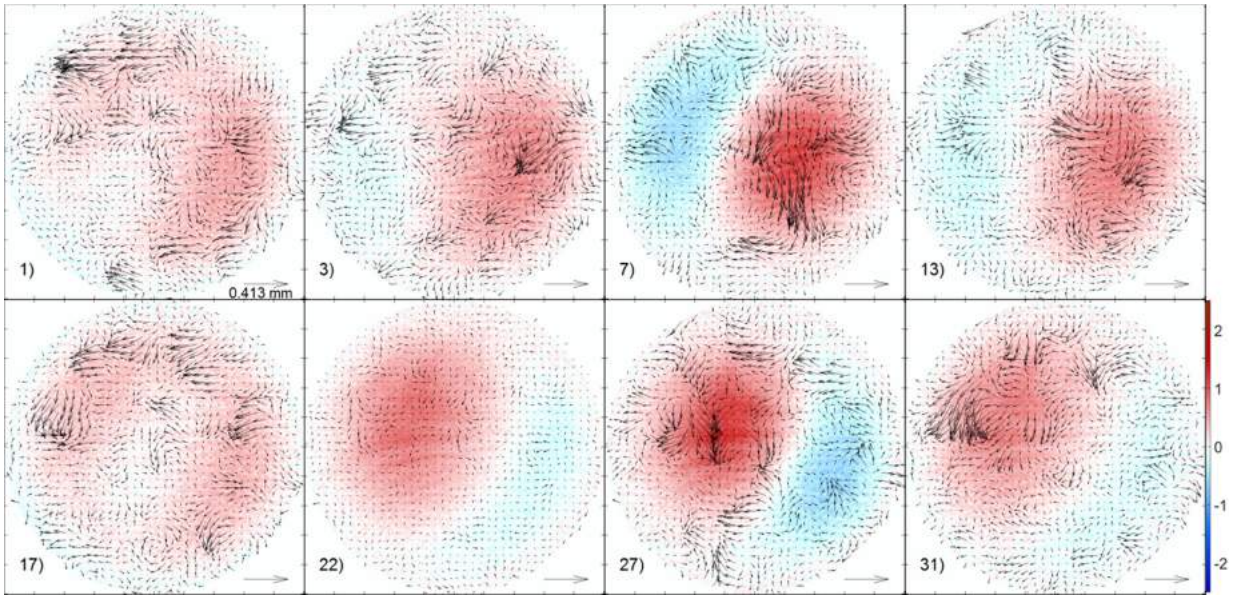

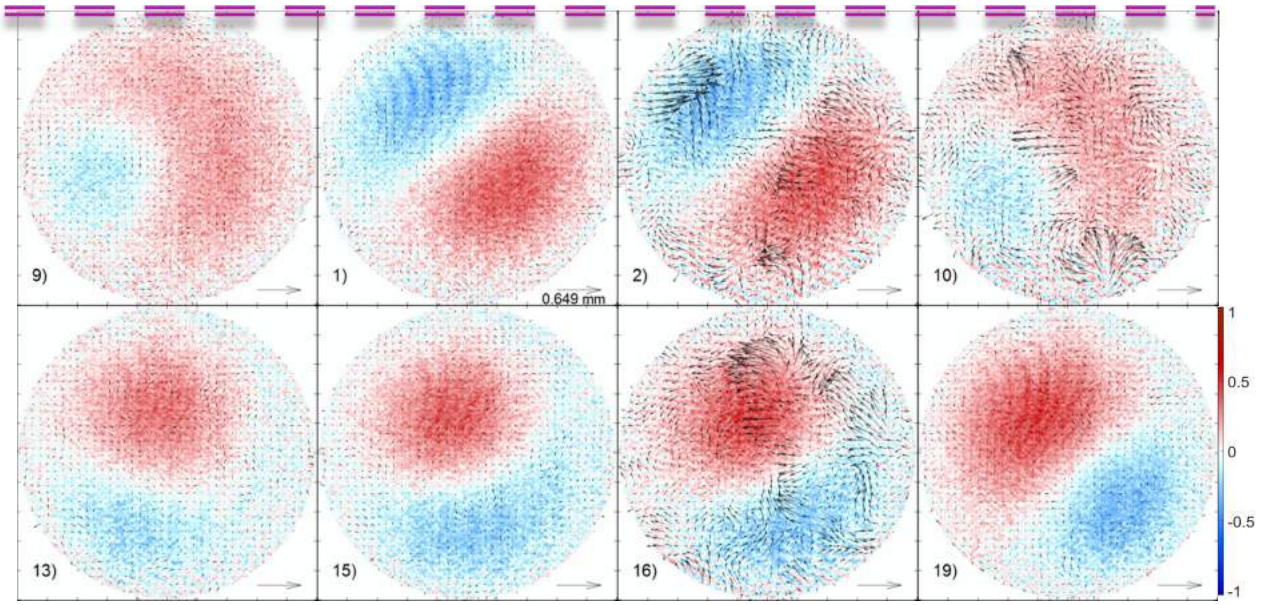


*Fig. 4.32 Mode 11 at 280 Hz; time between consecutive snapshots is 0.45 ms.*

#### 4.3.2.1.4 Mode 31, **340 Hz**, 0.71-mm thickness aluminum plate

Mode 31 should be after mode 02, but in this case, the order of appearance is changed. The corresponding displacement maps are shown in Fig. 4.33. In this measurement, the presence of mode 02 is noticed as well. Mode 31 is not clearly defined in the shaker loading case.

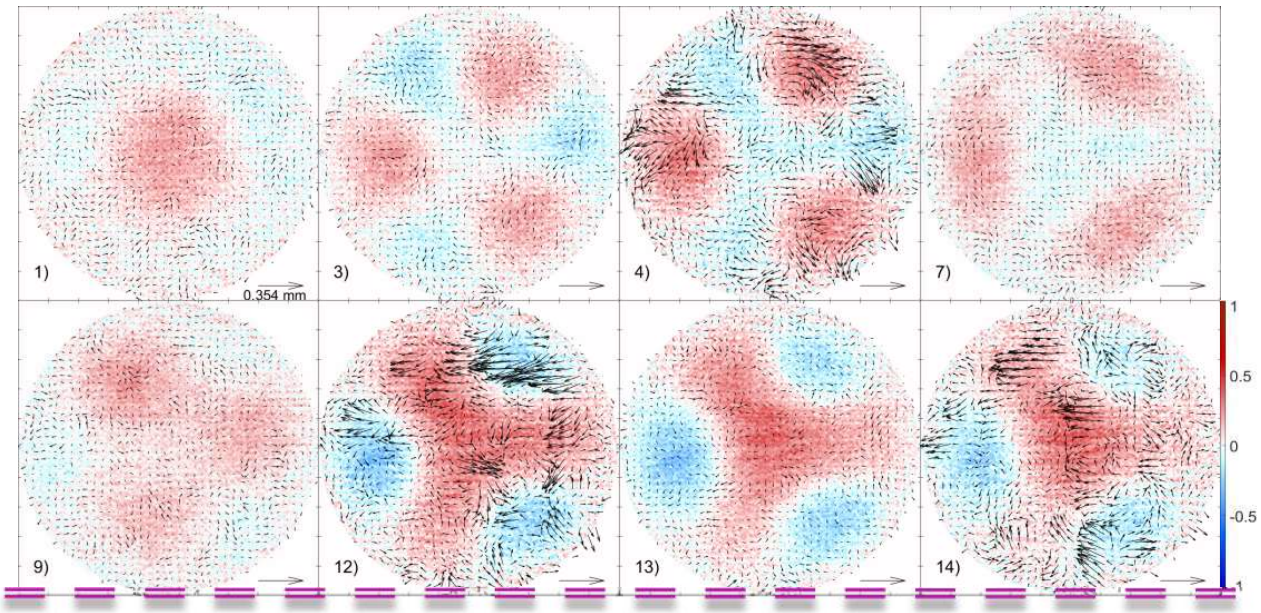

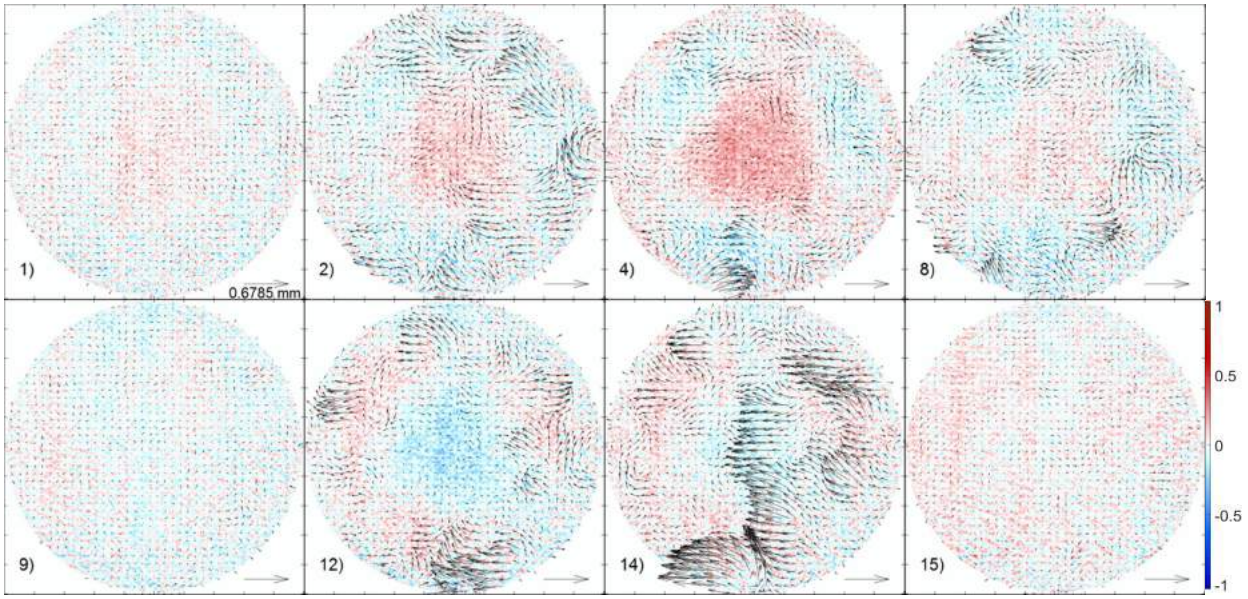


*Fig. 4.33 Mode 31, 340 Hz; time between consecutive snapshots is 0.37 ms.*

#### 4.3.2.1.5 Mode 02, **354 Hz**, 700-µm thickness aluminum plate

Displacements associated with mode 02 are included in Fig. 4.34. This mode presents in-plane displacements that appear spontaneously, panels 5, 13, 15, 4, 6 10, 14. Despite being relatively weak, this mode does present the structure corresponding to 2 rings and the inversion of the inner lobe.

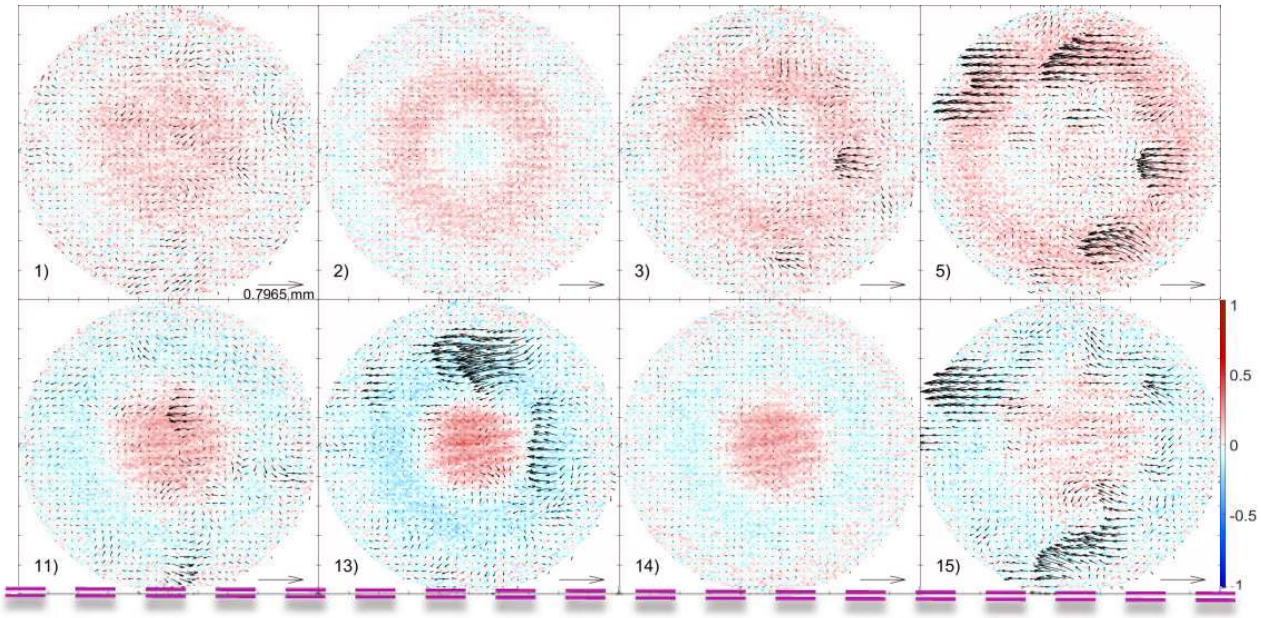

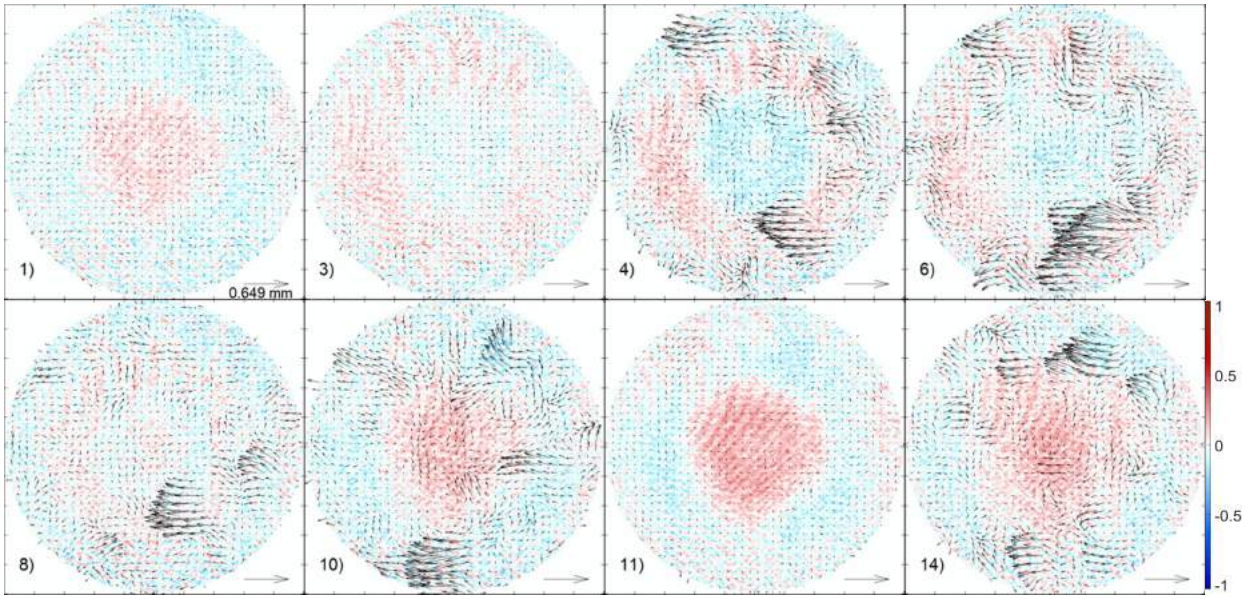


*Fig. 4.34 Results of FP-DIC, images taken at 354 Hz; time between consecutive snapshots is 0.35 ms.*

### *4.3.3.2 Conclusions*

Aluminum plates resulted to be more repeatable than leather, the vibration modes can be found at the same resonance frequency irrespective of the environmental conditions.
The sequence of the appearance of the modes is changed regarding the theoretical expectations; mode 21 appears first than mode 11 and mode 31 appears first than mode 02; however, entirely pure modes are not observed.
In-plane displacements have some spontaneous movements, due to the lack of flexibility of material.
By computing the ratios between resonance frequencies for the cases of leather and aluminum, we find out they behave like thin plates.
In the following sections, aluminum is replaced by latex and rubber.

## 4.4 LATEX MEMBRANE

The previous examples give us results that can be considered as thin plates; to illustrate an object behaving as a membrane, we use a fully elastic material, latex (Fig. 4.35); its properties are shown in Table 4.19.
The force acting in a vibrating membrane is only tension, Section 2.3.1; therefore, the tension has a fundamental role in the generation of vibration modes.
Uniform loading (speaker) is the only type of loading that is applied to both latex and rubber membranes.

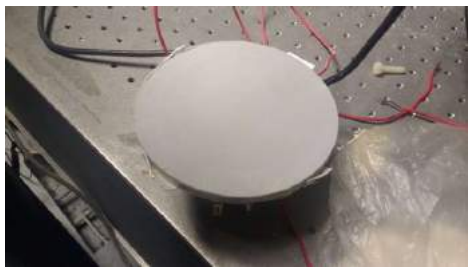

*Fig. 4.35 Latex membrane.*

| Properties | Value | Units |
|---|---|---|
| Radius | 62.5 | mm |
| Thickness | 0.049 | mm |
| Poisson ratio | 0.1 | - |
| Young modulus | 1e+6 | Pa |
| Density | 1736.32 | $kg/m^3$ |

*Table 4.19 Properties of latex membrane.*

### *4.4.1 LATEX MEMBRANE (13-CM DIAMETER)*

Setup parameters are shown in Table 4.20; the speaker is as close as possible to the membrane without touching it.

| $B$ (mm) | $H$ (mm) | $\theta$ (°) | $p$ (mm) |
|---|---|---|---|
| 170 | 368 | 24.8 | 1.202 |

*Table 4.20 Setup parameters.*

The vibration mode frequencies are in Table 4.21; it only presents mode 01, 11, and 02, because the other modes are a mixture of different modes.

| Mode | $f_{theoretical}$ (Hz) | $f_{numerical}$ (Hz) | $f_{real}$ (Hz) |
|---|---|---|---|
| 01 | 70 | - | 70 |
| 11 | 111.5 | - | 90 |
| 21 | 149.5 | - | - |
| 02 | 160.7 | - | 190 |
| 31 | 185.7 | - | - |

*Table 4.21 Vibration mode frequencies.*

#### *4.4.1.1 Results*

The setup of this case has an FP resolution of 60 µm, a DIC resolution of 15 µm, and a conversion factor of 0.147 mm/pix.

The further part of the outer ring in the next figures is part of the mounting; hence in this zone, the magnitude of displacement is almost null.

##### 4.4.1.1.1 Mode 01, **70 Hz**, 13-cm diameter latex membrane

Snapshots for mode 01 are presented in Fig. 4.36. It is noticed that IPCD presents a well-defined radial distribution, characteristic of OOPCD projections. The shape of vibration mode is similar

to that obtained in Section 4.2 (leather drum) and Section 4.3 (aluminum plate). These results are the ones with the least level of noise.

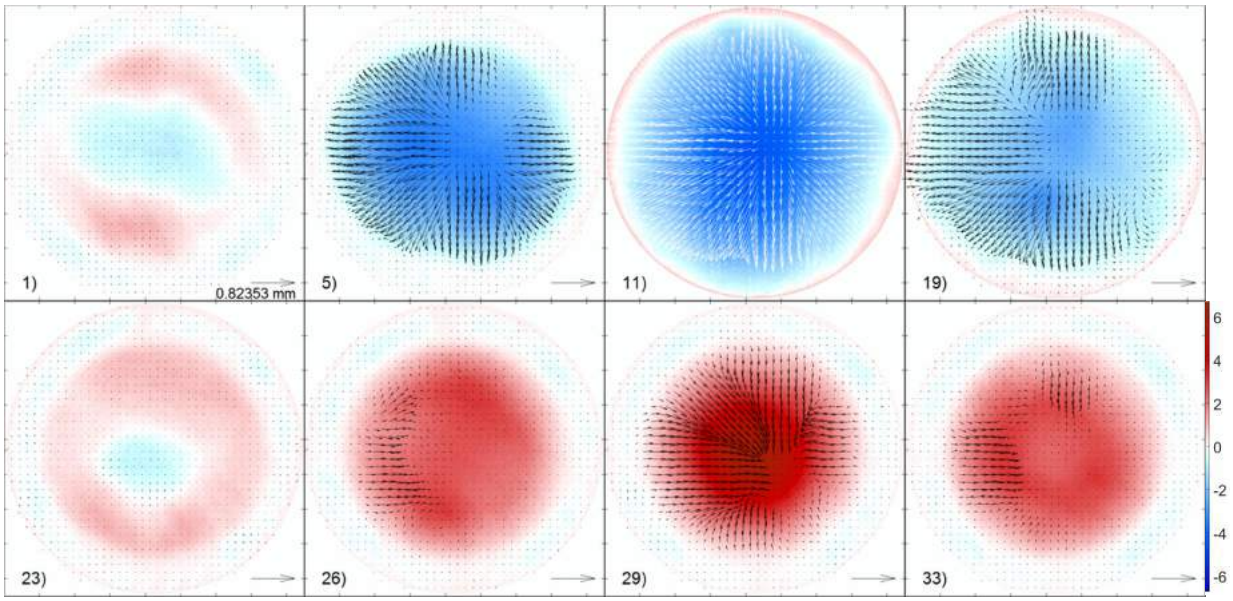


*Fig. 4.36 Mode 01, 70 Hz; time between consecutive snapshots is 1.79 ms.*

#### 4.4.1.1.2 Mode 11, **90 Hz**, 13-cm diameter latex membrane

Figure 4.37 shows the OOPCD and IPCD for this frequency. The measured mode at some snapshots is recognized as the 11 mode (panels 1 and 16), but in the others, the predominance of mode 01 is noted. The greater the OOPCD, the greater the IPCD; hence, the IPCD is the result of the projection (cone of vision effect) of the OOPCD.

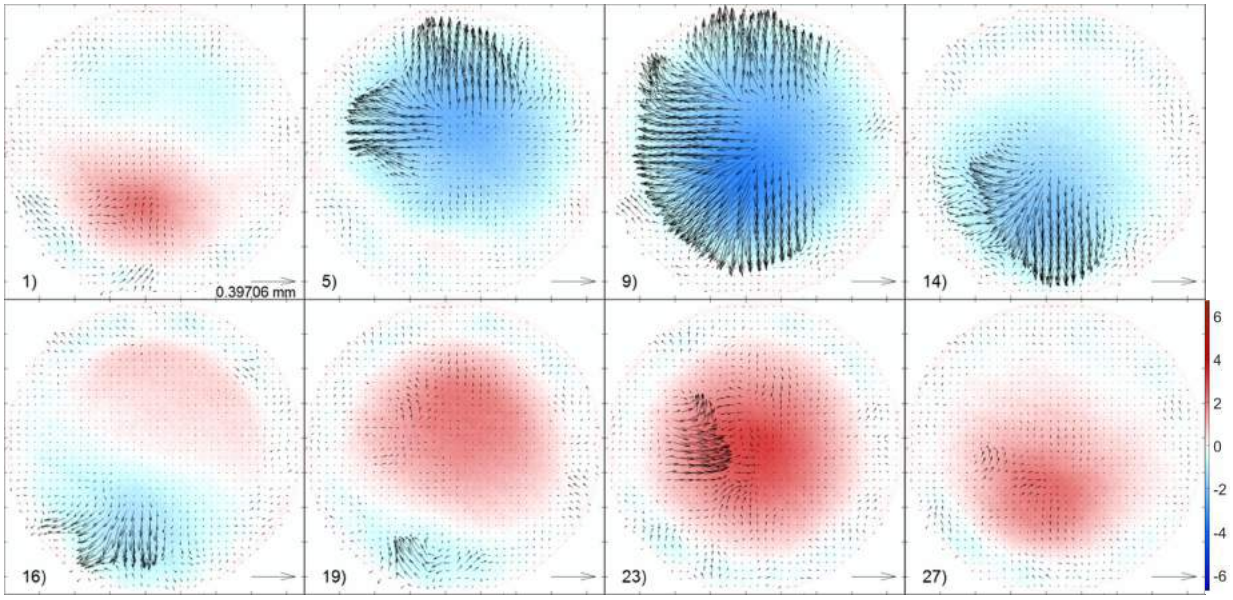


*Fig. 4.37 Mode 01, 90 Hz; time between consecutive snapshots is 1.38 ms.*

#### 4.4.1.1.3 Mode 02, **190 Hz**, 13-cm diameter latex membrane

At other intermediate values of frequency between 90 Hz and 190 Hz, other resonant modes are appreciated, but since no known distribution is perceived, they are not reported. At 190 Hz, we localize mode 02, Fig. 4.38. It is notorious the presence of in-plane displacements over the central ring and the outer ring, implying the existence of the cone-of-vision effect.

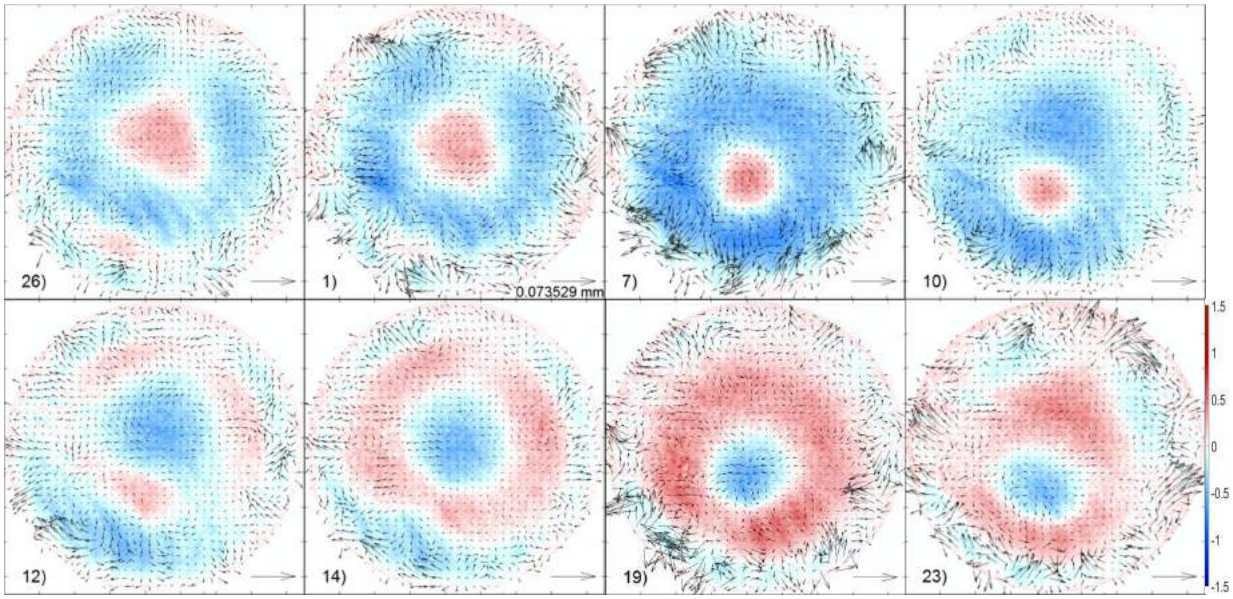


*Fig. 4.38 Mode 02, 190 Hz; time between consecutive snapshots is 0.66 ms.*

### *4.4.1.2 Conclusions*

The membrane of this section is subjected to small tension; this may be the reason for having measured only two modes.

Together with the results of next section, these series of measurements present the least level of noise.

## 4.5 RUBBER MEMBRANE

The rubber properties are shown in Table 4.22, this material is less flexible than latex. Figure 4.39 shows the rubber membrane. This object presents the vibration modes with the highest quality; they are almost similar to the theoretical ones.

*Fig. 4.39 Rubber membrane.*

| Properties | Value | Units |
|---|---|---|
| Radius | 85 | mm |
| Thickness | 0.34 | mm |
| Poisson coefficient | 0.15 | - |
| Young modulus | 100e+6 | Pa |
| Density | 1307.9 | $kg/m^3$ |

*Table 4.22 Properties of rubber membrane.*

### *4.5.1 RUBBER MEMBRANE (17-CM DIAMETER)*

The setup parameters are included in Table 4.23.

| $B$ (mm) | $H$ (mm) | $\theta$ (°) | $p$ (mm) |
|---|---|---|---|
| 150 | 510 | 16.4 | 1.405 |

*Table 4.23 Setup parameters.*

In Table 4.24 we present the different frequencies of the observed and recognized modes.

| Mode | $f_{theoretical}$ (Hz) | $f_{real}$ (Hz) |
|---|---|---|
| 01 | 65.0 | 65 |
| 11 | 103.6 | 95 |
| 21 | 138.8 | 131 |
| 02 | 149.2 | 160 |
| 31 | 172.4 | 178 |
| 12 | 189.6 | |

*Table 4.24 Vibration mode frequencies.*

#### *4.5.1.1 Results*

Resolutions for this system are 70 µm, and 21 µm, for FP and DIC, respectively. The conversion factor is 0.213 mm/pix.

##### 4.5.1.1.1 Mode 01, **65 Hz**, 17-cm diameter rubber membrane

Mode 01 is observed to fit the theoretical shape, except at relatively small OOPCD, as seen in Fig. 4.40. The IPCD follows tightly the OOPCD projection.

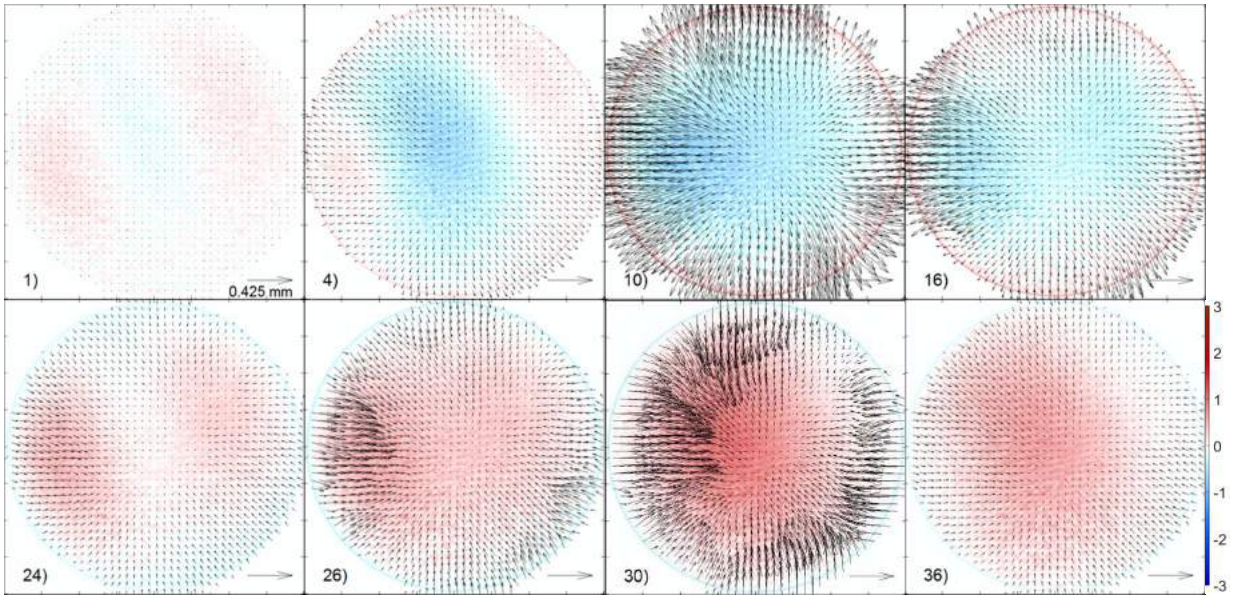


*Fig. 4.40 Mode 01, 65 Hz; time between consecutive snapshots is 1.92 ms.*

#### 4.5.1.1.2 Mode 11, **95 Hz**, 17-cm diameter rubber membrane

In Fig. 4.41 we illustrate the 3D-displacement map of mode 11. Unlike the latex result, in this case, higher modes are reasonably recognized. Recalling that for the projected OOPCD in red zones, the IPCD is directed away from the center, and inwards for blue zones, the IPCD refers basically to OOPCD projection (their magnitudes are proportional as well). The direction of the line that joins the center of the lobes depends on the exact boundary conditions, the uniformity of the loading and the uniformity of the mechanical properties.

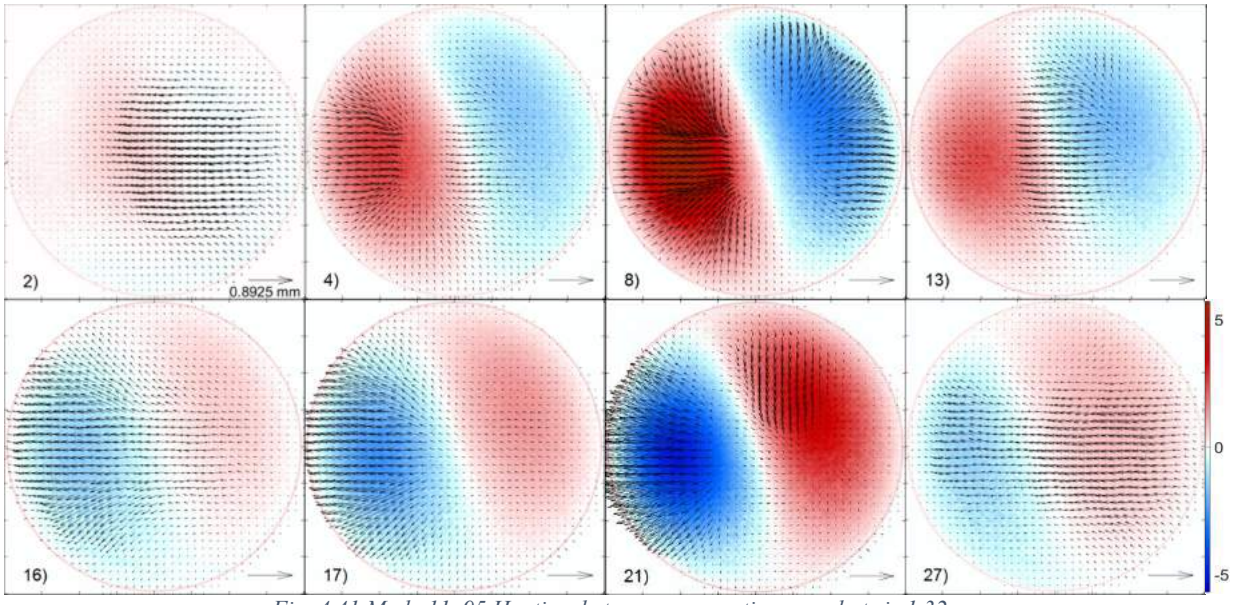


*Fig. 4.41 Mode 11, 95 Hz; time between consecutive snapshots is 1.32 ms.*

#### 4.5.1.1.3 Mode 21, **131 Hz**, 17-cm diameter rubber membrane

The shape of the displacement maps is similar to mode 21, except that the two lobes joined by a line at 135$^{o}$ are not separated (Fig. 4.42).

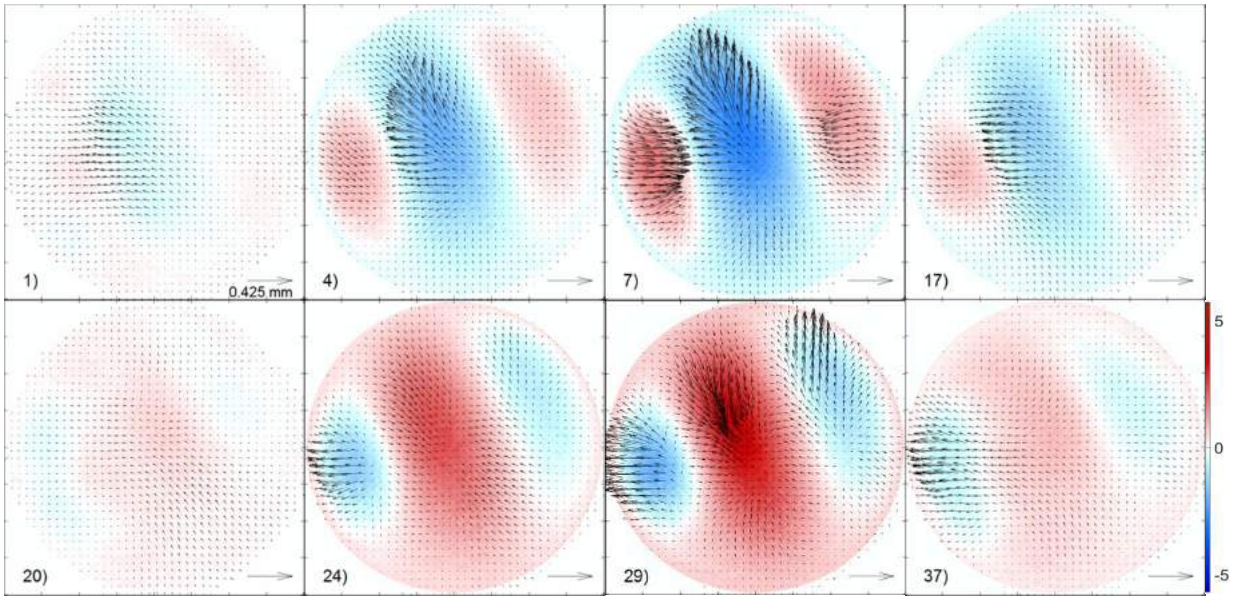


*Fig. 4.42 Mode 21, 131 Hz; time between consecutive snapshots is 0.95 ms.*

#### 4.5.1.1.4 Mode 02 **160 Hz**, 17-cm diameter rubber membrane

The resulting displacement maps suggest this is the case of mode 02 (Fig. 4.43); yet, the inner ring spreads out into the outer ring, on the left part of the figure.

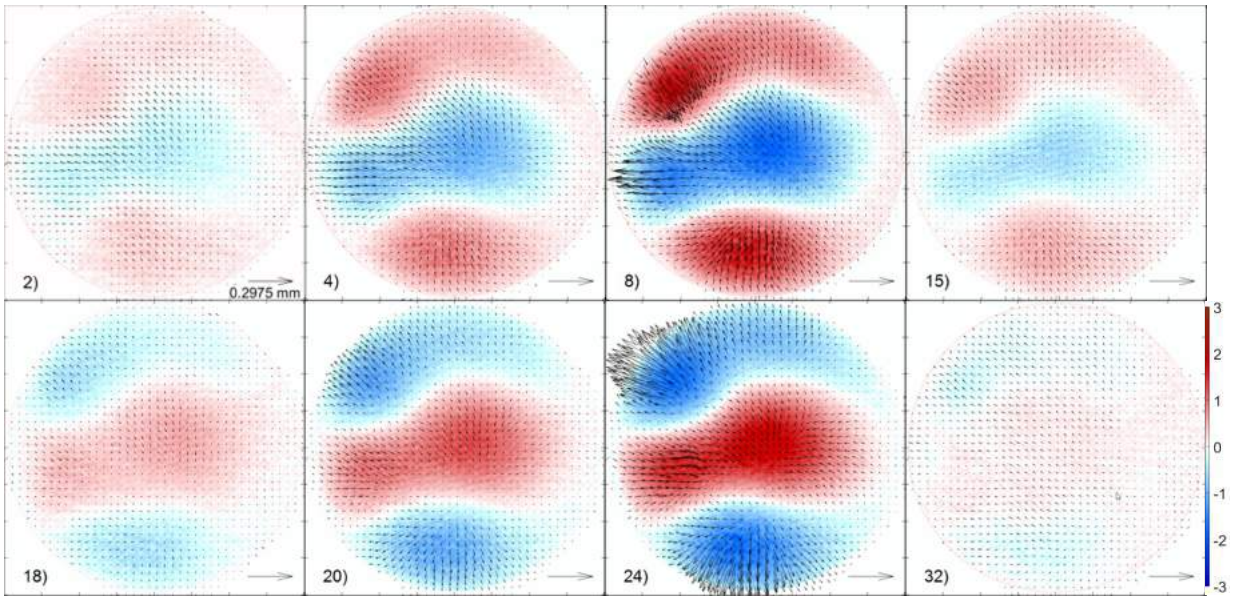


*Fig. 4.43 Mode 02 at 160 Hz; time between consecutive snapshots is 0.78 ms.*

#### 4.5.1.1.5 Mode 31, **178 Hz**, 17-cm diameter rubber membrane

Unexpectedly, one of the highest modes, mode 31, could be measured neatly, sown in Fig. 4.44. As it is observed, the magnitude of the snapshots is not symmetrical in time, yet the reversing of the lobes is readily noticed.

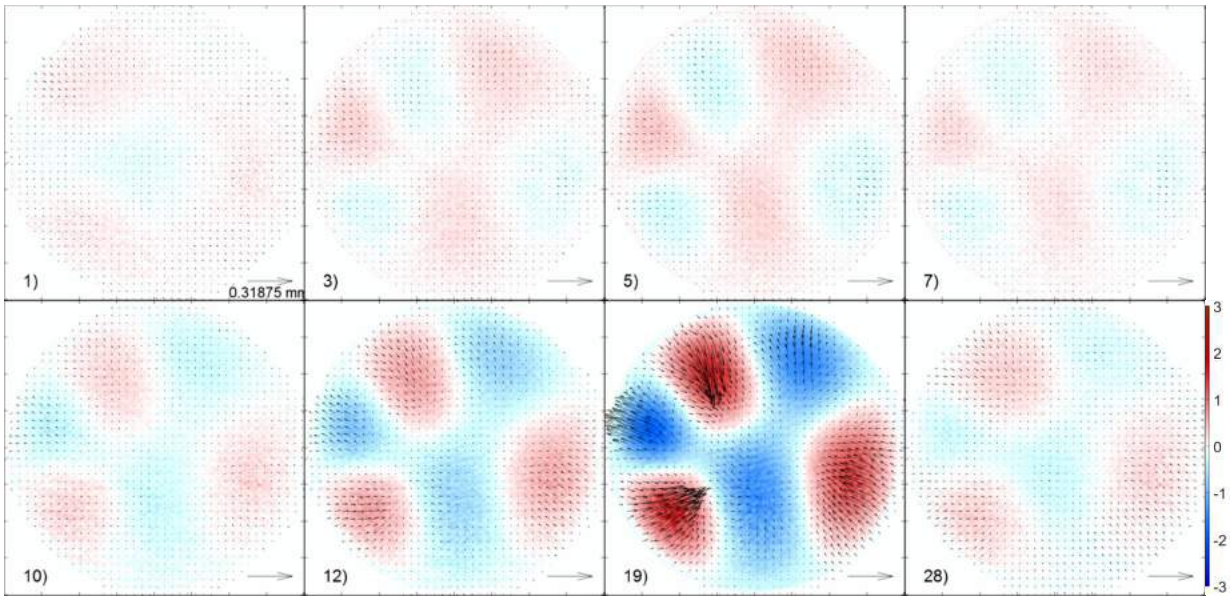


*Fig. 4.44 Mode 31, 178 Hz; time between consecutive snapshots is 0.70 ms.*

### *4.5.1.2 Conclusions*

The rubber object presents a membrane behavior; its vibration mode frequencies fit fairly well the proportion between theoretical modes. Besides, the main contribution to IPCD comes from the OOPCD projection (cone-of-vision effect). Additionally, for this object, even mode 31 was managed to be measured.

## 4.6 CONCLUSIONS

In this chapter we showed the feasibility of FP-DIC, where resolutions of the order of 50 µm and 20 µm, for FP and DIC, respectively, were achieved. For comparison reasons, first some vibration modes were measured by using FP and DIC, but in a separated way.

We tested two types of objects: ones that behave as a thin plate (leather and aluminum) and others like a membrane (latex and rubber). For the thin plates, different thickness and size were used; also, different type of loading (point-like and uniform) was carried out. For the membranes, only uniform loading was applied, but two distinct sizes were tested. We verified that the mode frequency decreases as the thickness/size/Young modulus increases. The type of loading changed slightly both the values of the resonance frequencies and their shapes.

The IPCD (in-plane component of displacement) present in most of the measurements was due to the cone-of-vision effect arising from the OOPCD (out-of-plane component of displacement) projection. In some examples, the effect of the point-like loading overrode the previous effect.

In several cases, some unexpected results were obtained: modification of the order of appearance of some modes, coupling between modes, strong spontaneous IPCD, and asymmetry of modes. These anomalies seem to have several causes, such as non-uniformity of the fixing of the objects,

the non-uniformity of the loading, the pre-loading conditions (in the case of the plates), and the inhomogeneity of the mechanical properties.
Aluminum showed a higher level of repeatability than leather, and this was reflected as mode shapes that fitted closer to the theoretical ones. This finding was enhanced in the case of the elastic membranes.
In general, up to 5 vibration modes were managed to be measured. Visually, we could verify the existence of higher modes, but their displacements were beyond the resolution of the system.

## 4.7 REFERENCES

1. L. F. Sesé, P. Siegmann, F. A. Diaz, and E. A. Patterson, “Simultaneous in-and-out-of-plane displacement measurement using fringe projection and digital image correlation,” Opt. Lasers Eng. **52**, 66–74 (2014).

# 5. CONCLUSIONS AND FUTURE WORK

In this work, to measure in-plane and out-of-plane displacements of a vibrating circular object, in a simultaneous way, a combination of fringe projection and digital image correlation (FP-DCI) was used. FP-DIC let us measure the out-of-plane component of displacement, OOPCD, with an accuracy of around 60 μm and IPCD with an accuracy of about 20 μm.

Several parameters were analyzed to obtain acceptable results. The analyzed parameters of FP were period, quantity of noise in images, and angle between camera and projector; the analyzed parameters of DIC were fill percentage (number of particles), particle diameter and magnitude of displacements.

The numerical simulations of FP gave the next considerations.

- An appropriate period was at least 5 pix. Even though a small period had more resolution than a large period, its minimum value (2 mm) is limited by the resolution of the used projector.
- In regard with the range of values of displacement, the minimum value is related with the general rule of thumb of taking one-twentieth of the period, which in this case is about 60 μm. On the other hand, the maximum value is about 5 cm which corresponds to the depth of field of the camera.
- A recommended projection angle is in the range of 10° to 20°; larger values may cause shadows on the scene.

The numerical simulations of DIC indicate the following.

- To warrant values of error less than 5%, the fill percentage should be around 3%. Values far from this setting imply having a reduce number of spatial structures, which produces degradation of the corresponding correlations.
- A particle diameter of around 2 pix is recommended.
- The resolution is related mainly to the accuracy of the correlation package, which for proVISION is 0.1 pix; this value, for an image size of 1280x760 pix and a scene region of 20 cm, is equivalent to around 20 μm.
- Displacements should be less than a quarter of the size of the correlation window (8 pix); this value therefore amounts approximately to 10 mm.

The latter limiting values corresponding to separated FP and DIC are valid as well to FP-DIC, since coupling between both techniques was reduced to a minimum by selecting the most spectrally separated color channels of the recording camera, blue and red channels.

Considering the vibrating objects, we can remark the following points.

- For a plate, the resonance frequency of out-of-plane vibration modes varied inversely with thickness and diameter of the plate.
- For a membrane, its tension has a large effect on the resonance frequency of out-of-plane vibration modes.
- The resonance frequency must be less than a tenth of the camera frame rate, 5000 Hz. This prevents any blur appearing in the registering images, during the exposure time of the camera.
- We verified that experimental shapes of vibration modes were similar to those dictated by theory and that their resonance frequencies were around the calculated frequencies.

- The vibration modes were located in a bandwidth instead of a defined value of frequency; this bandwidth decreases with the order of the vibration mode.
- In various cases, high-order vibration modes were stronger than low-order ones, giving rise to non-pure modes. This may have been caused by the non-uniformity of the fixing of the drums to the mountings and by the lack of uniformity of the applied load.

As future work, it may carry out the extension of this work to the theoretical study and mathematical analysis of in-plane vibration modes, as well as its numerical modeling. The implementation of an excitation layout to promote in-plane vibration modes would be equally desirable. Also, it would be useful to apply the FP-DIC method for measuring deformations in industrial parts (with complex geometries) without the need to use paints or developers.